# Preface

The subject of this thesis is an investigation of sizes and shapes (textures) and orientations (fabrics) of ice crystals during a warm event in the last glacial from the GReenland Ice core Project (GRIP) ice core. A new method for measuring the textures of individual crystals by mean of a semi-automatic image analysis technique is implemented. Fabrics of the ice crystals were supposed to be measured by a new automatic instrument from Australia, but a continuous delay in the delivery of the instrument made it necessary to look for another solution. Such a solution was fortunately found at Alfred Wegener Institute (AWI) in Bremerhaven, Germany, where a Japanese instrument, an Automatic Ice Fabric Analyzer, had just been installed. The fabric measurements were made during two visits in Bremerhaven. I would like to thank AWI for letting me use the instrument, and especially Yun Wang for help with the measurements. Allthough the first visit gave no usefull results, it was not fruitless. I had an introduction to the image analysing software package Image-Pro, and was taught the leason that patience and thoroughness is essential in experimental work, and that easy solutions are few. The visits at Bremerhaven were made possible with financial support from the Geophysical Department, NBIfAFG and the FREJA-project: "Ice in the planetary system".

Dorthe Dahl-Jensen was supervisor on this project, and I would like to thank her for encouragement during the project and for suggesting this subject to me, which I have found very interesting and challenging. Anders Svensson substituted for Dorthe during her maternity leave and continued as the main supervisor on this work. I would like to thank him heartily for the continuously encouragement and thorough comments on the project in all phases.

Thanks to Claus U. Hammer for letting me use unpublished data on continuous impurity measurements, and to Jørgen Peder Steffensen for letting me use unpublished data on ionchromatograph measurements. Jørgen Peder Steffensen also helped with the log-normal distributions, for which I am very grateful.

I would also like to thank my family, especially my girlfriend Pernille for the continuous support and encouragement, and for standing in for me in the family the last couple of months. Last but not least, thanks to my daughter Veronika, who more than fullfilled my sparetime, so I was not occupied by this project at all hours, and for giving me not too many sleepless nights.

The work with this thesis started in January, 2000. January–April, I worked half-time while finishing my last master courses. During May–August, I was occupied by a student position at the Danish Meteorological Institute, leaving only few weeks for work on this thesis. September–October I had maternity leave. From November 2000, I have worked full time.

Kaj Mantzius Hansen
Copenhagen, 24/6-2001

# Dansk resume

Dette speciale har to formål. Det første er at implementere nye halvautoma-
tiske metoder til at undersøge iskrystallers størrelse, form og orientering (på
engelsk kaldet *texture* og *fabric*). Det andet formål med specialet er at un-
dersøge hvordan disse parametre ændrer sig i løbet af en varmeperiode (en
*interstadial* eller Dansgaard-Oeschger begivenhed) under den seneste istid.
Den valgte begivenhed fandt sted for ca. 25.000 år siden og havde en varighed
på ca. 300 år. Til undersøgelsen udvalgtes 6 prøveserier af 55 cm længde, to
før, to under og to efter begivenheden. Prøverne er taget fra interstadial 3 i
2015–2030 m dybde fra GReenland Ice core Project (GRIP) iskernen boret i
det centrale Grønland.

Til at undersøge iskrystaller udnytter man at de er dobbletbrydende og
optisk enaksede. Placeret mellem to krydsede lineære polarisatorer vil hvert
krystal fremstå med en farve, der ofte er forskellig fra nabokrystallet på grund
af en anden orientering. Farveforskellen udnyttes til at skelne de enkelte kry-
staller fra hinanden. Drejes prøven mellem polarisatorerne vil krystallernes
farve ændres, hvilket man udnytter til at finde deres orientering.

I specialet beskrives en halvautomatisk metode til at finde iskrystallers
grænser ved hjælp af sammenlagte højopløste digitalbilleder. Metoden udnyt-
ter intensitetsforskellen mellem krystallerne når billederne bliver taget med
prøven placeret mellem roterende krydsede polarisatorer. Når grænserne
er bestemt, kan et billedbehandlingsprogram udregne areal, forhold mellem
længden og bredde, omkreds og andre parametre der beskriver krystallernes
størrelse og form. Denne metode implementeres og justeres så den giver det
optimale resultat for de valgte prøver.

Iskrystallernes orientering måles med et automatisk instrument opstil-
let i Bremerhaven, Tyskland. Det beskrives hvordan instrumentet benytter
billedbehandlingsteknikker til at udføre målingerne.

Både målingerne af form og størrelse og målingerne af orienteringen gik
generelt godt. Størrelse og form af 60.000 krystaller blev målt, selv om en
betydelig del af grænserne, 10–15%, måtte justeres. Ved hjælp af den hal-
vautomatiske metode kan man finde størrelsen og formen af mange krystaller

iv

på kort tid, men der skal endnu arbejdes en del med metoden før den bliver
en standard procedure indenfor iskrystalundersøgelser. Resultaterne af un-
dersøgelsen viser at krystalstørrelsen generelt varierer med klimaet. Midde-
larealet af krystallerne er hhv. 3.36 mm$^2$ og 3.04 mm$^2$ under og før/efter
Dansgaard-Oeschger begivenheden. Det postuleres at denne sammenhæng
skyldes en korrelation mellem krystalstørrelsen og indholdet af opløselige
urenheder, særligt nitrat. Dette understøttes af en undersøgelse af vinklen
mellem nabokrystaller der indikerer at urenheders hindring af krystalgrænse-
migration er den dominerende process der afgører krystallernes størrelse. Det
støttes yderligere af at arealfordelingen af iskrystallerne, som tilnærmelsesvis
har form som en log-normalt fordeling, ikke ændrer form hen over klimabe-
givenheden.

Orienteringen af mere end 10.000 krystaller blev målt. Prøverne viser et
stærkt enkelt maksimum, hvilket stemmer godt overens med tidligere resul-
tater fra GRIP iskernen. Det vises at der er en svag tendens til forstærkning
af maksimummet med dybden, og at der ikke tilsyneladende er en forskel på
styrken indenfor og udenfor Dansgaard-Oeschger begivenheden.

Størrelse og orientering af krystallerne i mælkehvide bånd (*cloudy bands*)
undersøges også. Generelt findes en sammenhæng mellem båndenes inten-
sitet og størrelsen af krystallerne i dem, men denne sammenhæng er ikke
entydig. Der findes signifikant mindre krystaller med et svagere samlet mak-
simum i båndene end udenfor båndene. Det foreslås at dette skyldes en øget
glidning mellem krystallerne i krystalgrænserne.

# Contents

# Chapter 1

# Introduction

In this chapter follows a short introduction, where I will describe how ice sheets are formed, and how palaeoclimatic informations can be extracted from the ice sheets by ice core drilling. This thesis is an investigation of the sizes and shapes (*textures*) and orientations (*fabrics*) of ice crystals in a rapid climate change in the last glacial from the GReenland Ice core Project (GRIP) ice core. I will shortly describe the GRIP ice core, the general results obtained from it, and the characteristics of the rapid climate changes. At the end of the chapter, I will give a synopsis of the thesis.

## 1.1   Ice sheets

Ice sheets are formed from snow, which in the process of transformation is called *firn*. The new fallen snow, consisting of ice grains with complex shapes, has a density of about 50–70 kg m$^{-3}$ [Paterson, 1994]. Each grain consist of one or more ice crystals. The density of the firn increases as new snow falls upon it and it sinks further and further down into the ice sheet. The firn is transformed into ice at a density of 830 kg m$^{-3}$, when the air space between the individual grains close off. The density of the ice increases further, as the air bubbles are compressed by deformation of the surrounding ice. The maximum density of the ice is about 917 kg m$^{-3}$ [Paterson, 1994].

Deformation takes place because ice is a quasiviscous material that slowly deforms and float. As the ice sinks due to the pressure from the above lying ice and firn, the layers are thinned. If the yearly layer thinning (due to ablation or calving of ice bergs at the ice margin) equals the growth due to precipitation, the ice sheet is said to be in an equilibrium state. This is assumed about the Greenland ice sheet. The flow of the ice in an ice sheet is generally downwards and out toward the ice sheet margins. At the ice divide

— the central point of the ice sheet that divides the flow — the flow is mainly downward. This ensures a unique chronology as the layers are only thinned and not deformed in other ways. In Greenland the ice at the bottom of the ice divide is believed to be from the formation of the ice sheet, which could be more than a million years ago. The ice in the lower part is deformed by a strong shear stress depending on the bottom topography.

## 1.2   Ice cores and palaeoclimatic information

The snow, firn and ice in ice sheets contains information about the climate at the time of precipitation by means of the $\delta^{18}O$ value. $\delta^{18}O$ is a measure of the content of the heavy $^{18}O$ isotope compared to the lighter $^{16}O$ isotope in the ice, in proportion to the same ratio in a sample of Standard Mean Ocean Water. Since the water vapor pressure is slightly lower for $^{18}O$ than for $^{16}O$, the precipitation will be depleted for the more heavy isotope, as the residence time in the clouds increases. The water vapour pressure is temperature dependent, so $\delta^{18}O$ correlates very well with the temperature at the place and time of deposition. In this way, variations of the $\delta^{18}O$ value will reflect climate variations at the time of deposition of the snow.

Information about the composition of the atmosphere at the time of precipitation can be derived from measurements of the air bubbles included in the ice, and from the concentration of soluble and insoluble impurities in the ice. Insoluble impurities are dust particles and volcanic ashes, soluble impurities are chemical ions or elements such as $Ca^{2+}$, $Na^{+}$, $Cl^{-}$, $SO_4^{2-}$.

The palaeoclimatic informations can be obtained by drilling ice cores out of the ice sheets. When ice cores are drilled at an ice divide the ice is stratified and annual layers in most of the ice are undisturbed. Ice core drillings have been made at several sites both in Greenland, in Antarctica and on many small glaciers around the world. In figure 1.1 the sites referred to in this thesis is marked.

## 1.3   The Greenland Ice Core Project

The GRIP ice core drilling was initiated in 1989, at 72°34.5'N, 37°38.5'W, 3230 m.a.s.l. very close to the highest point, Summit, and the present ice divide. The bedrock was reached in 1992, where the bottom part of the 3028.65 m ice core was retrieved [Dansgaard et al., 1993, GRIP Members, 1993]. The present day accumulation rate at the drilling site is 0.23 m ice equivalent per year, and the mean surface temperature is -32°C.
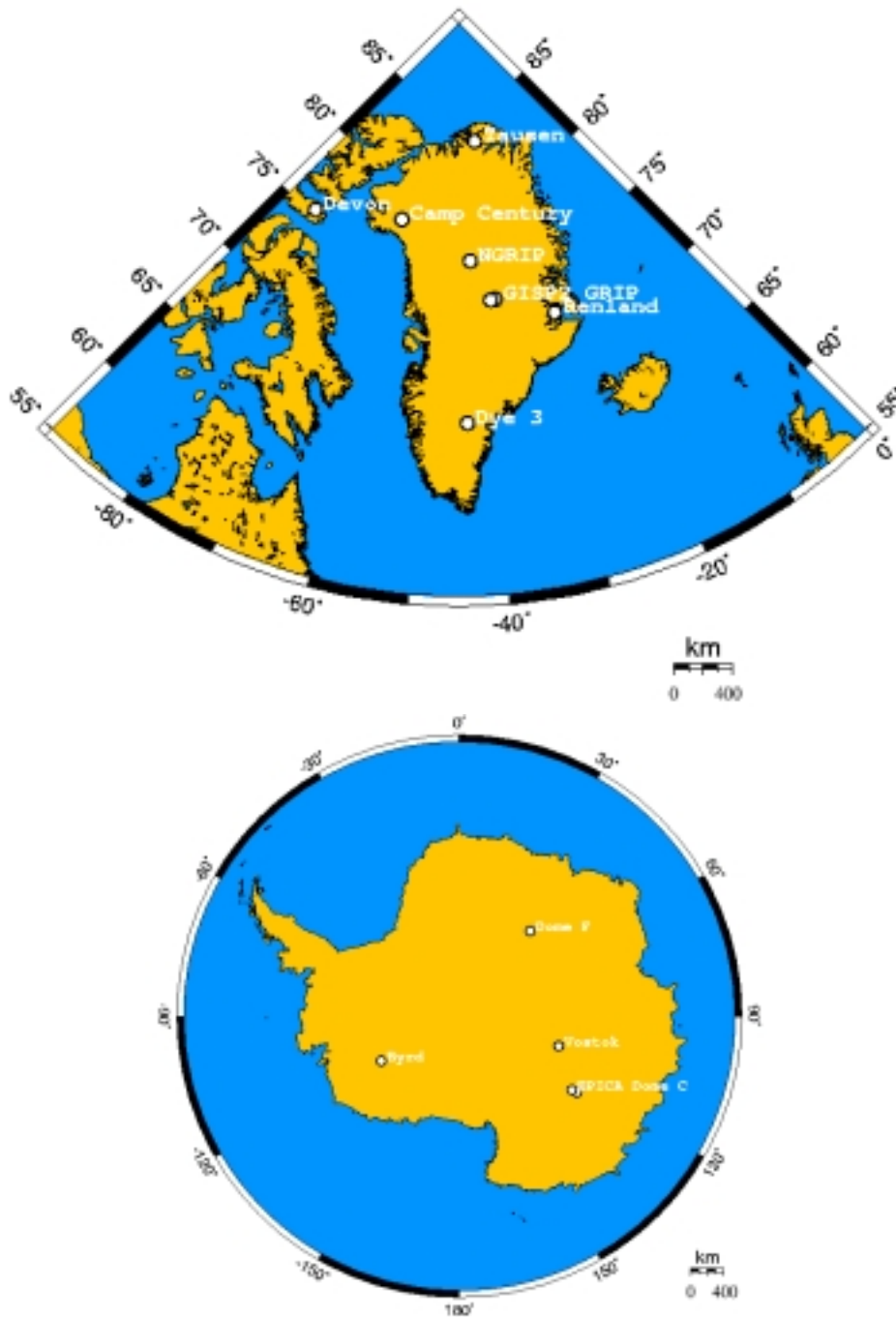
Figure 1.1: Deep ice core drillings referred to in this thesis. In Greenland: Camp Century (1966), Dye 3 (1981), Renland (1988), GRIP (1992), Greenland Ice Sheet Program 2 (GISP2) (1993), Hans Tausen (1995) and NorthGRIP (not terminated). In Antarctica: Byrd (1968), Dome C (1978), Dome F (1997), Vostok (1998), European Project for Ice Coring in Antarctica (EPICA): Dome C (Not terminated) — South of the old Dome C drilling.

## 1.3.1   Results from the GRIP ice core

The main result from the GRIP ice core is the $\delta^{18}O$ curve, which can be
seen in figure 1.2. The $\delta^{18}O$ curve shows that the present interglacial, the
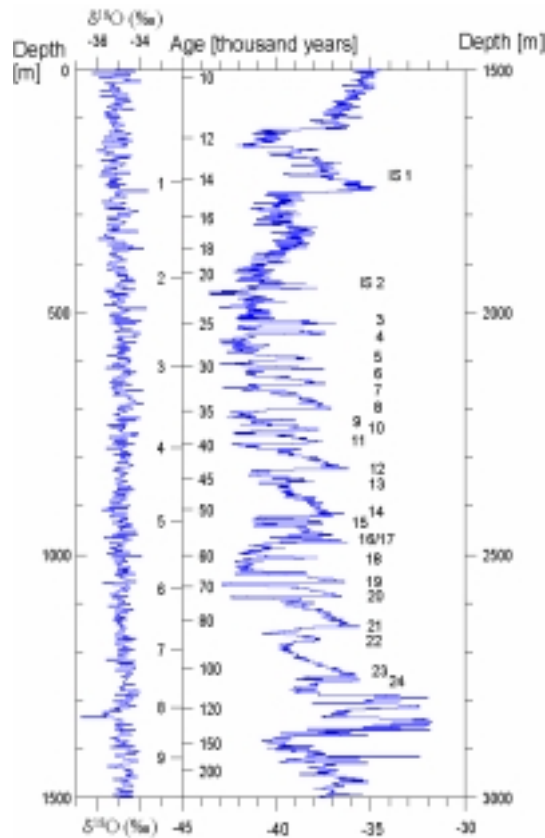


Figure 1.2:  The $\delta^{18}O$ curve from the GRIP ice core.  To the left is shown the upper
1500 m and to the right the lower 1500 m of the core.  A time scale for the ice is given
in the middle.  In the Wisconsin part of the record, the 24 interstadials (IS) are marked.
Adapted from [Dansgaard et al., 1993].

*Holocene* (0–1625 m) has been remarkably stable, but that the last glacial,
the *Wisconsin* (1625–2790 m) was characterized by dramatic climate changes.
The climate changes has a characteristic saw-tooth shape, with a rapid war-
ming during few decades, and a gradual or step wise cooling over a couple of
hundred years or more.  The relative mild climate events have been named
*interstadials* (IS) — as opposed to the glacial *stadials* — and have also be-
come known as Dansgaard-Oeschger events.  The ice at 2790–2865 m depth is
believed to originate from the last interglacial, the *Eem*. This interglacial was
generally warmer than the present interglacial, but apparently much more

unstable. It has been debated whether the layers at this depth has been disturbed [Alley et al., 1995a].

The interstadials were first observed in the Camp Century ice core drilled in 1966 in northwest Greenland [Dansggard et al., 1971]. They were doubted to be real climate events, until they were found in the Dye 3 and the Renland ice cores [Dansgaard et al., 1984, Johnsen et al., 1992b]. With the finding of the Dansgaard-Oeschger events in the GRIP ice core their existence is undoubted [Johnsen et al., 1992a]. The Dansgaard-Oeschger events are believed to be associated with changes in the North Atlantic Ocean circulation. It is likely that there generally was almost no circulation in the ocean during the Wisconsin, and that during the interstadials, the circulation was more like the present day, although weaker. This has been supported by investigations of ocean sediment cores, e.g. [Bond et al., 1993, Rasmussen et al., 1996].

Apart from $\delta^{18}O$ measurements, the amount of soluble and insoluble impurities have been extensively studied throughout the core. There is a general anticorrelation between $\delta^{18}O$ and the amount of impurities in the ice. This is due to a more vigorous atmospheric circulation in periods of cold climate [De Angelis et al., 1997].

The crystal properties: *fabric*: orientation and *texture*: size and shape of crystals have also been studied throughout the core. An overview of the results of texture and fabric measurements is given at the end of chapter 2.

The GRIP ice core has been dated by counting the yearly variations in $\delta^{18}O$ and other components such as dust and soluble impurities in the upper 1700 m. Below this depth, the ice is dated with a flow model, using two fix points, which gives a good dating back to 110 kyr BP[1] [Dansgaard et al., 1993].

## 1.4 This thesis

The purpose of this study is to implement new automatic and semi-automatic methods to measure textures and fabrics of ice crystals, and use these methods to measure textures and fabrics of ice crystals across the Dansgaard-Oeschger event IS3.

Figure 1.3 shows the $\delta^{18}O$ curve in the depth interval around IS3, where I have taken my samples. The curve is presented in agreement with common practice, on a depth scale, with increasing depth to the right. Time is in the opposite direction, so the oldest ice is to the right, and the youngest to the left. When ever presenting data and pictures of the ice on a depth/time scale in this thesis, they are presented with this orientation.

---

[1]kyr BP = 1000 years before present
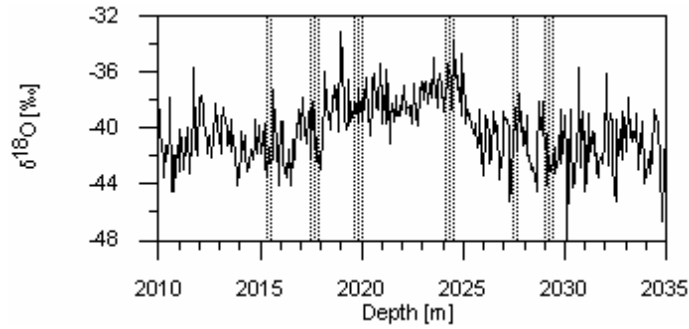
Figure 1.3: The $\delta^{18}O$ curve around IS3 from the GRIP ice core. The vertical hatched lines mark the depth intervals where my samples are chosen.

IS 3 is close to the Last Glacial Maximum, which had the lowest temperature (and the highest amount of impurities) throughout the Wisconsin. The age of the ice at this depth is about 25000 years. The event lasted about 300 years and the amplitude of the change in $\delta^{18}O$ is about $6^0\!/_{00}$ which corresponds to a temperature change of about 13K [Johnsen et al., 1995]. The precipitation rate also changed during the event, it was between about 0.17 (interstadial) and about 0.10 (stadials) m ice equivalent per year [Johnsen et al., 1995]. The yearly layers have thinned to about one fifth of their thickness at the time of precipitation [Dahl-Jensen et al., 1993] or between 1.5–3.5 cm.

**Synopsis**

In chapter 2 I will give a short introduction to the ice crystal structure and the mechanical properties of ice crystals.

The optical properties of ice crystals are presented in chapter 3. These are used when ice crystals are studied, and the most common techniques for measuring textures and fabrics of ice crystals are outlined.

Chapter 4 is a description of how samples are chosen and prepared, and of the techniques I have used to measure the textures and fabrics of the samples.

In chapter 5 I present the results of the measurements of textures and fabrics, and a comparison with previously texture and fabric measurements is made.

In chapter 6 the results will be discussed, and a comparison with other measurements from the GRIP ice core is made. An investigation of textures and fabrics of cloudy bands is also made.

Finally, in chapter 7, I summarize the discussions and conclusions from the previous chapters, and at the end, I recommend subjects for further studies of ice crystal textures and fabrics.

# Chapter 2

# Ice crystals

In this section I will describe the ice crystal and its mechanical properties. I will start with a description of the crystal lattice and of how defects can be introduced in the lattice by deformation. Then I will describe how the individual crystals deform, and how the polycrystal behaves under deformation. Recrystallization is an important type of process in the development of crystals in ice sheets, and a short description of the different types of recrystallization and their influences on textures and fabrics is given. At the end, I will describe how the textures and fabrics develops along the GRIP ice core.

## 2.1   The crystal lattice

Ice is a polycrystalline material. The behaviour of the polycrystal depends on the composition of crystals, on the sizes, shapes and orientations of the individual crystals, and on the stress and temperature in the ice.

Ice is formed by freezing water. The $H_2O$ molecule has the form of a tetrahedron with the oxygen nucleus in the center, and the two hydrogen nuclei in two of the corners. Each hydrogen nuclei is attached by an electron orbit with the electron from the hydrogen atom and one electron from the outer shell of the oxygen atom. In the other two corners of the tetrahedron are electron orbits containing the last four electrons from the outer shell of the oxygen atom. This gives two corners of the tetrahedron with negative charges and two with positive charges.

When the crystal lattice is formed, the negative corners of the water molecules attracts positive corners from other molecules, joining them by a hydrogen bond. So each molecule in the crystal lattice of natural ice ($I_h$) have four nearest neighbours.

The molecules are arranged in layers of hexagonal rings, called basal planes of the crystal. The axis perpendicular to the basal plane is called the c-axis. A sketch of the crystal lattice can be seen in figure 2.1.
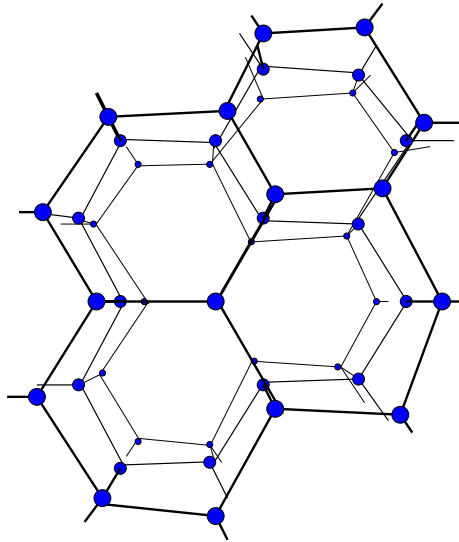


Figure 2.1: The crystal lattice. The molecules are arranged in layers of hexagonal rings. Three such layers, called basal planes are seen in the direction of the c-axis.

## 2.2    Crystal lattice defects

Figure 2.1 shows a perfect crystal lattice, but in natural ice crystals defects in the crystal lattice occur. These defects are either point defects or linear defects and will briefly be described below. A thorough description of crystal lattice defects can be found in e.g. [Hirth and Lothe, 1982, Kossevitch, 1999] for crystals in general, and in e.g. [Hobbs, 1974, Petrenko and Whitworth, 1999] for ice crystals.

### 2.2.1    Point defects

Defects in single molecules in the lattice are called point defects. There is a distinction between defects in the proton configuration and in the molecule configuration. There are two types of defects in the proton configuration. A defect is called a *proton* or *Bjerrum* defect if one binding between two molecules possesses two hydrogen nuclei, and another binding contains no

hydrogen nuclei. The point defect is called an *ionization defect* if a proton has jumped from one oxygen nucleus to the other along a binding, creating a pair of $H_3O^+$ and $OH^-$ molecules. Movement of ionization defects through the crystal accounts for the electric conductivity of the ice. These types of point defects are created when the crystal lattice gets distorted by deformation.

There are also two types of molecule point defects. If a molecule is missing in the crystal lattice, there is a *vacancy*. An extra molecule can be situated in the free space between the ordinary crystal lattice molecules, and we have an *interstitial* molecule. In both cases the crystal lattice is distorted around the vacancy or the interstitial. Interstitials in the ice crystal lattice gives rise to self-diffusion, which is an important process for the grain growth of polycrystalline ice.

Impurities can also enter the crystal lattice, either as interstitial molecules or as *substitutional* molecules, substituting an $H_2O$ molecule in the crystal lattice. The presence of impurities will create proton and ionization defects in the crystal lattice, and have thereby a large influence of the electric conductivity of the ice.

### 2.2.2  Dislocations

*Dislocations* are linear defects in the crystal lattice where a part of the crystal lattice is displaced compared to the rest of the lattice. The most important linear defects are *edge* dislocations and *screw* dislocations. An edge dislocation is an additional half-plane of molecules inserted in the regular part of the crystal, as depicted in the left hand side of figure 2.2. In a screw
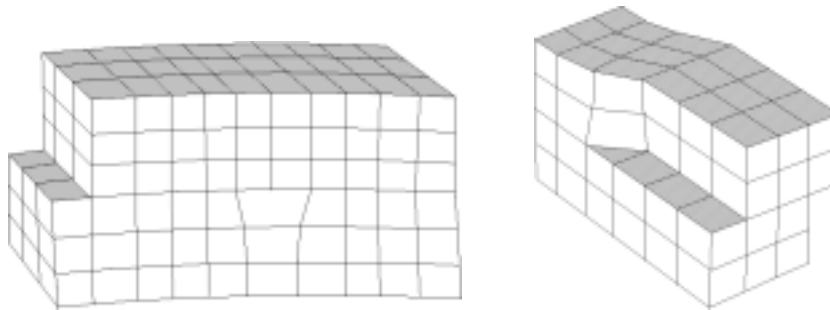


Figure 2.2: Left: An edge dislocation is an extra half-plane of molecules inserted in the regular part of the crystal. The shown dislocation can be seen to originate from a distortion of the crystal boundary and have moved inwards into the crystal. Right: A screw dislocation. A part of the crystal is translated one intermolecular distance to the right in the figure. The dislocations are shown in cubic crystal lattices to simplify the drawing.

dislocation, a part of the crystal is translated one intermolecular distance or
more relative to the rest of the crystal, as depicted in the right hand side of
figure 2.2.

Dislocations most commonly originate at the boundaries between crystals,
where local stress concentrations can arise. When the stress is increased
the crystal can deform by a gradual movement of the dislocations. The
dislocation move through the crystal lattice by either *glide* or *climb*. A
dislocation is said to move by glide, when it successively moves across planes
of molecules, called slide-planes. The slide planes are normally the planes
with the highest molecule density, which for ice crystals are the basal planes.
An example of basal plane glide is shown in figure 2.3. There is no favored
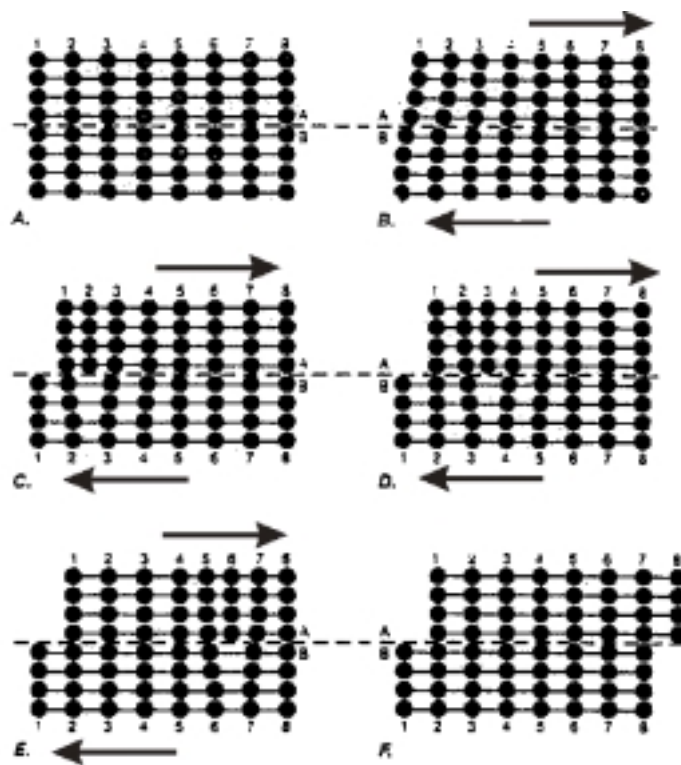


Figure 2.3: A perfect crystal (A) is subject to a horizontal stress (B). A dislocation
forms at one of the edges (C) and glides on the slide-plane through the crystal (D, E),
until it emerges at the other edge (E). Adapted from [Madsen, 1997].

direction for glide in the basal plane of an ice crystal. Glide can also take
place along other planes than the basal plane, but a much greater stress is
needed for this than for glide of basal planes. Glide of basal planes induces
proton and ionization defects.

When the dislocation is moving out of the slip plane and into another plane, it is said to move by climb. The climb movement requires transport of mass by diffusion of molecules to or from the half plane. Although the dominant process for moving dislocations in ice is glide, climb may also contribute significantly [Poirier, 1985].

## 2.3 Deformation of ice

*Stress* is defined as the force applied to an area. The stress can be resolved into components parallel and perpendicular to the surface it is acting upon, called *shear* and *normal* stress respectively. When a body is subject to a stress it will change in shape and dimension. The deformation of the body is called *strain*, and the change in strain with time is called the *strain rate*.

### 2.3.1 Deformation of a single crystal

If a crystal is subject to a stress it will start deforming by gliding of the basal planes, if the stress has the slightest component in the direction of the basal planes [Duval et al., 1983]. If the stress is parallel to the basal planes, the deformation will be rapid, and the crystal is said to be an easy glide crystal. The applied stress induces crystal defects. The creation of crystal defects is associated with some energy and counteracts therefore the deformation. Even low stresses results in a deformation of the crystal, since dislocations in the crystal only requires a minute amount of energy to move. If the stress is parallel to the c-axis of the crystal, the stress needed for deformation of the crystal is 100 times the stress needed for deformation by basal glide [Paterson, 1994]. Crystals oriented in this way are denoted hard glide crystals.

### 2.3.2 Deformation of polycrystalline ice

Each individual crystal in the polycrystal is confined by its neighbours, so the glide of the basal planes has to be accompanied by a rotation of the crystal. Apart from glide of the basal planes and rotation, other processes, e.g. recrystallization and grain boundary sliding contributes to the deformation of polycrystals.

The individual crystals within the polycrystal are generally not favorably oriented for glide of the basal planes, so the deformation of polycrystalline ice is more slow than the deformation of a single crystal.

Deformation is strongly temperature dependant. High temperatures lead to rapid deformation. Extensive deformation tests have been made in laboratories, and the typical development of strain and strain rate as function of applied stress has been found. This has lead to the formulation of a constitutive relation between the strain rate and the applied stress, also called the flow law of ice or Glens law. Deformation processes and constitutive relations are described further in e.g. [Alley, 1992, Paterson, 1994].

Deformation of the individual crystals influences the development of fabrics in ice sheets. In newly fallen snow the c-axis orientations are isotropically distributed. As the ice becomes subject to an increasing stress, each crystal in the polycrystal deforms preferentially by sliding of the basal planes. Rotation of the crystal accompanying the basal plane sliding will lead to a re-orientation of the crystal c-axis, that depends on the dominating stress system. The fabric of the ice can therefore reveal the stress history of the ice. If the ice is subject to uniaxial compression[1] the c-axes will rotate toward the axis of stress and create a strong single maximum. A strong vertical single maximum will also develop in ice subject to a horizontal shear stress. This has been observed in e.g. the Camp Century, the Byrd and the GRIP ice cores [Herron and Langway, Jr., 1982, Thorsteinsson et al., 1997]. A review of the fabric formation processes can be found in e.g. [Alley, 1988, Alley, 1992, Paterson, 1994]. Anisotropic c-axes orientations has made it necessary to develop anisotropic flow laws, which are described by e.g. [Azuma and Goto-Azuma, 1996, Castelnau et al., 1998].

## 2.4  Crystal growth and recrystallization

Three different regimes of recrystallization have been identified in polar ice sheets. They are thoroughly described in e.g. [Alley, 1992, Duval and Castelnau, 1995], although these authors do not agree about the terminologies of the regimes. I will follow the terms of Thorsteinsson (1996) in this description.

In the upper part of ice sheets the mean crystal size increases with depth due to crystal growth by grain boundary migration. This is called the *normal grain growth* regime. Below the normal grain growth regime one finds the *rotation recrystallization* or *polygonization* regime, in which large crystals are divided into smaller crystals due to the applied stress, and the increase in mean crystal size ceases. Finally, close to the bottom under the right conditions the *migration recrystallization* or *dynamic recrystallization* regime

---

[1]compression in one direction, extension in the other two

is situated, in which the dominant recrystallization form is believed to be nucleation and rapid growth of new crystals.

## 2.4.1 Normal grain growth

In the normal grain growth regime[2], large crystals grow on the behalf of smaller crystals. The boundaries migrates as molecules on the boundaries of the small crystals separates, moves and segregates to larger crystals, due to a curvature-induced boundary pressure gradient. The process is driven by the decrease of free energy that lies in the reduction of the total crystal surface area.

The normal grain growth can be described by an equation originally developed for use in metallurgy, e.g. [Atkinson, 1988]:

$$D^n = D_0^n + kt, \tag{2.1}$$

where $D$ and $D_0$ are linear dimensions of the crystal size at time $t$ and $t_0$ respectively, $k$ is the growth rate and $n$ is a constant. The growth rate, $k$, is given by the Arrhenius equation:

$$k = k_0 \exp(-\frac{Q}{RT}), \tag{2.2}$$

where $k_0$ is a constant, $Q$ is the activation energy for grain boundary self-diffusion, $R$ is the universal gas constant and $T$ is the temperature.

$n$ lies generally between 2 and 3 [Alley et al., 1986a]. Thorsteinsson et al. (1997) found that a value of $n = 2.5$ gave the best fit to the normal grain growth regime of the GRIP ice core, but $n = 2$ is normally used to describe crystal growth in firn and ice, e.g. [Gow, 1969, Alley and Woods, 1996].

The normal grain growth regime is dominant in the upper part of the ice sheets. In Greenland it has been found in the uppermost 600 m in the Camp Century [Herron and Langway, Jr., 1982], and 700 m in the GRIP and GISP2 ice cores [Thorsteinsson et al., 1997, Alley and Woods, 1996]. In Antarctica the regime has been found in the uppermost 600 m of the Byrd ice core [Gow and Williamson, 1976], whereas it seems to be prevailing throughout the Dome C ice core (900m) [Duval and Lorius, 1980] and more than 2000 m down in the Vostok core [Duval and Castelnau, 1995].

---

[2]here grain refers to crystal, since grains and crystals only can be distinguished in the upper few meters of firn [Gow, 1969]

**Effect of normal grain growth on fabric**

Normal grain growth is assumed not to have any influence on the formation of fabric in ice sheets [Alley, 1992]. On the contrary a strong single maximum fabric can influence the normal grain growth, since the boundaries between individual crystals will be low angle boundaries, which have low mobility and thereby the crystal boundary migration decreases.

## 2.4.2   Polygonization

The increase in mean crystal size ceases at a certain depth where the in-creased stress leads to polygonization of crystals. Large crystals are divided into smaller crystals by a gradual misorientation of the crystal lattice due to high stress. As the crystals favorable oriented for deformation by sliding of the basal planes are deformed, the stress in the ice is gradually trans-ferred to hard glide crystals, poorly oriented for sliding of the basal planes [Duval and Castelnau, 1995]. This results in bending and twisting of the hard glide crystals. Due to the bending, dislocations are created at the boundaries of the crystals, and these are moved inwards in the crystal lat-tice, increasing the dislocation density. To minimize the deformation energy, the dislocations arrange themselves in a sub-grain boundaries, dividing the crystal in two areas or more with slightly different c-axis orientation (see figure 2.4) [Hirth and Lothe, 1982]. The polygonization process is driven by
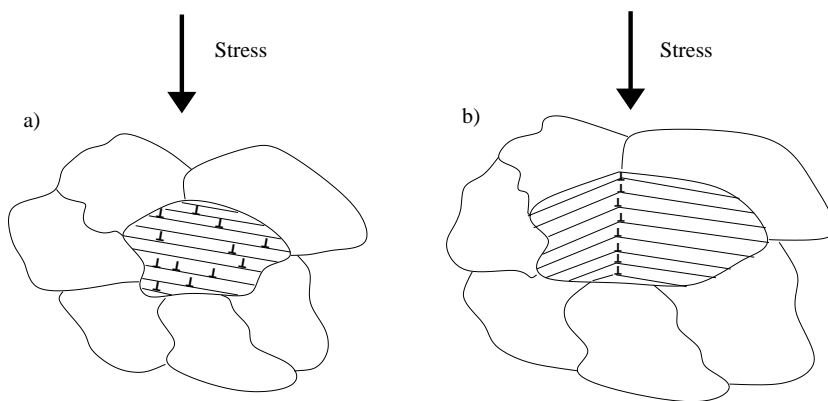


Figure 2.4: The bending of a crystal due to the stress induces dislocations (illustrated by inverted T), which moves inwards into the crystal along the basal planes (illustrated by the parallel lines) (a). The dislocations can be collected in dislocation bands forming sub-grain boundaries (b).

deformation energy stored as deformation-induced dislocations.

As the stress increases, the angle between sub-grains increases. The sub-grains are normally considered separate grains, when the angle between them are larger than 10–15° [Poirier, 1985]. This limit is though a question of definition, and could also attain other values.

In thin sections from deep ice cores a slight variation of colour and intensity across a crystal is often seen. This feature, called a *strainshadow*, is due to a beginning misorientation of the crystal lattice initiating a bending of the crystal. It is the first sign that the polygonization process has started on the crystal.

Although grain boundary migration continues in the polygonization regime, the polygonization is counteracting the normal grain growth, since large crystals are divided into smaller. Below the normal grain growth regime, there is a large depth interval where the two processes appear to be in equilibrium, and the mean crystal size is almost constant. This has been observed in e.g. the Byrd, GRIP and GISP2 ice cores [Gow and Williamson, 1976, Thorsteinsson et al., 1997, Alley and Woods, 1996].

**Effect of polygonization on fabric**

Polygonization influences the fabric by dividing crystals with a given orientation into two or more crystals with almost the same orientation. If the polygonization favours crystals with a certain direction, these will obtain a larger weight in the fabric. On the other hand, if polygonization does not favour a certain direction, the result is only a local surplus of the orientation of the polygonized crystal. It will not effect the overall fabric, if the statistics are comprehensive enough.

## 2.4.3 Migration recrystallization

The migration recrystallization process is nucleation of new crystals and rapid migration of grain boundaries. Old crystals have a high dislocation density, and hence much stored strain energy. New, almost perfect crystals with no dislocations are therefore able to grow at a high rate on the behalf of the old crystals, which will minimize the energy. Although the typical deformation energy for the polycrystal is too low to drive migration recrystallization, the stress can be build up in badly oriented crystals due to the unevenly distribution of stress and deformation within the polycrystal, and the necessary amount of deformation energy is reached [Duval et al., 1983]. The process requires a high temperature, close to -10°C [Duval and Castelnau, 1995].

Migration recrystallization is believed to result in large interlocking crystals [Duval and Castelnau, 1995], which is found in the lowermost 350 m

of the Byrd ice core [Gow and Williamson, 1976] and in the lowermost 200
m of the GISP2 and GRIP ice cores [Alley and Woods, 1996, Thorsteins-
son et al., 1997], although the latter not definitely is ascribed to migration
recrystallization [Thorsteinsson et al., 1997].

**Effect of migration recrystallization on fabric**

In laboratory studies, deformation tests are carried out at high tempera-
tures, to speed up the process, and migration recrystallization is inevitable
in this case.  Therefore the influence of migration recrystallization on the
development of fabric is very well known.  Generally the new crystals have
a different orientation than the surrounding crystals and the boundaries be-
tween the crystals are therefore high angle boundaries [Alley et al., 1995b].
The new crystals tend to form in positions favorable for glide of the basal
planes, which is with the c-axes positioned between the axes of compression
and tension.  For uniaxial compression this results in a girdle fabric, which
in natural ice only has been observed in the lower part of the Byrd ice core
[Gow and Williamson, 1976]. In simple shear, a second maximum is expected
to form close to the shear plane. This type of fabric has not been observed
in polar ice cores.

## 2.4.4   Effects of impurities

The main process in the change of crystal size and shapes is the crystal
boundary migration.  Migration is an ongoing process in the ice sheet, but
it can be impeded by air bubbles or impurities which have zero of very low
mobility.  According to Alley et al. (1986a), the interaction energy between
impurities and the crystal boundaries causes the impurities to be concen-
trated on the boundaries.  Microparticles and air bubbles will replace crystal
boundary area, whereas soluble impurities can dissolve in the crystal lattice
at the boundary [Alley et al., 1986a].
    A migrating boundary separating from a trapped air bubble or micropar-
ticle has to replace the grain surface area that the impurity fill, which is
energy consuming.  Soluble impurities causes crystal lattice defects at the
boundaries. Before the soluble ladden boundary is able to migrate, the defect
has to be moved inwards into the crystal, which increases the deformation e-
nergy, and hence decreases the boundary mobility energy [Alley et al., 1986a].
    Alley et al. (1986a) made a quantitative analysis of the effect of air bub-
bles, microparticle drag and impurities on the crystal boundary migration.
They found that bubbles do not appear to influence the grain boundary mi-
gration significantly.  The drag effect of microparticles is too small to have

any effect on the grain boundary migration, unless the amount is so large that the ice looks dirty, which was also stated by [Duval and Lorius, 1980]. The drag effect from soluble impurities is shown to be of a significant size to impede crystal boundary migration, and it is supported by a data analysis from Dome C [Alley et al., 1986b]. Further indications of the detainment of crystal boundary migration by soluble impurities have been supplied from the Dye 3, GRIP, GISP2 and Dome F ice cores [Langway, Jr. et al., 1988, Thorsteinsson et al., 1997, Alley and Woods, 1996, Azuma et al., 2001].

When the boundaries with impurities migrate, they must either drag the impurities along, or move faster than the impurities can diffuse. This gives rise to a low and a high velocity regime for the crystal boundary migration. The transition velocity for escape from impurities has not been calculated, but an estimate is several orders of magnitudes higher than migration rates observed in normal grain growth regimes in glacier ice [Alley et al., 1986a]. A jump from the low to the high velocity regime can take place for higher temperatures and changed stress, and is essentially what happens for migration recrystallization [Duval and Castelnau, 1995].

**Effects of impurities on fabric and deformation**

Indirectly the impurities effect the fabric by impeding the crystal growth, resulting in small crystals, which more easy develops a preferred fabric orientation by rotation [Paterson, 1991]. A direct influence of impurities on crystal fabric formation has not been investigated.

The effects of impurities on deformation has been widely discussed. Deformation tests in the early sixties indicated that impurities enhanced the deformation of polycrystalline ice, but this was since rejected [Paterson, 1991]. Recently the idea has experienced a revival. Cuffy et al. (2000) believes that variations in crystal size accounts for about 30% of the enhanced shear strain rate in Wisconsin ice at Dye 3.

## 2.5   Textures and fabrics of the GRIP ice core

Thorsteinsson (1996) made an extensive analysis of the textures and fabrics of the GRIP ice core, which has also been reported in Thorsteinsson et al. (1995) and Thorsteinsson et al. (1997). Below is a short description of the results throughout the core in general and around 2000 m depth especially, since my samples are taken here.

The mean horizontal crystal diameter, measured by the linear intercept method (See section 3.2.1 on page 22), is observed to increase linearly with

time from about 1 mm near the surface, to about 4 mm at a depth of 700
m (see figure 2.5). This is the normal grain growth regime. From here, the
mean crystal size is almost constant — the polygonization regime — until
the transition between Holocene and Wisconsin, at a depth of 1625 m, where
a decrease over a short distance is observed. This is believed to be due to the
influence of impurities on the normal grain growth. The horizontal crystal
diameter at a depth of 1982 m is 2 mm, which is the smallest crystal diameter
in core, except for the top 100 m. The crystal diameter stays fairly constant,
until the Wisconsin–Eemian transition at a depth of 2790 m, where layers
of coarse grained ice alternates with layers of fine grained ice. The crystal
diameter in this region is found to vary strongly with the climatic parameters.
In the bottom 100 m the crystal diameter increases dramatically, until the
silty ice just above bedrock is reached, where the crystal diameter is very
small again.

The crystals are elongated already at
a shallow depth. A more or less constant
ratio between the horizontal and the ver-
tical diameter of the crystals is found in
the top 700 m to 1.22. In the Holocene
and Wisconsin parts of the polygoniza-
tion regimes it is found to be 1.32 and
1.36 respectively.

The fabric is randomly oriented at a
shallow depth of the ice core, but with
an indication that a strengthening of the
fabric has already started. The strength-
ening increases rapidly until a depth of
about 500 m, where the increase contin-
ues although at a more moderate rate.
No sharp fabric contrast is found at the
Holocene–Wisconsin transition, but the
strength of the fabric continuous to in-
crease. At a depth of 2000 m it has de-
veloped a degree of orientation of $R \approx$
85% (see section 3.3.5 on page 27). With
some small variations, the single maxi-



Figure 2.5:   The mean crystal size
profile from the GRIP ice core. From
[Thorsteinsson, 1996].

mum fabric strengthens further, until the warm stages of the Eemian ice,
where a girdle-like fabric, inclined 20° from vertical is observed. The fabric
in the fine grained ice below Eem, is again of strong single maximum type,
and in the coarse grained ice near the bottom, the fabric appear to be an
elongated and stretched single maximum fabric.

# Chapter 3

# Theory of measurements

In this section, I will give an introduction to the optical properties of ice crystals and describe how crossed linear polarizers are used to study ice crystals. Then I will describe the most common methods for determining the textures of ice crystals. The methods to measure the fabrics of ice crystals are described as well, together with a description of how fabric diagrams are made and how statistical parameters can be used to describe the fabrics.

## 3.1    Optical properties of ice

Ice is a doubly refracting crystal. When light enters an ice crystal, it is split into an ordinary and an extraordinary wave. The velocity of the ordinary wave is constant in all directions in the crystal, whereas the velocity of the extraordinary wave is slower than the ordinary wave and depends on the orientation of the crystal [Hobbs, 1974]. The velocity of the two waves is only equal when light travels in one direction, which is called the optic axis and is coincident with the crystal c-axis. The electric vector of the extraordinary wave oscillates along the optic axis, and the electric vector of the ordinary wave oscillates perpendicular to the extraordinary wave (see figure 3.1).

When two linear polarizers are crossed and placed over an uniform light source, the light will be extinct by the polarizers. If an ice crystal is placed between the two polarizers, the superposition of the ordinary and extraordinary waves as the light emerge from the crystal will generally be elliptical polarized due to the phase difference between the two waves. The light will therefore have a component of the electric vector in the direction of the upper polarizer, and light will be transmitted through it. The phase difference between the two waves, and hence the brightness of the crystal seen between the crossed polarizers, depends on the angle of the incident light to the optic
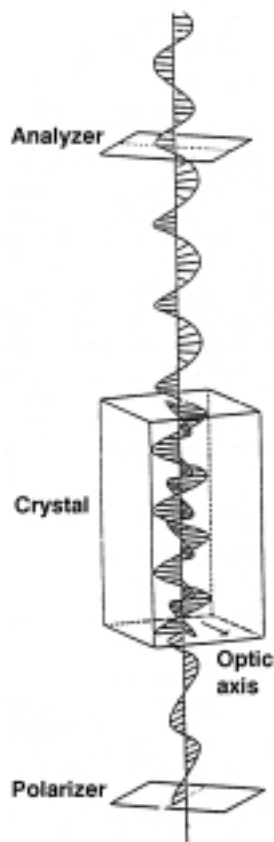
Figure 3.1: The path through an ice crystal of a linear polarized light wave. Due to the double refractivity of the crystal, the wave is split into an extra ordinary wave, and an ordinary wave. When the light emerges from the crystal the two waves are generally out of phase due to different travel velocities, and a component of the wave passes through the analyzer. Adapted from [Madsen, 1997].

axis. If the projection of the optic axis onto the plane of polarizers is parallel to the electric vector of the incident light, there is no extraordinary wave. If the projection is perpendicular to the electric vector, there is no ordinary wave. In these cases the crystal appear dark. If the optic axis is parallel to the direction of propagation of the light, there is no extraordinary wave, and the crystal appear dark no matter how it is rotated in the plane of the polarizers.

The wavelengths of the visible light have different velocities through the ice crystal, and the crystals can appear coloured when displayed between crossed polarizers. When the ice crystal thickness exceeds about 0.4 mm, the short wavelengths in the visible spectrum (violet) becomes just out of

phase when the waves emerges from the crystal. These colours are subtracted from the white light and the crystal have the complementary colour of green-yellow [Hobbs, 1974]. A slightly thicker crystal yields colour subtraction of the green, and the crystal appears red and so on. These colours are the first order interference colours, and a further increase in the crystal thickness give interference colours of higher orders. When the crystal is just thicker than 1 mm, it will exhibit interference of higher orders than 3, and the crystal will appear to have a peculiar white colour, due to the irregular mixing of the waves of different orders [Hobbs, 1974]. Interference colours can also be seen when light passes more than one overlapping crystals, due to the (possible) different orientation of the crystals.

The optical properties are used to study the orientation of ice crystals. A sample of the ice is placed on a glass plate, cut to a thickness of about 0.5 mm and placed under crossed linear polarizers, normally in a Rigsby stage (See section 3.3.1).

## 3.2   Measurement of textural parameters

When a thin section is placed between crossed polarizers, the different crystals can be distinguished, and the size and shape, or the *texture* of each crystal can be found.

Here one should remember, that the dimensions of crystals seen in a thin section are not representative for the three dimensional size of the crystal. Ice crystals, being space filling, are closely packed, so a section through a polycrystal will intersect some of the crystals at their maximum diameter, while only the corner of other crystals are intersected. So the observed crystal "size" is the area of the crystal in that particular section.

It is also important to specify in which direction the thin sections are made. Crystals can exhibit shape anisotropy in some directions, while they are isotropic in others, e.g. under vertical uniaxial compression, crystals will be vertically flattened and horizontally isotropic. A horizontal thin section under these circumstances will only give information about the horizontal extension of the crystals, whereas a vertical thin section also can give informations about the vertical extent of the crystals, which is important if the ice is dominated by a layered structure.

### 3.2.1   Mean crystal size

The most common parameter used to describe the texture of an ice sample is the mean crystal size. The term "size" has been widely used in the literature

to cover measured or calculated quantities concerning the spatial extent of ice crystals in both, one, two and three dimensions. I will attempt to use the word size, only for the spacial extend of the crystals. The areal extend of the crystals are then termed *area*, and the linear extend, *diameter*.

Several methods have been used to determine the average crystal size in ice thin sections [Jacka, 1984]. Among them I will shortly describe the most common two — the mean area method and the mean linear intercept method — together with the newly developed individual crystal area method.

### The mean area method

When using the mean area method the number of crystals, $N$, within an area, $A$, of a sample is counted. Crystals on the boundary of the measured area are counted as a half. The mean crystal area is found by: $A/N$. This method is e.g. used by [Gow and Williamson, 1976, Duval and Lorius, 1980, Jun, 1995]. A problem with this method is that information about a possible size anisotropy, i.e. a flattening in one dimension, is lost.

### The mean linear intercept method

Using the mean linear intercept method the number of crystals, $N$, that intersects a test line with length, $L$, is counted. Crystals just touching the intercepting line and crystals at the end points of the test line are counted as a half. The mean diameter of the crystals is: $\bar{d} = L/N$. This method is e.g. applied by [Langway, Jr. et al., 1988, Alley and Woods, 1996, Thorsteinsson et al., 1997].

The linear intercept method depends on the orientation of the test lines. To cover all directions of the sample one can apply test lines evenly distributed in all directions or use a circle as a test line. But when using test lines in only one direction one obtains information about the crystal diameter in that particular direction. This is of interest if the crystals e.g. are elongated due to compression. By applying test lines parallel and perpendicular to the elongation direction, information about the mean crystal diameter in these two dimensions is obtained.

### The individual crystal area method

The above mentioned methods are both based on a calculated mean crystal size. The individual crystal area method determines the area of each individual crystal in a sample by means of image processing software and several images taken between rotating crossed polarizers. The method is described in details in section 4.4. A mean crystal area of the measured sample can

be calculated from the individual crystal areas. This method has been used to measure crystal areas on the Dome F core [Azuma et al., 1999] and on the EPICA: Dome C core [Gay and Weiss, 1999] with two nearly identical methods, developed individually. An early attempt to measure the crystal size in sea ice by image processing methods was made by Eicken (1993).

Since each crystal area is measured in pixels, one can extract detailed information about the distribution of the textural parameters in a sample. Several parameters such as aspect ratio and elongation direction can also be measured by the image processing software, giving information about a possible size anisotropy (see section 3.2.3).

## 3.2.2 The sectioning effect

All methods to determine crystal sizes measures a one- or a two-dimensional quantity of a three dimensional structure. Since the sectioning of the crystals seldom intersect the crystals at their maximum diameter, the measured diameter or area is not a satisfactory expression for the real diameter or area. Some authors calculates a three dimensional size from their measurements, but are then obliged to make an assumption about the extend of the crystal in the third dimension, not represented in the thin section.

Several authors have tried to compensate for the sectioning effect by adding a constant factor to the mean diameter or area. Such a correction factor depends on the shape of the crystals. A section through closely packed spherical crystals of equal size will give an area which is 2/3 of the true maximum cross sectional area [Underwood, 1970]. Correcting a mean area measurement using this yields a correction factor of 3/2, which is used by [Alley and Koci, 1988, Alley and Bentley, 1988]. When measuring crystal diameters with the linear intercept measurement, an additional sectioning is introduced. Therefore linear intercept measurements should be corrected by a factor $\sqrt{3/2} = 1.22$ [Alley and Woods, 1996]. Other suggested correction factors for the linear intercept measurements are 1.75 [Jacka, 1984] (calculated from observations in metallurgy) and 1.78 [Fisher and Koerner, 1986] (no statement of the origin). The assumption of spherical crystals do not hold, since these are not space filling. No regular polyhedron with plane sides is space filling in three dimensions [Atkinson, 1988], so a theoretical correction factor for the sectioning effect can only be approximated.

Another way of compensating for the sectioning effect was made by Gow (1969) and Gow et al. (1997), who measured only the 50 largest crystals in a sample, and used the average value of these as the mean crystal area. This method is not recommendable since it depends on the shape of the size

distribution in the sample.

Using three vertical and one horizontal thin section from between 221 and 2807 m depth, Thorsteinsson (1996) calculated a correction factor of the mean diameter for GRIP ice core, to between 1.2 and 1.4.

In the latest years mean crystal size data commonly have been presented uncorrected, e.g. [Fisher and Koerner, 1986, Thorsteinsson et al., 1997, Azuma et al., 1999]. In the following sections I will continue this practice.

### 3.2.3   Other textural parameters

Hitherto information about shapes of ice crystals have been given quantitatively as description of typically shapes (i.e. twisted and interlocked or regular). The linear intercept method can give a ratio between e.g. vertical and horizontal diameter of the crystals. With the individual crystal area method, other parameters can now be measured qualitatively, since every single crystal is measured and described in pixels. Parameters describing the orientation and the flattening of crystals, can be calculated using the image processing software. [Azuma et al., 1999].

The textural parameters can also be described by distributions, which until now have been a laborious task, although it has been done. Thorsteinsson et al. (1997) calculated the diameter distribution for three samples from the GRIP ice core.

## 3.3   Measurement of fabric

The most common method to describe the fabric of ice is to measure the orientation of the c-axes in the crystals in a thin section. This is normally done using a universal stage also called a Rigsby stage.

### 3.3.1   The Rigsby stage

A glass plate with the fixed thin section is placed in the Rigsby stage between two crossed polarizers (see figure 3.2). In the rest position, the sample can be rotated about two axes in the horizontal plane, $A_2$ and $A_4$. The sample can also be rotated 360° around an axis perpendicular to the sample plane, $A_1$, and the whole stage can be rotated around the same axis, $A_5$, which is used for control.

The principles of measurements with the Rigsby stage is to observe one crystal at the time, place the eye directly above the crystal, and rotate the stage axes until the c-axis of the observed crystal is parallel to the line of

sight. The angle between the c-axis and the direction perpendicular to the sample plane — the tilt angle — and the azimuth angle can now be read on the stage axes dials. These two angles constitute was is called *the extinction angle*. In this position, the reading of the angles is said to be polar. If the angle between the c-axis and the plane of the sample is less than 45°, the stage axes are rotated so the c-axis of the crystal is placed in the plane of the polarizers, parallel to the polarization of the incoming light. The angle reading in this case is said to be equatorial. A detailed description of how to measure with the Rigsby stage can be found in Langway, Jr. (1958).
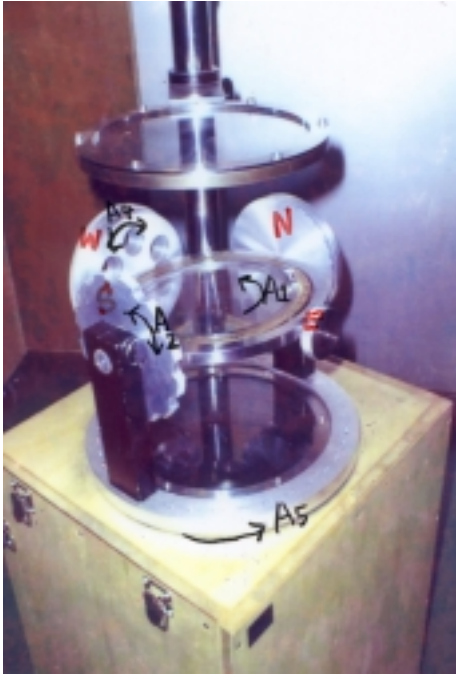


Figure 3.2: The Rigsby stage. The stage axes $(A_1, A_2, A_4$ and $A_5)$ are indicated on the picture.

If the c-axis of a crystal is in the plane of the sample or within a few degrees, it is very difficult to determine the correct extinction position. An error of 90° in determining the azimuth extinction angle can easily be made for crystals with this orientation.

Due to the refraction between ice and air, the measured angles have to be corrected. For the polar readings the corrections are made using Snell's law [Langway, Jr., 1958]. For the equatorial readings the theoretic correction do not hold, and an empirical correction is needed [Kamp, 1962].

Langway, Jr. (1958) estimated the maximum error of the readings of the Rigsby stage to be ±5°. This error estimate included an error in determining the exact extinction angle, a wrong reading of the dials on the stage axes, an offset if the observer is not placed exactly vertical over the crystal, and mechanical errors in the stage.

To ameliorate the Rigsby stage, a semi-automatic device was proposed by e.g. Lange (1988), where the reading of the angles were made with optoelectronic sensors, and the refraction correction and data handling was computerized. This setup facilitated the c-axes measurements, although the basic measurements were the same.

### 3.3.2   Ultrasonic measurements

Another way of characterizing the fabric of ice, is by ultrasonic measurements. The ultrasonic measurement do not measure the c-axis of the individual crystals, but describes the fabric in a section of the ice. The velocity of ultrasonic waves moving through an ice crystal depends on the direction between the propagation direction and the c-axis. If the wave is parallel to the c-axis it moves faster than if it is perpendicular to it. In isotropic oriented ice, the velocity will be the same in all directions. As ice crystals develops a preferred orientation, the ultrasonic velocity will increase in this direction. If the velocity is measured both along and perpendicular to an ice core, the difference between the two measurements can determine the strength of the fabric. This has been done in various set ups for e.g. the Byrd [Bentley, 1972], the Dye 3 [Langway, Jr. et al., 1988] and the GISP2 ice cores [Anandakrishnan et al., 1994].

### 3.3.3   The Automatic Ice Fabric Analyzer

An Automatic Ice Fabric Analyzer (AIFA) has been developed by Wang and Azuma (1999). The instrument is operating after the same principles as the Rigsby stage, but all crystals in a sample is observed at once by a CCD camera, and the c-axis orientation of each crystal is calculated from the measured intensity from different camera positions. The instrument is described in detail in section 4.5. Fabric measurements with this instrument can be made easier and with more comprehensive statistics than previously. The instrument has been used to measure the fabrics of the Dome F ice core [Azuma et al., 1999]. The accuracy of the instrument is stated to be $\pm 0.34°$ for the azimuth angle and $< \pm 2°$ for the tilt angle [Wang and Azuma, 1999].

### 3.3.4   Fabric diagrams

To illustrate the orientation of the c-axes, they are plotted as points in a *fabric diagram*. Each c-axis is represented as a direction through the center of a sphere, and the intersection of the axes with the lower hemisphere is projected onto the plane perpendicular to the line of sight (see figure 3.3). The most common used projection is the Lamberts equal area projection, in which a unit area on the projected plane corresponds to a unit area on the hemisphere [Thorsteinsson, 1996].

Earlier, fabric diagrams were presented with contours of the number of crystals within 1% of the total area. This was abandoned when it was shown that this parameter did not have any statistical significance.
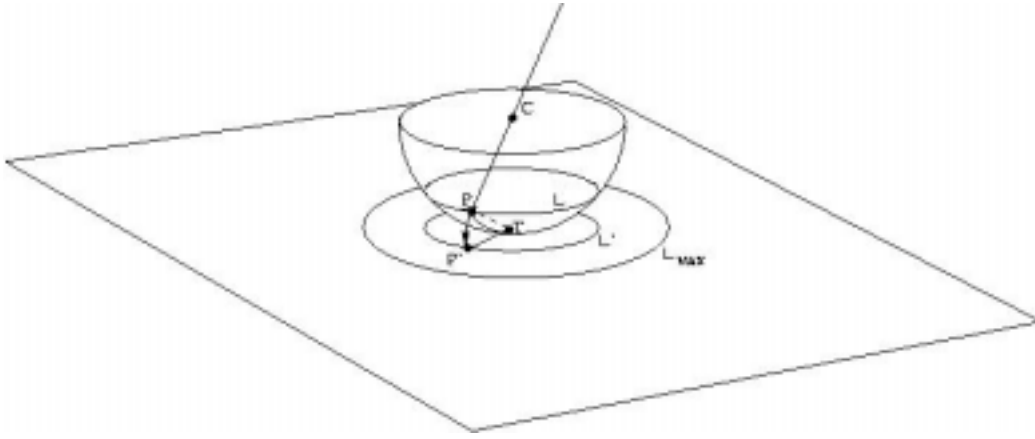
Figure 3.3: The Lamberts equal area projection. Each c-axis is represented as a direction through the center, C, of a sphere. The intersection between the line and the lower hemisphere, P, is projected onto the plane in the point, P',where the distance TP' is given by the chord lengthTP.

### 3.3.5  Statistical parameters

The most commonly used statistical parameters to characterize the fabric of ice crystals are the normalized degree of orientation, $R$ and the half-apex angle of a cone containing 90% of the measured c-axes, $\alpha$ [Paterson, 1994].

$R$ is a measure of the rectification of the c-axes and is given by:

$$R = \frac{2 \cdot S - N}{N} \cdot 100\%, \qquad (3.1)$$

where $S$ is the length of the vector sum of all c-axes treated as unit vectors and $N$ is the number of measured c-axes. $R$ varies between 0% for a random distribution and 100% for completely parallel orientation.

$\alpha$ has the disadvantage of not taking the distribution of the c-axes into account, i.e. one can not from this parameter distinguish between a single maximum and a girdle fabric. To compensate for this, Thorsteinsson et al. (1997) calculated the spherical aperture, $\alpha_s$. The spherical aperture is the angle of a cone spanning a circle centered on the average c-axis in the fabric diagram, containing an uniform distribution of c-axes with the $R$-value of the measured distribution. $\alpha_s$ lies between 0° for a complete parallel c-axis distribution and 90° for a random orientation and is given by:

$$\alpha_s = \arcsin(\sqrt{2 \cdot \frac{1 - 1/N}{k}}), \qquad k = \frac{N - 1}{N - S}. \qquad (3.2)$$

As a mean of investigating fabric shapes, the eigenvalues of the cross product matrix (the cross product of a matrix with the c-axes given in Cartesian coordinates as components and its transpose) can be calculated. The eigenvalues are the length of the axes of an ellipsoid which best fits the distribution of the c-axes in a fabric diagram [Thorsteinsson, 1996]. The normalized eigenvalues are obtained by dividing the eigenvalues with $N$. A random fabric will have normalized eigenvalues $s_1 \approx s_2 \approx s_3 \approx \frac{1}{3}$. For a girdle fabric $s_1 \approx \frac{1}{5}$ and $s_2 \approx s_3 \approx \frac{2}{5}$, and for a symmetrical single maximum $0 \leq s_1 \approx s_2 \leq \frac{1}{6}$ and $\frac{2}{3} \leq s_3 \leq 1$.

The $q$-parameter, calculated by:

$$q = \frac{\ln\left(s_3/s_2\right)}{\ln\left(s_2/s_1\right)}, \qquad (3.3)$$

can be used to distinguish between girdle fabric and unimodal fabric. $q \in [0; 1[$ for a girdle fabric and $q \in [1; \infty[$ for a single maximum fabric [Thorsteinsson, 1996].

To characterize the fabric of the Dome F ice core, Azuma et al. (1999) calculated the median inclination, which is defined as the half apex angle of the cone in which half the measured c-axes are included. They also used the mean orientation of c-axes (MOC): The angle between the pole of the single maximum and the core axis.

# Chapter 4

# Measurements

In this chapter, I will describe the procedures of the three different types of measurements I have used to measure the textures and fabrics of the ice crystals in my samples. I will start with a short outline of how the GRIP ice core has been handled from the recovery until my sample preparation, and then I will describe how thin sections were prepared from the chosen samples. I have measured the textural parameters using the individual crystal area method, and the orientation of the c-axes has been measured using the Automatic Ice Fabric Analyzer. Finally I have made some measurements of the mean crystal area and diameter using the conventional methods: The linear intercept and the mean area methods.

## 4.1   Handling of the GRIP ice core

The GRIP ice core was drilled in a trench below the ice sheet surface. Immediately after recovery, the ice core was transferred to a science trench where it was logged, and then it was stored in a core buffer for a week at a temperature of about -25°C. The processing of the ice core took place in the science trench at a temperature that never exceeded -15°C. The core was cut in *bags* (0.55m long sections) after processing and shipped to Copenhagen, where it has been stored in a cold room at -25°C.

Gow (1994) observed post-drilling recrystallization in the Byrd ice core indicating that the ice had been exposed to high temperatures while stored, and migration recrystallization has taken place. According to Duval and Castelnau (1995) the migration recrystallization can only take place at temperatures higher than about -10°C. Since the GRIP ice core has been handled at temperatures below this, no or very little post-drilling recrystallization should have taken place in the ice core.

Langway et al. (1988) concluded from a study of the Dye 3 ice core from southern Greenland that no marked change in textures and fabrics was observed 5 years after drilling. Since the Dye 3 core was handled and stored in almost the same way as the GRIP ice core after recovery — except that the temperatures were slightly higher at the drill site — I assume that no significant changes in textures and fabrics have taken place in the GRIP ice core since the recovery.

## 4.2   Sample selection

I decided to use ice from the climate event IS3 because both $\delta^{18}O$, dust and soluble impurities had been measured on this part of the core, giving a good basis for comparison with these data.

I chose to use mainly vertical samples to include an examination of the vertical ice core stratigraphy in my study, and because both vertical and horizontal textural parameters can be found in vertical samples. Since the ice core is drilled at the ice divide, where there is almost no horizontal flow in the upper two third of the ice sheet, the crystal size is isotropic in the horizontal plane. No additional information can therefore be obtained from horizontal thin sections.

Samples were chosen to cover ice from before, during and after IS3. Instead of taking one sample from each bag covering IS3, samples were taken from six bags. Two bags in the cold stadial before IS3, two in the stadial after, and two bags from the warm interstadial, one at about the peak of the event and one in the transition phase from interstadial to stadial. The distinction between interstadial and stadials were made from the $\delta^{18}O$ curve. The samples from the last two bags mentioned will be referred to as interstadial samples and the others as stadial samples. A 1 cm thick and 55 cm long piece was cut from the side of the ice core in each bag with a width between 6 cm and 8 cm, depending on the previous sampling of the core. This piece was divided into 7 samples (see figure 4.1): 6 samples with a length of 8 cm and one with a length of 7 cm, so the total number of vertical samples was 42. The core was sampled in this way, partly due to the limited amount of available ice from the depth interval, partly to average out the annual cycle, which has a length of 1.5–3.5 cm. The continuous series of thin sections opens furthermore for an interesting comparison with high resolution impurity measurements.

Six horizontal samples were obtained to look for possible variations of the textural parameters in the horizontal plane. The samples were taken from the bottom of the bag in two series of three samples spaced about 9 cm, as
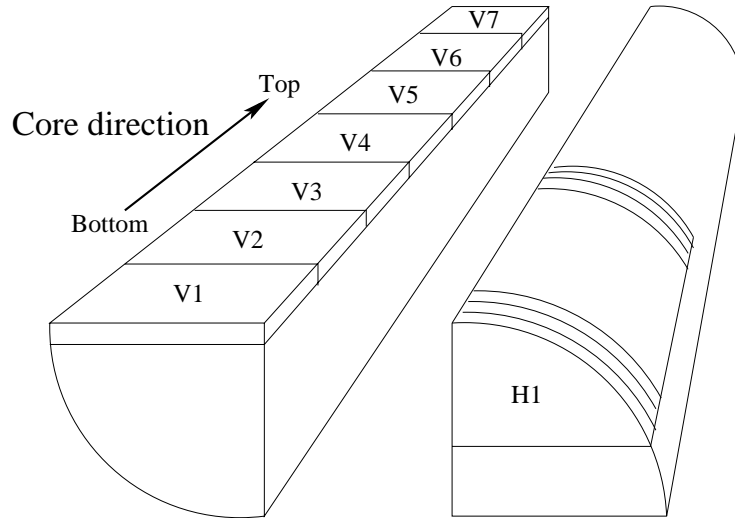
Figure 4.1: Sampling of the core. Left: Vertical samples. Right: Horizontal samples.

depicted in figure 4.1. The bag numbers and depth of the ice can be seen in table 4.1. The depths of the vertical samplesare also shown in figure 1.3.

| Bag number | depth [m] | Mean $\delta^{18}$O [$^0/_{00}$] | Type of samples |
|------------|-----------|----------------------------------|-----------------|
| 3665 | 2015.20–2015.75 | -41.43 | Vertical |
| 3669 | 2017.40–2017.95 | -40.86 | Vertical |
| 3673 | 2019.60–2020.15 | -38.51 | Vertical |
| 3680 | 2023.45–2024.00 | -37.01 | Horizontal |
| 3681 | 2024.00–2024.55 | -36.51 | Vertical |
| 3687 | 2027.30–2027.85 | -40.13 | Vertical |
| 3690 | 2028.95–2029.50 | -42.18 | Vertical |

Table 4.1: Bag number, depth of the ice, mean $\delta^{18}$O value and type of samples.

All sample preparation was carried out in a cold room at a temperature of -15°C. The samples were cut with a bandsaw, so less than one millimeter ice was lost between each sample.

## 4.3  Preparation of thin sections

The thin sections were prepared during June 2000 in a cold room at a temperature of -15°C. Each sample was flattened on one side using a microtome

bench. After flattening, it was mounted on a glass plate with droplets of water along the sides. Few micrometers were then cut in the microtome bench so the top side surface appeared polished.

A photo was taken of each sample while it was still about 1 cm thick. The samples were placed on a black piece of cardboard and a lamp placed so the light fell in the plane of the sample from the core direction. With the sample in this set-up the stratigraphy of the ice is accentuated.

The samples were then thinned to a thickness of about 0.5 mm using the microtome bench. Each sample was put in a small plastic bag with a "zipper" to prevent sublimation and stored in a cold room at a temperature of -25°C.

The thin sections were in general in good conditions. Only a few samples got minor cracks during the microtoming process. But two samples got so severe cracks that a continuation of the microtoming process most likely would break them. These two samples were left uncovered in the cold room at a temperature of -15°C for sublimation. The sublimation rate was found to be 0.2 - 0.4 mm/day, very close to the values found by Thorsteinsson (1996) at a temperature of -20°C. The samples sublimated more at the edges than in the center which made them uneven. One sample (from 2027.53 m depth) became so uneven that I chose not to use it for the measurements. It almost vanished at the edges, but in the center it was still so thick that it exhibited interference of high order, so it was not possible to distinguish the crystal boundaries.

## 4.4   Measurements of textures

To measure the textural parameters in the 41 thin sections, I used a semi-automatic method based on image processing techniques. The method applies pictures of thin sections displayed under rotating crossed polarizers and a commercial image processing software (Image-Pro). The crystal boundaries is determined by a procedure applying different filters from Image-Pro based on the method described by Wang and Azuma (1999).

The first step of the method is to take pictures of the samples. The samples are placed in a sample stage fixed between the two crossed linear polarizers. The CCD-camera is fixed above the upper polarizer (see figure 4.2). The CCD-camera used is an Olympus 2500L with a macro function and a zoom lens, and the pictures were taken with the highest possible resolution: True colours pictures (RGB24) with a resolution of 1712x1368 pixels compressed with the JPEG format. The camera was zoomed so the sample filled the whole frame, giving a resolution of 16–18 pixels per mm. The macro
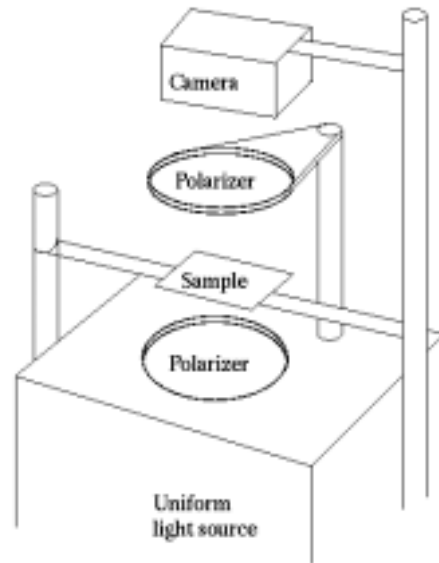
Figure 4.2: A sketch of the setup for taking pictures for the texture measurement procedure.

function was switched on, and the pictures were taken with a remote control. 4 pictures were taken of each thin section: One where the lower polarizer were parallel to the core direction, one where the polarizers were rotated about -10° (10° clockwise) from the first position, one at about 10° and one at about 20°. A precise angle control was not possible with the setup. The largest intensity contrast was found when the core direction was close to the direction of the lower polarizer. Therefore the pictures were taken with this orientation.

Due to the large intensity contrast around the core direction only 4 pictures were necessary. Wang and Azuma (1999) used images from 19 different angles spaced 5°, but it was found that running the procedure with more than 4 images gave more noise, and hence a poorer result.

The next step of the method is to determine the crystal boundaries for which the software package: Image-Pro from Media Cybernetics is used. The procedure is shown in the flow diagram in figure 4.3. Step 1-6 is repeated for each picture (each angle). Technical specifications of the individual steps can be found in Image-Pro (1999).

1. Each picture is smoothed by the Median Filter to diminish impulse noises. The filter is applied on an area of 5x5 pixels. The center pixel is replaced with the mean value of the intensity in its neighbourhood.

2. The picture is then split into three separate images: The red, green and blue colour channels of the picture. Each image is converted to grey-scale with intensity values from 0 to 255.

3. The crystal boundaries on each image (colour channel) are detected by the Sobel Edge Filter. This filter calculates intensity gradients in a 3x3 pixel neighbourhood to locate and highlight its edges (places with an intensity difference). The result is an image with high values where the edges are distinct and lower values where they are not.

4. The three images are added using the logical "ADD" operation: The gray scale value of a pixel in the resulting image is the sum of the values in the three images. Values larger than 255 is set to 255.

5. To delimitate the noise in the resulting image the Median Filter is again applied on 3x3 pixels.

6. The image is reduced to its skeleton by application of the Morphological Thinning Filter. This filter turns all pixels with a grey-scale value above a certain threshold value white, and the rest of the pixels are turned black. All lines are also thinned so they are one pixel wide. The threshold is set to be 40%.

7. The images for the 4 different angles are added together using the logical "OR" operation: Pixels that are "on" in either of the images will be "on" in the resulting image.

8. The Morphological Close Filter is applied on a 7x7 pixel circle in the resulting image. The effect of the Close Filter is to fill gaps and connect objects that are close together.

9. The Morphological Thinning Filter is again applied, this time with a threshold of 50%.

10. The Morphological Prune Filter is applied with a threshold of 50%. The effect of this filter is to remove protrusions.

11. The Morphological Dilate Filter is applied to a 2x2 pixel square to enlarge the crystal boundaries.

12. The crystals are counted and the textural parameters (area, aspect ratio, elongation direction, etc.) can now be found by the Measurement: Count operation.

The original Picture.

Step 1:
The Mean Filter is applied on an area of
5x5 pixels to diminish impulse noices.

Step 2:
The picture is split into the colour channels:
Red, Green, blue.

Step 3:
The Sobel Edge Filter is applied on the
three colour channels to determine edges.

Step 4:
The images of the three colour channels are
added.

Step 5:
The Mean Filter is applied on an area of
3x3 pixels.

Figure 4.3: Flow diagram of the crystal outline procedure.

Second angle    Third angle    Fourth angle

**Step 6**: The image is reduced to its skeleton by application of the Morphological Thinning Filter.

**Step 7**: The pictures from the four different angles are added: 1+2, 1+2+3, 1+2+3+4.

**Step 8**: The Morphological Close Filter is applied on a 7x7 pixel circle.

**Step 9**: The Morphological Thinning filter is applied again.

**Step 10**: The Morphological Prune Filter is applied to remove protrusions.

**Step 11**: The Morphological Dilate Filter is apllied to a 2x2 pixel square to enlarge the crystal boundaries.

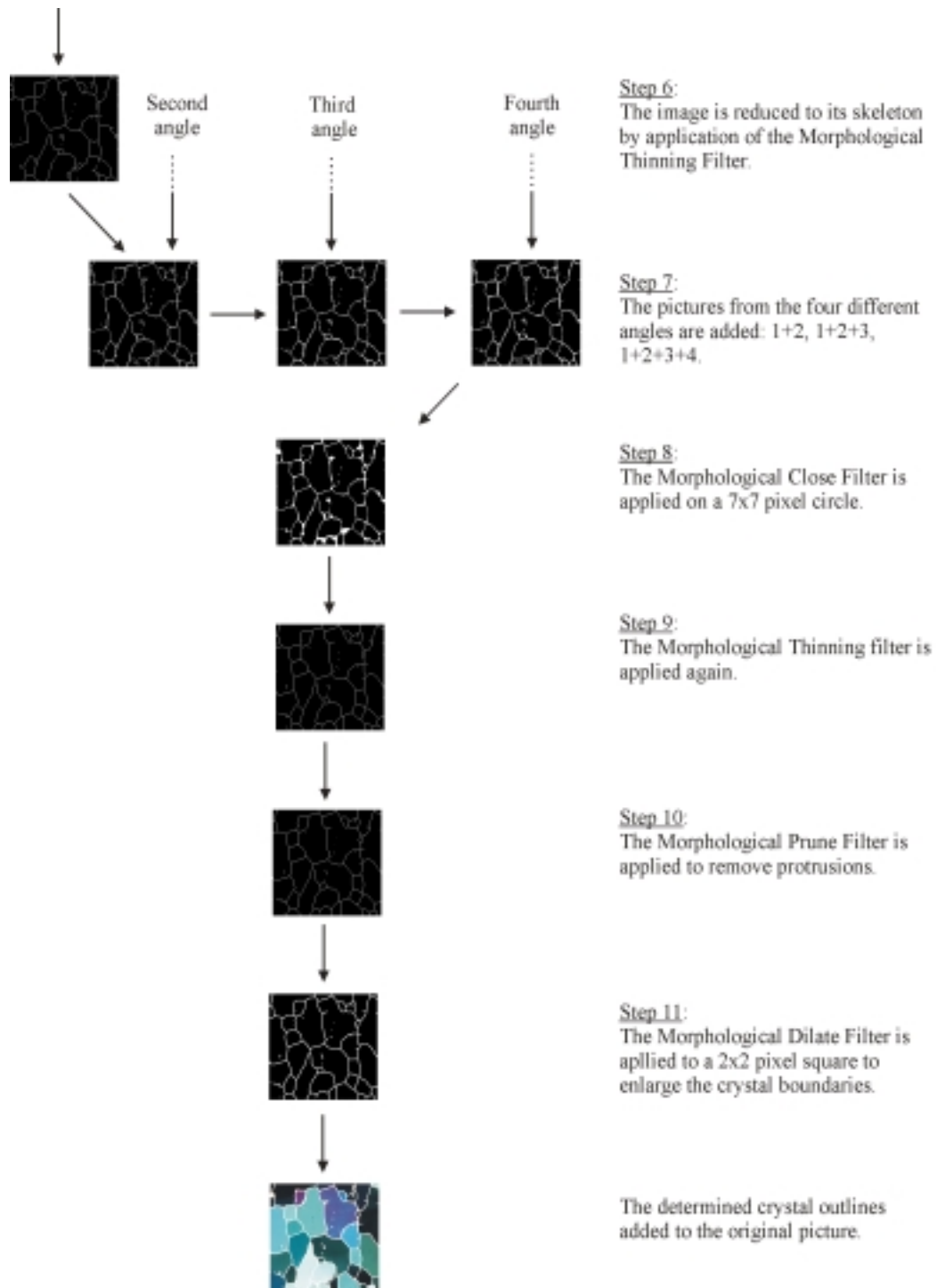The determined crystal outlines added to the original picture.

Figure 4.3 (continued)

### 4.4.1 Limitations of the filter parameters

The different filters used in the procedure can be applied to areas of different size and form (e.g. 3x3 pixels square, 7x7 pixels circle, etc.), some of the filters operates with thresholds, and yet other filters with other effects can be applied to the images. Each filter effect has its advantages but also its limitations as will be described below.

Other features than crystal boundaries, e.g. holes from entrapped air bubbles in the crystals, also displays an intensity difference and will disturb the crystal boundary detection. If a hole is close to the edge, it will be seen as part of a boundary, and the Close Filter applied to a too large area will connect it to the boundary. If there are several holes close together in a crystal, a wrong boundary can arise.

Some neighbouring crystals have very similar orientation and hence similar intensity, so the boundary between them is hard to detect. Since the Sobel Filter and the Thinning Filter operates with thresholds, the number of detected crystal boundaries will depend on the size of these thresholds. With a too large threshold too many crystal boundaries are not detected, and with a too low threshold too much noise and hence too many wrong crystal boundaries are found.

One of the more critical points of the procedure is the use of the Morphological Close Filter. If a crystal is very small and have distinct edges, the crystal will be "closed" when the filter is applied on a too large area, and when the Thinning Filter is applied afterwards, a crystal boundary will be placed in the middle of the crystal. On the other hand, if a crystal has a size of the same order as the thickness of the sample, it will not fill the total thickness of the sample. The edges of the crystal are then compound of part of several crystals and they will appear white — due to the interference of the light from the different crystals — and broad, sometimes of the same size as the crystal itself. When the Close Filter is applied on a too small area, the crystal will be interpreted as two or more separate crystals.

Many experiments have been carried out to determine the right composition of filters and filter parameters. None of them were perfect, but the filter parameters were adjusted to diminish the effect of the noise and hence minimize the number of wrong boundaries. This made the program less sensitive to boundaries between crystals with similar orientation.

### 4.4.2 Outline determination

Since it was not possible to construct a perfect procedure to detect the crystal boundaries some adjustments of the outlines found by the automatic proce-

dure had to be made manually. The adjustments were made with the crystal outlines placed on each of the four original pictures.

Most of the adjustments were addition of crystal boundaries that were not found by the automatic procedure due to a too small intensity differ- ence between adjacent crystals. Other adjustments were addition of crystal boundaries where the procedure had placed an outline through a small cry- stal, and removal of wrong crystal boundaries, i.e. outlines that were dividing one crystal into 2 or more.

Crystals cut by the edges of the sample were removed from the outline to make sure only whole crystals contributed to the area distribution. To obtain the area measurements in mm$^2$, a calibration between pixels and mm was made. The length of each sample was measured after the pictures for the outline procedure was taken, and a function in Image-Pro made the calibration on the pictures.

## 4.5   Fabric measurements

The measurements of the ice fabric took place in January 2001 at The Alfred Wegener Institute for Polar and Marine Research in Bremerhaven, Germany, using an Automatic Ice Fabric Analyzer (AIFA).

### 4.5.1   The Automatic Ice Fabric Analyzer

The AIFA is based on the principles behind the Rigsby stage, i.e. the sam- ple is placed between two crossed polarizers, and the intensity of the light transmitted through the ice crystals changes as the polarizers (or the sam- ple) are turned. When measuring c-axes with the Rigsby stage one crystal is observed at a time. In the AIFA all crystals are "observed" at the same time by a CCD camera, and the actual extinction angle is not measured, but interpolated between values of extinction angles from 9 different camera positions. In this way it is ensured that the light is transmitted through the crystals from different angles like in the Rigsby stage.

The instrument consists of three sections, a measurement section, a con- trol-box/interface and a PC. The measurement section consist of four parts, a sample stage with a step motor, two crossed linear polarizers with a step motor, a CCD camera mounted on a step motor-controlled rotation and slide stage and a homogeneous scattered white light source. A sketch and a picture of the instrument can be seen in figure 4.4.

To conduct the measurements, a procedure which applies Image-Pro is used. The procedure is constructed so it is possible to measure textural
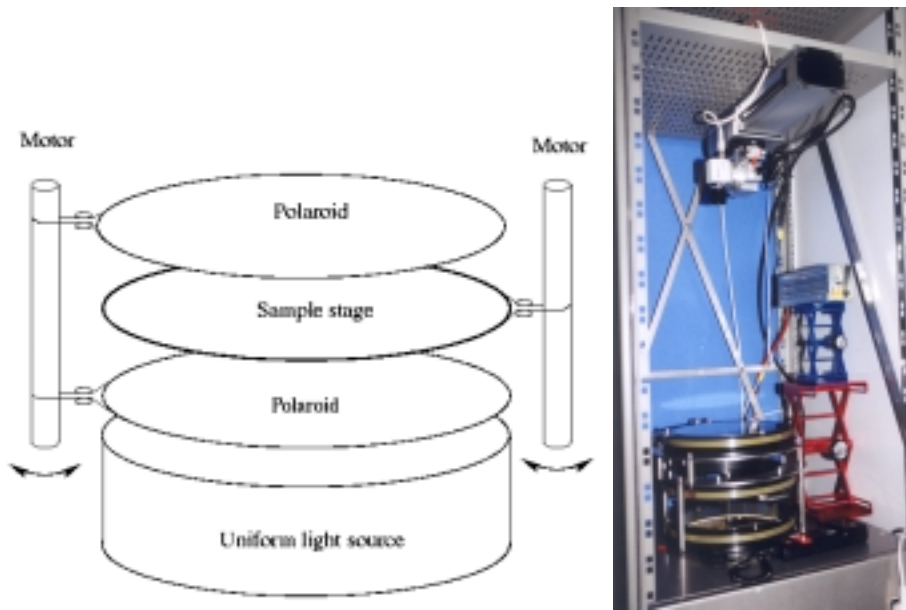
Figure 4.4: Left: A sketch of the measurement section of the Automatic Ice Fabric Analyzer. Right: A picture of the instrument inside the cabinet.

parameters as well as ice fabrics [Wang and Azuma, 1999]. Since the image resolution of the AIFA is lower than the Copenhagen CCD camera, I measured only the c-axis orientations with the AIFA.

The procedure runs in 9 steps, as shown in the flow diagram in figure 4.5. The details of the individual steps can be found in Wang and Azuma (1999):

1. A coordinate transform is made, to ensure measurements of the same crystal from the different camera positions.

2. The crossed polarizers are rotated 90°, and for every 5° a pictures is taken with the camera in vertical position. From these pictures the crystals for the fabric measurement are chosen by placing a measurement point in the crystal. Using several pictures makes it easier to distinguish between adjacent crystals with almost the same orientation. This is also the step where the crystal outline can be determined.

3. With the camera still in the vertical position, the crossed polarizers are rotated $\theta = 90°$, and for every 2° a picture is taken. The grey-scale values in 3x3 pixels around each measurement point is measured in each

```
                        ┌─────────────────────────────┐
                        │  Coordinate transformation  │
                        └─────────────────────────────┘
                                      │
                                      ▼
                   ┌──────────────────────────────────────┐
                   │      Chosing measurement points        │
                   │ (and determination of crystal outlines).│
                   └──────────────────────────────────────┘
                                      │
                                      ▼
              ┌──────────────────────────────────────────────┐
              │  90 degrees rotation of the crossed polaroids, │
              │          taking pictures for every 2 degree.    │
              │ Calculating intensity curve for each measurement point │
              └──────────────────────────────────────────────┘
                                      │
                                      ▼
                        ┌─────────────────────────────┐
                        │ 20 degrees inclination of the camera. │
                        └─────────────────────────────┘
   ┌─────────────────────────────────┐         │
   │ 45 degrees rotation of sample stage. │────────▶│
   └─────────────────────────────────┘         │
            ▲                                   ▼
            │              ┌──────────────────────────────────────────────┐
            │              │  90 degrees rotation of the crossed polaroids, │
            │              │          taking pictures for every 2 degree.    │
            └──────────────│ Calculating intensity curve for each measurement point │
                           └──────────────────────────────────────────────┘
                                      │
                                      ▼
                   ┌──────────────────────────────────────────┐
                   │ Calculation of c−axis orientation of measured crystals │
                   │         from the nine camera positions.    │
                   └──────────────────────────────────────────────┘
```
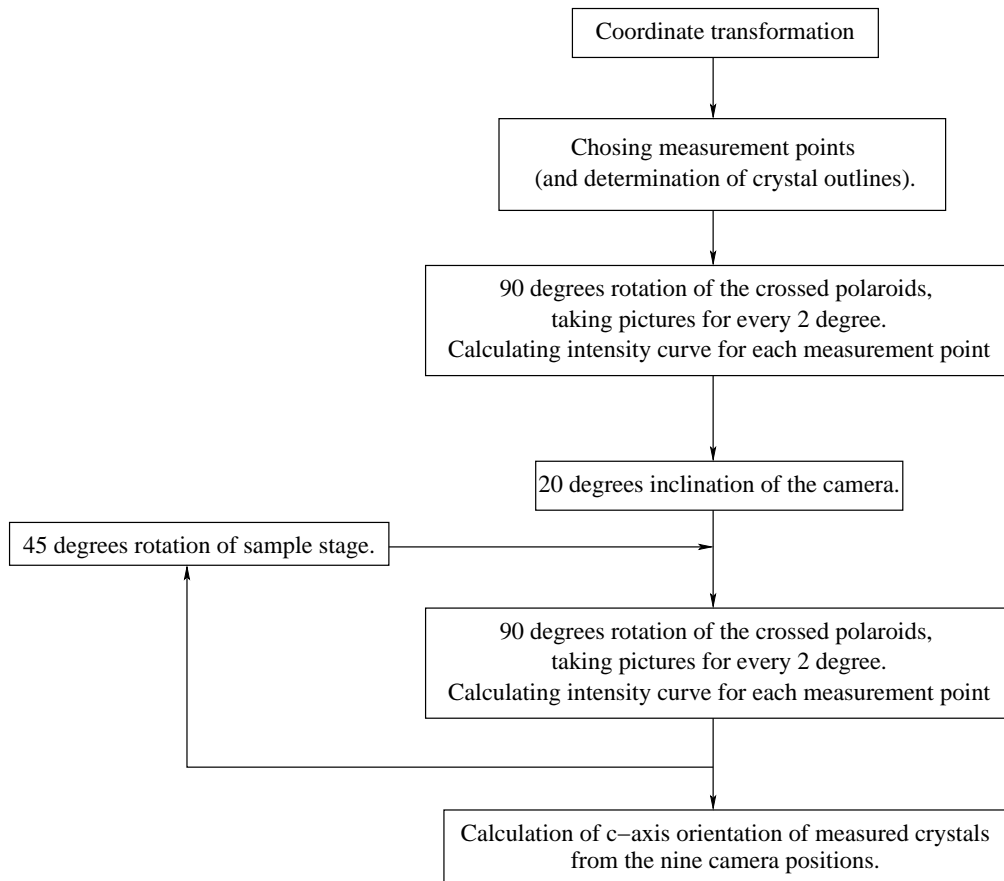
Figure 4.5: Flow diagram of the ice fabric procedure.

picture and the mean value is ascribed to the measurement point. The result is an intensity curve for each measurement point as a function of the angle $\theta$.

4. The CCD camera is moved to the end of the slide and inclined $20°$.

5. The coordinate transformation is applied and the positions of the measurement points in the new camera position are calculated.

6. Step 3 is repeated for this camera position.

7. The sample stage is rotated $45°$ and step 5 and 6 are repeated. The $45°$ rotation of the sample stage is repeated 8 times.

8. The intensity curve for each measurement point is approximated by a sine curve with a least-squares error algorithm. From this expression, the extinction angle is found for each of the nine camera positions by solving for the minimum over the range of $\theta$ from 0° to 90°.

9. From the extinction angles for the nine camera positions, the tilt and the azimuth angles for each measurement point are calculated.

## 4.5.2 The measurements

The AIFA is placed in a cabinet in a cold room with a temperature of -25°C. The motor control units were unfortunately very sensitive to low temperatures and would only work properly at a temperature above about -10°C. Therefore a heater was placed inside the cabinet to raise the temperature of the motor sections to about -5°C.

The sample was placed in the sample stage and the first step of the procedure was runned. Due to the rotation of the sample in the measuring steps, all crystals in the sample could not be measured. An Area Of Interest (AOI) of about 5x5 cm covering about 50% of the sample was applied to the images from which the measurement points were chosen.

Three different types of measurements were conducted:

1. In 12 samples (two per bag) about 200 crystals randomly distributed inside the AOI were measured.

2. In 4 samples 200 crystals were measured with two measurement points in each crystal as a mean of verifying the measurements.

3. 12 samples (two per bag) were measured in detail, where as many crystals as possible were chosen with two measurement points in each crystal. 500-600 crystals were typically measured.

Measuring one samples took about 1–2 hours. The most time consuming part was choosing the measurement points. The instrument operation time was almost constant no matter how many measurement points chosen. Due to the high temperature in the cabinet, the samples were exposed to sublimation at a high rate during the measurements.

Another problem arose as a consequence of the high temperature inside the cabinet. Since the cabinet with the instrument was placed in a cold room at a temperature of -25°C the samples were exposed to a large temperature difference when they were taken out of the instrument. This temperature difference lead to very severe cracks in some of the samples. This problem was solved by leaving the door to the cabinet ajar.

## 4.6    Conventional area measurement methods

To evaluate the results of the individual crystal method, a comparison be-
tween the method and two of the conventional crystal area methods: The
linear intercept and the mean area method, was made. The measurements
were carried out with the thin sections mounted in the Rigsby stage and
following the descriptions outlined on page 22 in section 3.2.1.

The mean horizontal and mean vertical crystal diameter was measured by
the linear intercept method on 6 of the vertical samples. On the 6 horizontal
samples, the crystal diameter was measured in four directions, each rotated
45° to the others.

The mean crystal area was measured by the mean area method on the
same 6 vertical thin sections where linear intercept measurements were mea-
sured.

# Chapter 5

# Results

In this chapter, I will present the results of my measurements. First I will show the intensity analysis of the thick sections, and shortly describe the features of the thin sections. Then I will present the results of the textural analysis, and make an estimate of the uncertainties of the crystal outline determination. The results of the c-axis measurements are presented hereafter. The orientation of some of the measured c-axes have showed up to be wrong. I will describe how the measurements are sorted and the errors discarded. Finally the results of the conventional mean area methods are presented.

## 5.1   Visual stratigraphy

Two typical thick sections are shown in the upper part of figure 5.1, one stadial (left) and one interstadial (right). A clearly layered structure, with white cloudy bands interchanging with clear ice (appearing black due to the background) can be seen in the stadial sample, while the interstadial sample only weakly displays a layered structure. This is a common feature of ice cores; more cloudy bands are observed in ice from cold periods, indicating a correlation with climate [Thorsteinsson, 1996]. The thickness of the cloudy bands varies from few millimeters to several centimeters, but are in general about 1 cm.

Layers in the stadial sample appear cloudy due to a high content of inclusions which scatters light. The reason for the inclusions are not well determined. A common believe is that they consist of microbubbles, which form around microparticles after core retrieval, and that the bands generally correlates well with high dust concentration [Thorsteinsson, 1996, Alley et al., 1997]. Cloudy bands are also observed in the interstadial samples, but they are not as abundant and not as strong in intensity as the cloudy bands in the sta-
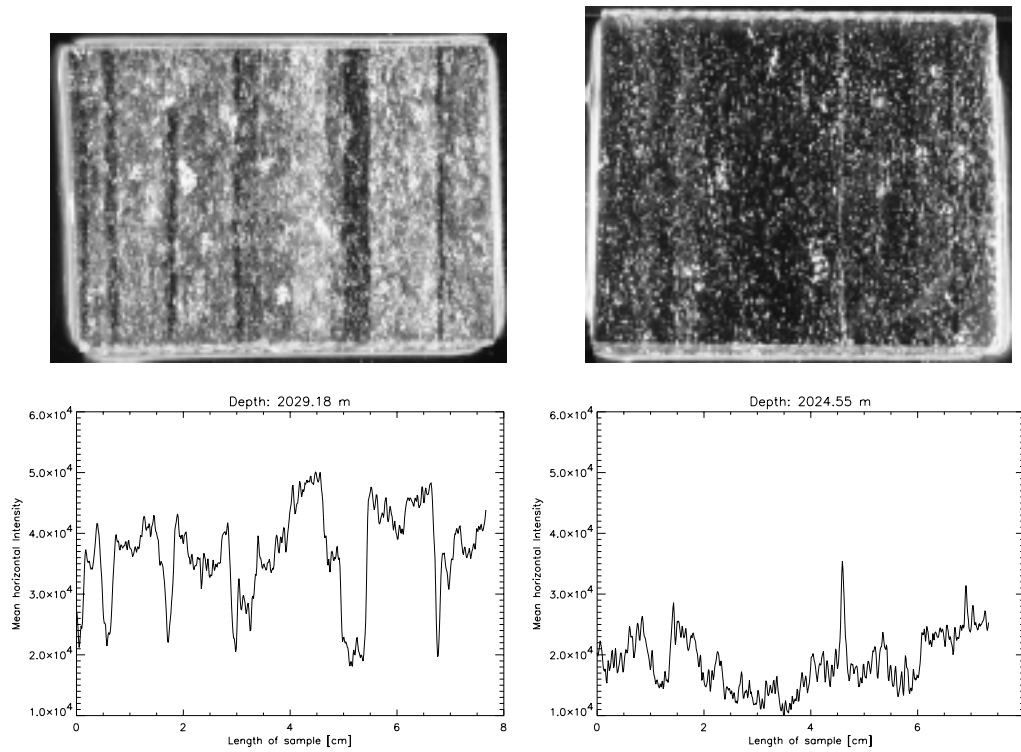
Figure 5.1: Top: A photo of two thick sections, a stadial sample from 2029.18 m depth (left) and an interstadial from 2024.55 m depth (right). Bottom: The mean horizontal intensity for the samples.

dial samples. Thick sections from a whole stadial, and an interstadial bag is shown in appendix A.

The mean horizontal intensity as a function of depth was measured from the photos using an intensity analysis function in Image-Pro. The pictures were converted to 16 bit gray scale images, and the intensity of each pixel was calculated as: $Intensity = 0.3 \cdot Red + 0.59 \cdot Green + 0.11 \cdot Blue$ [Image-Pro, 1999]. The resulting images have an intensity range of 0–65,535. The intensity analysis function measures the intensity in each pixel in a line placed in the desired direction, or the mean intensity in a band of parallel lines [Image-Pro, 1999]. A band of lines is placed parallel to the core direction, so they cover the horizontal extend of the sample, and the mean intensity in each horizontal layer of the band is measured. The intensity curves for the stadial and the interstadial samples can be seen in the bottom of figure 5.1.

The lowest intensity values lies around 10000 and the highest around 60000. The clear ice has a mean intensity of 15–20000, while the cloudy bands have intensity values of about 40–50000.

Some crystals in the surface of the samples in figure 5.1 are oriented so they reflect the light, which effects the mean intensity in the horizontal bands. The set-up for the photo session of the thick sections was quite intermistic. Some of the samples got a little inclined, so the upper side on the photos is shorter than the lower side, which can be seen on the sample in the right part of figure 5.1. Therefore the samples could not be measured from edge to edge, but a couple of millimeters in each edge was cut off. There is therefore a little offset in the intensity measurements of each sample on the order of 0.5 cm.

## 5.2   Thin sections

The thin sections were generally of very good quality with only few cracks. The durability of the sections was also very good. Several times they have been taken out of the plastic bags for photo sessions, and they have endured two trips between Copenhagen and Bremerhaven, although the journeys has resulted in some cracks. Due to the stays in the open air in the cold room, the samples have sublimated, especially at the edges which can be seen e.g. at the lower edge on the sample in figure 5.2. The crystals are generally elongated horizontally, and bands of crystals with smaller area than in general, such as the (weakly detectable) band in the middle of the sample in figure 5.2, can be seen. Pictures of thin sections from a stadial and an interstadial bag can be seen in appendix A.

About half of the thin sections had a little offset in thickness across the section. This occurred due to the mounting system of the microtome bench where one had to use great care that the glass plate with the sample was evenly mounted. The offset in thickness did not have any influence on the texture and fabric measurements, but gives a good illustration of how the dominant colour depends on the thickness of the sample. In figure 5.2 one can see the different first order interference colours of the ice crystals, from the thinnest lower right corner ($\sim$0.4 mm) to the thickest upper left corner ($\sim$0.6 mm). The dominant colour changes from grey to brown, yellow, orange, red, purple, blue and green.

**Figure 5.2:** The sample from 2015.75 m depth. The change in dominant colour due to changes in thickness can be seen across the sample.

## 5.3   Textural parameters

The result of the new implemented semi-automatic method to determine crystal boundaries is in general very satisfying. The crystal boundaries are determined very well, although a significant amount of crystal outlines still have to be corrected manually. From the point of view of implementing a new method, the samples were not well chosen, since they contained the smallest crystals in the lower part of the GRIP ice core, which have given several problems, as mentioned in section 4.4.1. On the other hand, it showed the power of the semi-automatic method, that it so well can determine very small crystals. Each sample contained about 1500 crystals, giving a total of 61250 crystals in the 41 measured samples.

It should be noted that the combination of filter parameters is optimized to detect the boundaries in my samples. This combination does not give the best results for samples with other crystal composition. Therefore the work with automatic crystal outline determination still has to progress, before it becomes a standard procedure.

## 5.3.1 Estimation of uncertainties

There are two contributions to the uncertainty of the measured textural parameters. The first is from the image analysis software and the second is induced when the crystal outline is adjusted manually.

### Pixels in the boundaries

After the crystal outline adjustment had been made, it was discovered that Image-Pro excluded pixels in the boundaries when the area of a crystal was calculated. This is apparently inevitable, and one has to take it into account when measuring the textural parameters. The size of this induced uncertainty depends on how large the crystals are. In my samples there is an average of 1500 crystals in each sample. With the standard boundaries, one pixel wide, the sum of the pixels in the boundaries constitute $4 - 5\%$ of the area of the samples, giving an error on the mean area of this order.

With one pixel wide boundaries, the Count Procedure in Image-Pro could not detect a conciderable part of the boundaries. Therefore the Dilation Filter was applied in the crystal outline procedure, and the crystal boundaries were made 2 pixels wide. This doubled the error induced by the exclusion of pixels in the boundary to about $10\%$.

The effect of the excluded boundary pixels on the individual crystal size depends on the size and shape of the crystal, yielding larger effect on small crystals than on large. Assuming circular crystals with a measured area: $A = \pi R^2$, where $R$ is the radius of the crystal. The actual area, including the boundaries is:

$$A' = \pi(R + r)^2 = A + \pi(r^2 + 2Rr) = A + \pi r^2 + 2r\sqrt{\pi A}, \qquad (5.1)$$

where $r = 1$ pixel $\approx 1/17$ mm with the present resolution of the images. Calculating the effect of this difference yields an error of up to $40\%$ for the smallest crystals with a measured area of 0.1 mm$^2$, and less than $3\%$ for the largest crystals with a measured area of 45 mm$^2$.

I have corrected the individual crystal areas according to equation (5.1). Although the crystals are not circular, the error made by this assumption is estimated to be less than a few percent. Both the mean crystal areas and the area distributions have been calculated with the corrected areas.

The effect of the excluded boundary pixels on both the flattening and the mean elongation direction has also been calculated, and it is found to be negligible.

**Outline procedure**

In the manual adjustment process, an additional 10–15% crystal boundaries
were added, since boundaries between crystals with almost the same orienta-
tion are not detected by the automatic outline procedure. Some of these ad-
ditional outlines were placed on boundaries that were only weakly detectable
in one of the four pictures. These boundaries could represent low-angle sub-
grain boundaries, and it can be discussed whether these low-angle boundaries
should be included as crystal boundaries. If they are accepted, it corresponds
to setting the limit for when sub-grain boundaries become real boundaries
to a smaller value than the commonly used 10–15°.

To test whether weakly detectable boundaries are sub-grain boundaries
or real boundaries, the c-axes of the crystals on each side of the boundaries
and the angle between them should be evaluated. This was not possible since
AIFA was not at hand, and it was very difficult using the Rigsby stage, since
the uncertainty on the stage is quite large and the crystals very small. There-
fore I chose to estimate the effect of too many detected low-angle boundaries
by another method. The sample from 2015.75 m depth was readjusted, with
a somewhat more conservative attitude to place crystal outlines on weakly de-
tectable boundaries. In the original adjustment, the result was 1746 crystals
on an area of 4679 mm$^2$. In the second adjustment, 75 fewer crystals were
found on the same area. The sample was then examined between crossed
polarizers, and the outline was found to fit quite well to the observed cry-
stal boundaries. 45 crystal outlines found in the first but not in the second
adjustment were examined in detail. Of the inspected boundaries, 16 were
estimated to be real boundaries, 20 boundaries were unclear and could there-
fore be low-angle sub-grain boundaries and 9 outlines were not found at all.

Taking the unclear boundaries as sub-grain boundaries, about two third
of the re-examined boundaries should not be taken into account. A better
estimate of the number of crystals in the sample is then about 1700 cry-
stals, leading to a mean crystal area 0.07 mm$^2$ larger than the crystal area
calculated from the first adjustment, or within 3% of the first estimate.

The overall inspection of the examined sample showed that the crystal
outline that was not adjusted manually fitted very well. There are most
likely both some boundaries that should not be there and some boundaries
that are missing, but my impression is that these two categories just about
cancels. So an estimation of the uncertainty on the number of crystals in a
sample is 5% or less, with a tendency of too many crystals found rather than
too few.

### 5.3.2 Crystal area

Most crystals have areas smaller than 10 mm$^2$, and only very few crystals are considerably larger than the others. The smallest measured crystal is 0.17 mm$^2$ and the largest is 51.35 mm$^2$.

The mean crystal area is found for each sample by taking the mean of the individual crystal areas. The result is plotted in figure 5.3 as a function of depth. In some of the samples from around 2024 m depth — on the peak of
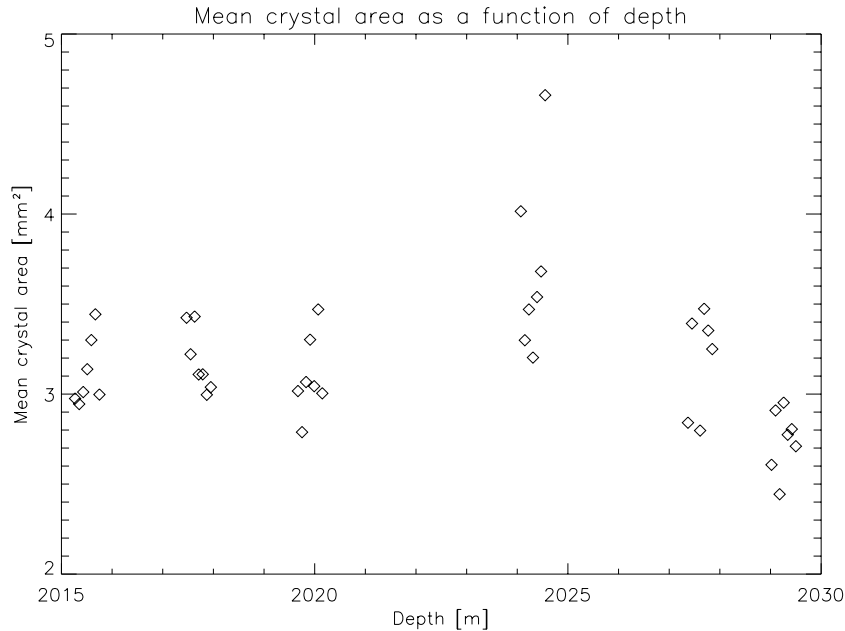


Figure 5.3: The mean crystal area as a function of depth.

the Dansgaard-Oeschger event — there are significantly larger crystals than in the other samples, while the other samples from the interstadial around 2020 m depth, do not have larger mean crystal areas than the samples in the stadials. The samples from 2024 m depth shows a much larger variability than do the samples from the other depth intervals. This could indicate that there is a change in the dominating physical process determining the crystal area at this depth. The mean crystal areas in the samples from 2029 m depth are slightly smaller than the mean crystal areas in the other stadial samples.

The mean crystal area in the samples in the interstadial and the stadials is 3.36 mm$^2$ and 3.04 mm$^2$, respectively, yielding a difference of about 11%. The mean crystal area for each bag can be found in table 5.1 together with the mean $\delta^{18}$O value.

Thorsteinsson et al. (1997) measured a horizontal crystal diameter of about 2,0 mm at 1982 m depth on thin sections from the GRIP core by linear intercept measurements. With the reported ratio between horizontal and vertical diameters of 1.36 at this depth [Thorsteinsson, 1996], the vertical diameter is 1.5 mm. Assuming ellipse shaped crystals, the area is then: $A = d_H d_V \pi/4 = 2.4$ mm$^2$. At 2064 m depth, the results are: $d_H = 2.3, d_V = 1.8$, giving an area of: $A = 3.3$ mm$^2$. These two measurements are the measurements of Thorsteinsson et al. (1997) closest to my sample interval. Although linear intercept measurements can not be compared directly to the mean area measured by the individual crystal area method (see discussion in section 6.1.1), the results of the two measurements are of the same order, and can thus be said to agree quite well.

### 5.3.3   Area distribution

When the area of each individual crystal in the samples has been measured the area distribution can be found. The area distribution for all crystals in the samples is plotted with asterisks on semi-logarithmic scales in figure 5.4. The distribution shows a very distinct bell shaped form, indicating that the crystal area is log-normally distributed. To test this, a Gaussian weighted log-normal distribution is fitted to the crystal area distribution. The log-normal distribution is defined as:

$$\frac{dN}{d\ln A} = N_0 \exp\left(-\frac{1}{2}\left(\frac{\ln(A) - \ln(\mu)}{\ln(\sigma)}\right)^2\right), \qquad (5.2)$$

where $A$ is the area, $\mu$ is the log-normal mode, $\sigma$ is the log-normal standard deviation and $N_0$ is the amplitude of the distribution [Underwood, 1970]. The log-normal standard deviation describes how the crystals are distributed around the log-normal mode. 68% of the crystals can be found in the interval: $[\exp(\ln\mu - \ln\sigma), \exp(\ln\mu + \ln\sigma)]$. Plotting the area distribution on linear scales will show a skew distribution.

The log-normal type distribution appears to be a very stable feature for the crystal area at this depth. All samples show this type of distribution individually (although very noisy), indicating that the dominant physical process determining the crystal structure is not changing across the climate event. A time invariant shape of the area distribution is a characteristic of the normal grain growth regime in metallurgy [Atkinson, 1988]. Also shown in figure 5.4 are the area distributions for crystals in the interstadial and in the stadials.

The observed crystal area distribution is the result of the interaction between ice flow, recrystallization and deformation processes that has taken
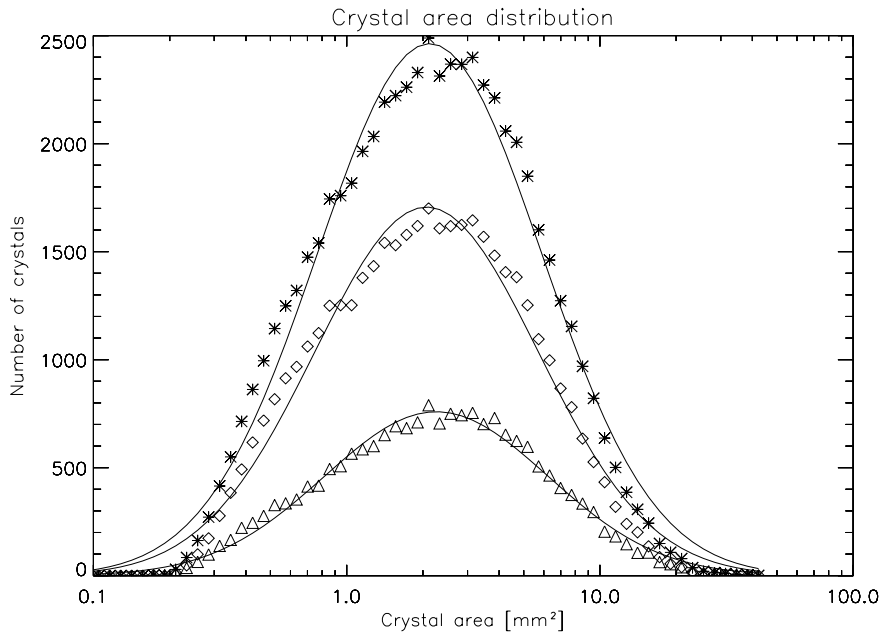
Figure 5.4: The area distribution for crystals in all samples (asterisks), for the crystals in the stadials (diamonds) and for the crystals in the interstadial (triangles) and their fitted curves. The log-normal modes, $\mu$, and the log-normal standard deviations, $\sigma$, for the fitted curves is found in table 5.1.

place in the ice since precipitation. Each contributing process has highly non-linear terms, such as the exponential term found in the Arrhenius equation, which enters both the normal grain growth equation and the flow law. The interaction of these terms, could be the reason for a log-normal area distribution.

It should be remembered that the found distribution is not the real crystal volume distribution, but only the distribution of the crystal areas in a cross-section of the ice. One could therefore imagine that the apparent log-normal distribution of the crystal area is an effect of the sectioning of the crystals.

The log-normal distribution is frequently found in small particle systems [Underwood, 1970]. It is often seen fitted to experimental data on grains in the normal grain growth regime in metallurgy, although not with an entirely satisfactory result [Atkinson, 1988]. It has also been observed in computer simulations of normal crystal growth in metals [Anderson et al., 1989]. Thorsteinsson et al. (1997) examined the normalized size distribution (the crystal diameter normalized by the average crystal diameter) of 3 samples from the upper part of the GRIP core, two from the normal grain growth

regime, and one from the polygonization regime (221.1, 633.6 and 1249 m). They found that all three samples approximately can be fitted with a log-normal distribution with peaks around 2/3 of the average crystal size. In the lowermost sample, there is a tendency of two populations, one below the average crystal diameter, containing the bulk of the particles, and one above.

The distribution for the crystals in each bag has also been plotted and the log-normal modes and standard deviations for the fitted log-normal distributions have been tabulated in table 5.1 together with the mean $\delta^{18}O$ value and the mean crystal area. The results confirms that there is a difference in

| Depth [m]/ Interval | Mean $\delta^{18}O$ [$^0/_{00}$] | Mean area [mm$^2$] | $\mu$ [mm$^2$] | $\sigma$ |
|---|---|---|---|---|
| 2015.20–2015.75 | -41.43 | 3.10 | 2.17 | 2.72 |
| 2017.40–2017.95 | -40.86 | 3.18 | 2.20 | 2.69 |
| 2019.60–2020.15 | -38.51 | 3.09 | 2.15 | 2.71 |
| 2024.00–2024.55 | -36.51 | 3.63 | 2.38 | 2.83 |
| 2027.30–2027.85 | -40.13 | 3.16 | 2.12 | 2.82 |
| 2029.95–2029.50 | -42.18 | 2.74 | 1.79 | 2.80 |
| Interstadial | -37.51 | 3.36 | 2.26 | 2.76 |
| Stadial | -41.15 | 3.04 | 2.07 | 2.77 |
| Total | -39.94 | 3.14 | 2.12 | 2.77 |

Table 5.1: Mean $\delta^{18}O$, mean area, and $\mu$ and $\sigma$ from the fitted log-normal distribution.

the crystal area between stadials and interstadial, or rather, that the crystals around 2024 m depth are larger than the crystals in other depth intervals. The crystals at 2029 m depth are smaller than the crystals in the other stadial depth intervals, also confirming the result from the mean crystal area. The standard deviation is almost constant and shows no significant changes with depth, supporting the observation of an invariant distribution with depth. It is seen from the table, that the log-normal mode is around 2/3 of the mean crystal area, as found by Thorsteinsson et al. (1997). They also found, that the maximum crystal diameter appears to be close to 3 times the average diameter. From the distributions in figure 5.4 it does not quite appears to be valid for this depth interval.

The fitted log-normal distribution appear to have a little offset for crystals smaller than the mean crystal area compared to the area distribution for the crystals in figure 5.4. To optimize the fit, I have tried to fit the log-normal distribution to the right shoulder of the area distribution for all crystals. The best fit was reached with a fit from 1.5 mm$^2$ to the maximum area, which

is plotted in figure 5.5 as a dotted curve. The log-normal mode is shifted to
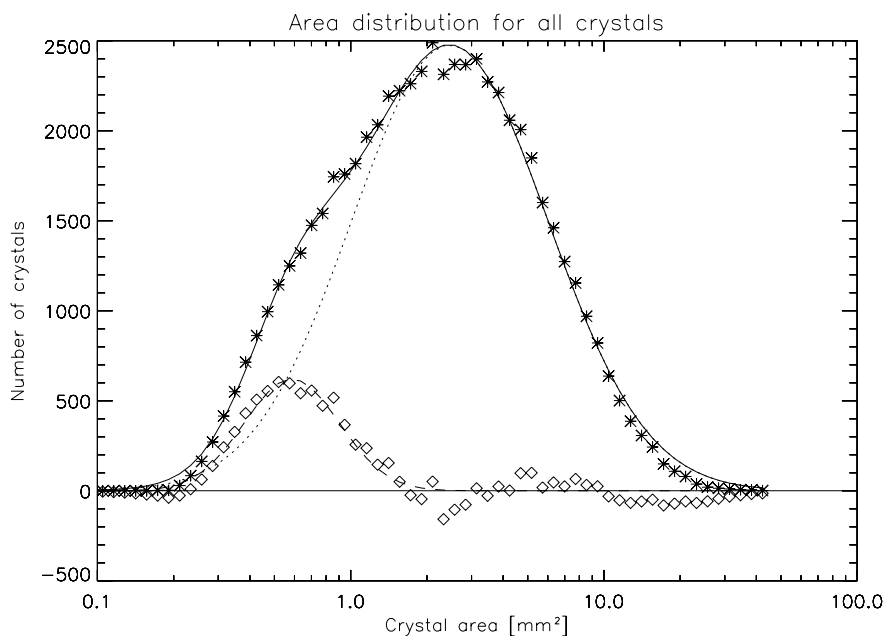


Figure 5.5: The area distribution for all crystals in the samples (asterisks) fitted with a log-normal distribution in the interval 1.5–45 mm² (dotted curve). The residuals between the fitted and the observed curves (diamonds), the fitted log-normal distribution to the residuals (dashed), and the sum of the two fitted log-normal distributions (solid).

2.46 mm$^2$ and the log-normal standard deviation is 2.44 which is considerable lower than for the total fit.

The residuals between the area distribution and the fitted curve are plotted as diamonds in the same plot. As can be seen, the residuals can be fitted to another log-normal distribution (dashed line) accounting for almost all the difference between the area distribution and the fitted log-normal distribution. The log-normal fit of the residuals have a log-normal mode of 0.59 mm$^2$ and a log-normal standard deviation of 1.54. The sum of the two log-normal fit (solid curve) is seen to fit the observed area distribution very well.

The crystal area distribution is thus composed of two log-normal distributions, one centered around 2.46 mm$^2$ containing about 90% of the crystals, and one centered around 0.59 mm$^2$ containing the rest. The reason for the overlaying of a small log-normal distribution to the large distribution could be either a physical process (e.g. polygonization) or a special feature of the samples (e.g. small crystals in the cloudy bands). It could also be a bias induced in the outline determination or an effect of the sectioning.

The effect of the exclusion of pixels in the boundaries on the individual crystal area is larger for small crystals than for large. One could therefore imagine, that the second log-normal distribution is an effect of the corrected crystal areas. To test this, I have plotted the distribution of the uncorrected crystal areas, and found that this distribution was almost identical to the distribution for the corrected crystal area. Therefore the second log-normal distribution does not arise from the correction of the crystal areas.

Although one could imagine that another effect of the crystal outline determination (e.g. the too many sub-grain boundaries accepted) could be the source of the extra small crystals, it is not likely that this could account for the whole deviation, since the accuracy of the outline determination is estimated to be within 5% and the second distribution contains 10% of the crystals.

Cloudy bands can be seen as bands of crystals with smaller areas than crystals in the rest of the sample (see section 6.5). To investigate whether the second log-normal distribution arise due to the small crystals in the cloudy bands, I chose seven samples with very distinct bands of small crystals. The area distribution of all crystals in these samples, for the crystals in the cloudy bands, and for the crystals outside the cloudy bands is plotted in figure 5.6. All area distributions could be fitted with log-normal distributions, although there is more scatter than for the total distribution.

The log-normal mode for the fit to the crystals outside the cloudy bands is about the double of the log-normal mode for the fitted distribution to the crystals in the cloudy band. But the value of 1.1 mm$^2$ is about two times larger than the log-normal mode of the second log-normal distribution from the fit of all crystals. Moreover, the deviation between the area distribution and the fitted log-normal distributions around 0.5 mm$^2$ can be discerned both inside and outside the cloudy bands. The cloudy bands are discussed further in section 6.5.

A physical process that could influence the area distribution is polygonization. I suggest that polygonization is the reason why the fitted log-normal distribution overshoots in the large tail. The polygonization subdivide large crystals so there is not as many large crystals as expected. But it is not very likely that the polygonization could create the bulge of very small crystals. An investigation of the angles between adjacent crystals indicates that polygonization is not a dominating process at this depth interval (see section 5.4.5).

A final suggestion of the reason for the second distribution in figure 5.5 is the sectioning effect. The crystals are polygons with somewhat rugged contours. Although it is purely speculative, one could argue that if the dominating crystal shape in 3D is a rugged structure with many small corners,
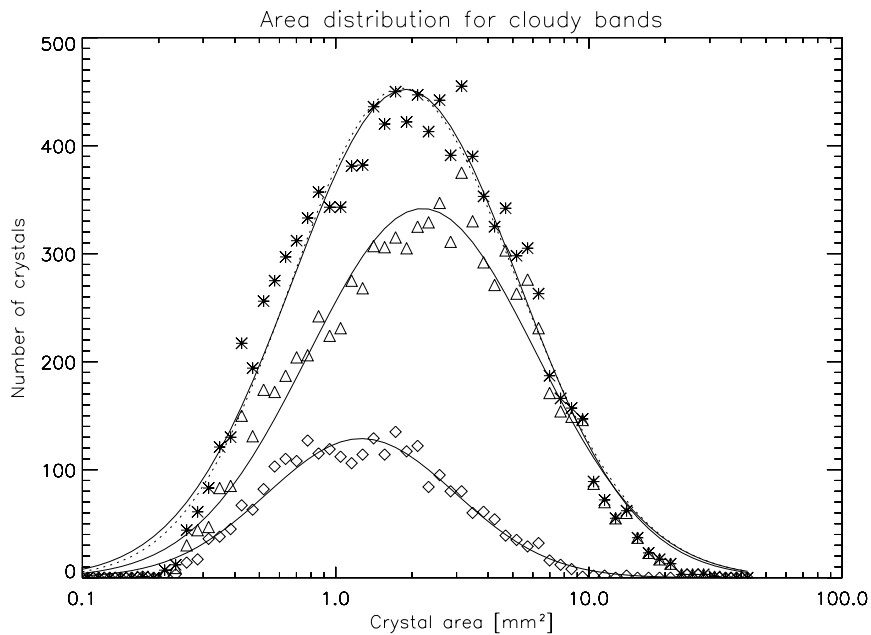
Figure 5.6: The area distribution for all crystals in the 7 samples (asterisks), for the crystals in the cloudy bands (diamonds), and for the crystals outside the cloudy bands (triangles) and their fitted log-normal distributions. $\mu$ is 1.71, 1.10 and 2.02 mm$^2$ and $\sigma$ is 3.06, 2.58 and 3.05 for the three distributions: All crystals in the 7 samples, crystals inside and crystals outside the cloudy bands respectively

many of these small corners are cut, which could give rise to the distribution of very small crystals, when the sample is sectioned.

## 5.3.4   Flattening and mean elongation direction

When the ice is subject to a uniaxial compression, the crystals become elongated horizontally due to the vertical stress. To describe the flattening of the crystals, I have chosen the ratio between the horizontal and the vertical dimensions of the crystal bounding box. This parameter lies generally between 0.5 and 2.5, with few values as low as 0.4 and as high as 4. The mean value of the ratio for each sample is plotted in figure 5.7 as a function of depth.

There is in general only low variability in the flattening with depth. The mean value of the flattening is about 1.33 for all the samples. There is no significant difference in the mean flattening between samples in the interstadial and in the stadials.

My results are in good agreement with the earlier findings for the GRIP ice core. Thorsteinsson (1996) calculated a mean ratio of vertical to horizon-
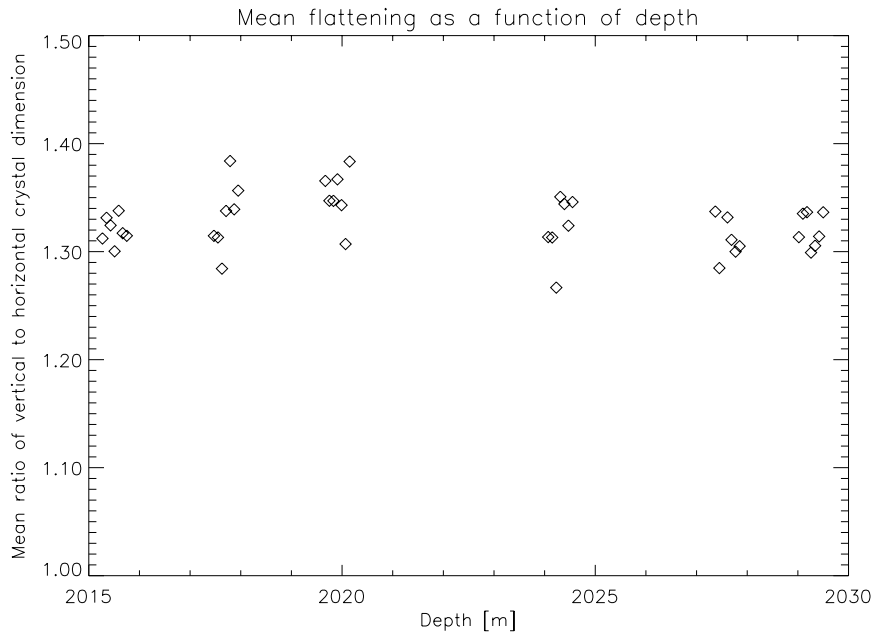
Figure 5.7: The mean flattening, expressed as the ratio between the horizontal and the vertical dimension of the crystal bounding box, as a function of depth.

tal diameter from linear intercept measurements in the two directions. His result was a ratio of 1.36 in the depth interval 1625–2790 m with only small variations with depth.

Since the vertical stress increases with depth, an increase in the flattening of the crystals would be expected. This increase is however counteracted, both by polygonization, that will breaks elongated crystals into shorter crystals, and by normal grain growth, that tends to round the crystals, since they grow with the same speed in both horizontal and vertical directions.

The elongation direction of a crystal is defined as the angle between the horizontal plane and the major axis of an equivalent area ellipse for the crystal. This parameter is also related to the stress in the ice. When the ice is subject to uniaxial compression, the mean elongation direction is horizontal, and the angle of the mean elongation is $0°$. The crystal elongation direction is normally distributed around $0°$.

The mean elongation direction for each sample as a function of depth is plotted in figure 5.8. For the samples in four of the six bags, the mean elongation direction is $0° \pm 2°$. The samples from two of the bags, one interstadial and one stadial, have a mean elongation direction of about $4° \pm 2°$. This indicates that the layered structure in these samples is not horizontal.
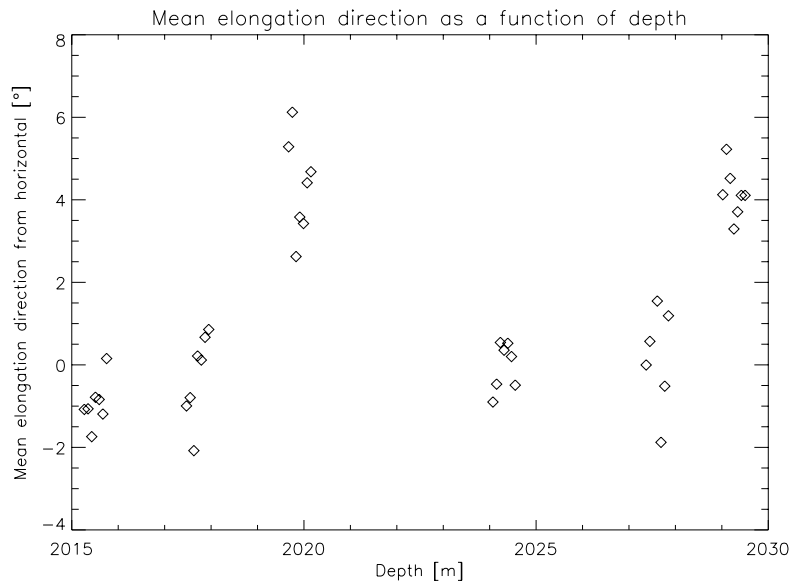
Figure 5.8: The mean elongation direction as a function of depth.

The inclination of the borehole does not exceed 3° throughout the core an is only 0.5° at 2000 m depth [Gundestrup et al., 1993], so 4° inclined layers could not be the result of a borehole inclination. An inspection of the pictures of the thick sections shows, that the layers are not horizontal in the samples from these two bags, and that the bottom of one of the bags was not flat. Therefore the samples from this bag may not have been cut horizontally, but with a little offset because of the uneven bottom of the bag. Due to the cutting procedure, all samples will be inclined if the first sample is inclined. Since slight waviness of layers with inclinations up to 6° are reported in the 2300–2790 m depth interval [Thorsteinsson, 1996], slightly inclined layers at 2000 m depth can not be outruled. An inspection of the fabric diagrams for the samples in the two bags show no deviation from the general pattern of the fabric diagrams in IS3, indicating that the layers in the samples are tilting, and they are not unevenly cut. The effect of the inclined layers on the texture and fabric measurements is zero or negligible.

The development of the crystal elongation direction with depth can also be shown by plotting the distribution, either in a circular plot [Azuma et al., 1999], or in a regular plot. The elongation direction is a good parameter to describe the development of texture with depth in a whole ice core, as done by [Azuma et al., 1999], but it is not so suitable for detail studies, since the information derived from it is limited.

### 5.3.5    Crystal morphology

To evaluate the average grain morphology, the mean form factor can be calculated [Gay and Weiss, 1999]. The mean form factor is given by $A/s^2$, where $A$ is the crystal area and $s$ is the crystal perimeter. It is a dimensionless quantity which has a maximum value for a sphere: $A/s^2 = \frac{\pi r^2}{(2\pi r)^2} = \frac{1}{4\pi} =$ 0.0796. Some processes, e.g. migration recrystallization, are believed to create interlocking crystals [Duval and Castelnau, 1995], which would result in a lower mean form factor than for regular crystals.

I have tried to calculate the mean form factor, but the perimeter measured by Image-Pro is too small. When the mean form factor is calculated, some crystals — especially small crystals — have mean form factor values larger than 0.08, which is impossible. Since Image-Pro is a commercial software package, the company does not provide information on how the measurement is made. In the end, measuring the perimeter of the crystals is a discreet problem of counting the number of pixels in the boundaries. Since the crystals are not rectangular but rather round or polygons, the length of the round edges has to be interpolated, and this interpolation is apparently not successful.

I have however calculated the mean form factor, but without trusting the magnitude of the result, and assuming that the wrong measurement of the perimeter influences all samples equally. With this assumption, I can compare the mean form factor for the samples, which is done in figure 5.9.

The mean form factor has very little variation with depth, and there is no significant difference between the samples inside and outside the interstadial. This indicates that the physical process determining the crystal shape does not change across the climate event.

## 5.4    Fabric

The measurements of the orientation of the crystal c-axes was generally very successful. The orientation of more than 10000 crystals was measured in 28 samples, most of them with two measurement points in each crystal. The instrument was very stable, and the time used to measure the crystals was much less than one would expect to use when measuring crystal orientations on a Rigsby stage. Although a considerable part of the measurements had to be discarded due to a too low image resolution (see below), the detailed measurements were comprehensive enough to give good statistics.

Figure 5.10 shows a typical fabric diagram of the measured samples. The plot is seen in the plane of the sample, with the core direction aligned ver-
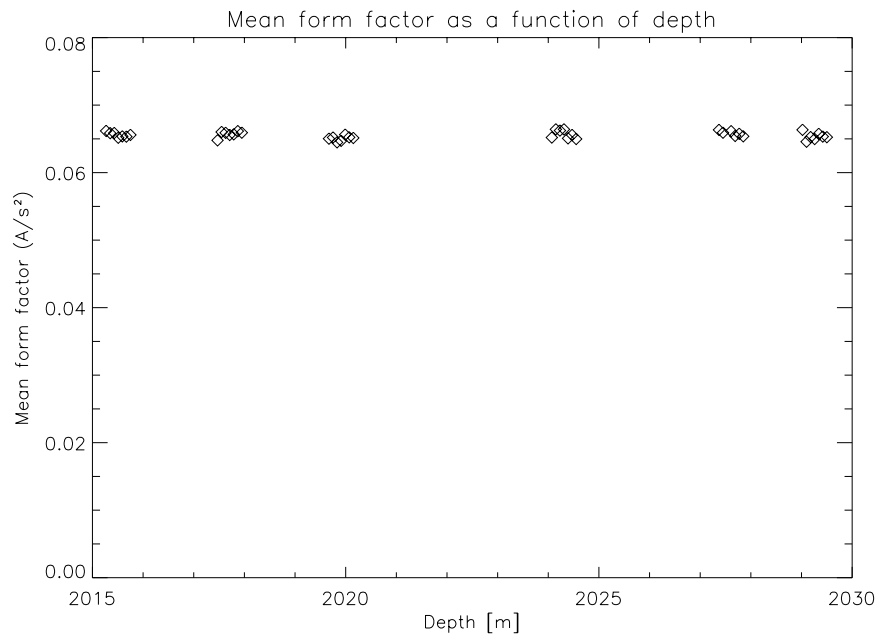
Figure 5.9: The mean form factor as function of depth.

tically in the plot. Most of the c-axes are lying in the plane of the sample clustered around the core direction.

The most common way to present a fabric diagram is with a top view plot in the plane perpendicular to the core direction. This presentation is obtained by turning the c-axes vectors before projecting them. The right hand side of figure 5.10 shows the top view fabric diagram for the same sample as in the right hand side of the figure. The diagram shows a strong single maximum, with individual crystals deviating from the general pattern.

## 5.4.1 Fabric measurement errors

Most of the crystal c-axis orientations are expected to lie within a cone with a half-apex angle of about 45° from vertical as observed by Thorsteinsson et al. (1997). I decided that if the crystal c-axes had an azimuth angle within 50° from the core direction (in the original coordinate system, in the plane of the sample) they were very likely to be correct and did not need further examination. A few crystals had c-axis orientations outside this interval, and some of them were almost perpendicular to the core direction. Measuring the orientation of crystals that are almost in the plane of the sample is difficult for AIFA, like it is difficult when one is measuring these crystals in
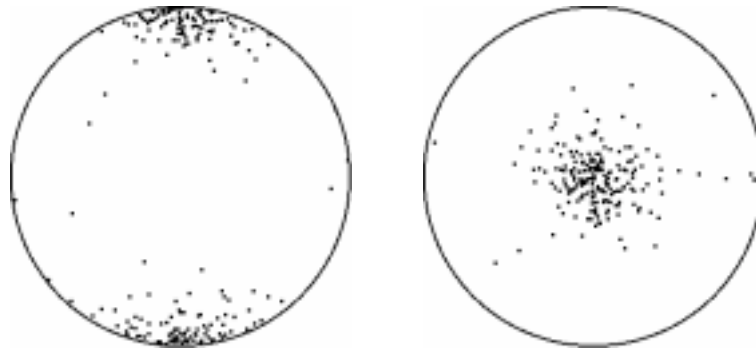
Figure 5.10: Left: A typical fabric diagram for the samples (the sample from 2015.59 m depth) seen in the plane of the sample. Right: The same sample where the c-axes are turned 90° so they are seen in the plane perpendicular to the core axis. The number of crystals in the fabric diagram is 205.

the Rigsby stage (see section 3.3.1). The measured c-axes 90° perpendicular to the core direction could therefore be wrong measurements. This problem was examined using a Rigsby stage.

Two samples were chosen for the inspection, one of the samples with about 200 measured crystals (group 1) and one of the samples measured in detail (group 3). I re-measured 8 deviating crystals in the group 1 sample from 2015.69 m depth using the Rigsby stage, and found that three crystals with low tilt angles (53°–78°) had the right orientation. The remaining 5 crystals all had a tilt angle of 89°. 4 of these had azimuth angles turned 90° in the original measurement compared to the control measurement. The azimuth angle of these wrongly measured crystals were between 67° and 90° from vertical. One crystal with a tilt angle of 89°, which had the correctly determined orientation, had an azimuth angle of 52° from vertical and was thus just outside the accepted interval.

The sample from 2015.75 m depth was measured on AIFA in detail twice, so most of the measured crystals have four measurement points, giving a good basis for comparison. The examination of this sample yielded 3 types of measurement errors in the samples measured with two measurement points in each crystal:

1. A 90° or 270° difference in the azimuth angle between the two measurements of the same crystal. Most of these errors occur when the tilt angle is larger than 85° and the azimuth angle of one of the measurements are within 10° from the core direction This is the type of error found by the examination of the sample from group 1. All these measurements were discarded.

2. A 180° difference in the azimuth angle. This error arise most often when the tilt angle is close to 90°, and is essentially the same problem as mentioned above. Here it turns out well, since the "wrong" measurement ends in the "right" direction, almost parallel to the other measurement. These measurements are accepted.

3. A difference larger than 5° between the two measurements in either the tilt or the azimuth angle. This "error" can arise if one of the measurement points is too close to the edge of the measured crystal, or if the measurement points are placed in two different crystals or on each side of a sub-grain boundary. Since it was not to possible to determine the cause of this "error", these measurements were discarded. 5° were chosen as the limit to be well outside the interval of the accuracy of the instrument ($< 2°$).

Most of the measurement errors arise because the measured crystal is too small and/or the measurement point is too close to the edge of the crystal (in which case the uncertainty of the coordinate transformation can move the point to an area with another intensity for one or more of the camera positions). After sorting the data of the two measurements of sample v3665.1 and the "trivial" errors as mentioned above were discarded, 6 suspicious crystals remained, all with azimuth angles close to 90° from the core direction and high tilt angles. These were re-measured using the Rigsby stage and except for one crystal — that was too small to be measured in the Rigsby stage — all were turned 90° in the first measurement compared to the control measurement.

## 5.4.2   Sorting the fabric measurements

The 16 samples with two measurement points in each crystal were sorted with the above mentioned criteria for measurement errors, discarding the "trivial" errors. Of the remaining crystals outside the "50° from vertical" interval, both in these 16 samples and in the 12 samples from group 1, I discarded the crystals with tilt angles larger than 85° if their azimuth angle was within 65°-90° from the core direction.

The amount of measurement errors in each sample is 0–2% for the samples in group 1, 2.1–5.4% for the samples in group 2 and 5.7–12.9% for the samples in group 3. The relatively large percentage of errors for the last group of measurements arise because I tried to measure all crystals in the sample, also the very small ones, and many of these measurements were unsuccessful. Very small crystals were avoided in the other two groups.

The sorting and discarting of crystals does not ensure that there are no more measurements errors, but the investigations show that the remaining crystal c-axes have very likely orientations. The measurement uncertainty after the sorting is estimated to be less than a few per cent.

In figure 5.11, two fabric diagrams, one from an interstadial and one from a stadial sample is shown. In general they look very much alike, both
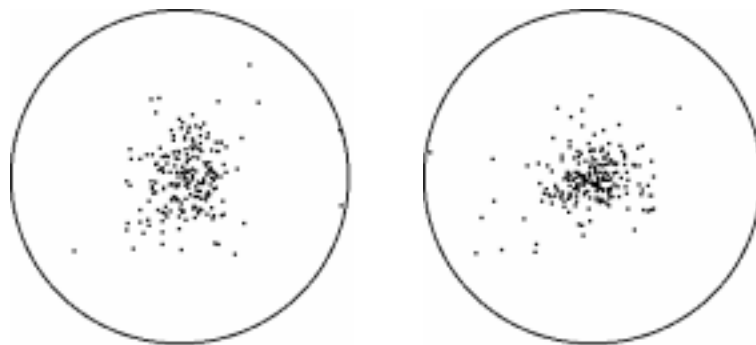


Figure 5.11:  Left:  A fabric diagram from an interstadial sample (from 2020.07 m depth). Right: A fabric diagram from a stadial sample (from 2027.77 m depth). In both samples 200 randomly chosen c-axes are shown.

displays a strong single fabric maximum, and no significant difference can be seen between them. This is a general feature of the fabric diagrams from the stadial and the interstadial samples. The fabric diagrams are also similar to fabric diagrams found by Thorsteinsson et al. (1997) around the same depth. In appendix A, fabric diagrams for samples in a stadial and an interstadial bag are shown.

## 5.4.3   Statistical parameters of the fabric measurements

To quantify the fabric measurements, the statistical parameters, $R$, $\alpha_s$ and the eigenvalues has been calculated from the equations in section 3.3.5.

Figure 5.12 shows $R$ for the measured samples as a function of depth. $R$ lies within 80–90% displaying a strong single maximum. There is a weak overall tendency of an increase in $R$ with depth, indicating a strengthening of the single maximum fabric. This is a general feature of the development of the fabric in the GRIP ice core [Thorsteinsson et al., 1997]. On the other hand, there is also a tendency of a weakening with depth in the uppermost three bags, and a strengthening with depth in the lowermost three bags. This indicates that there is a correlation of the fabric with climate, or that an underlying physical process could influence the strengthening of fabric.
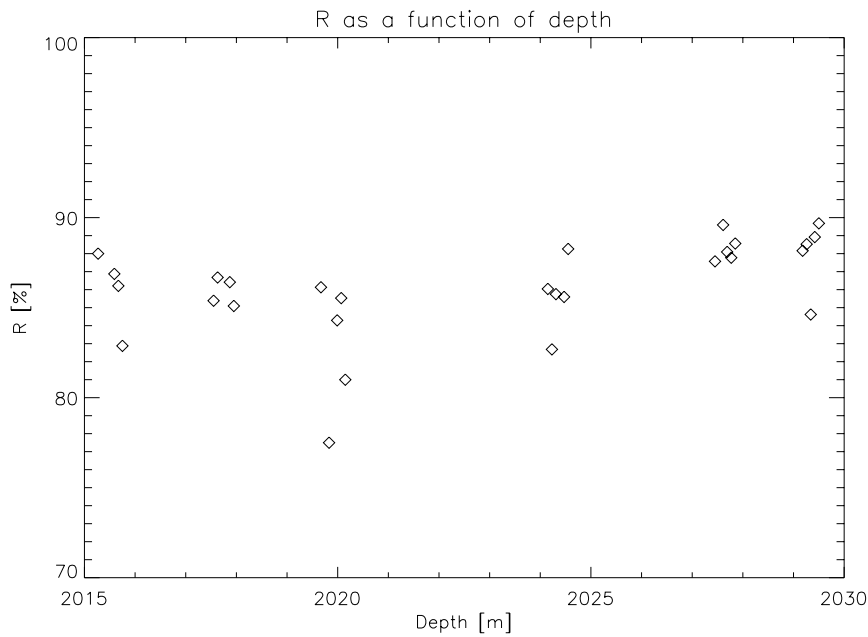
Figure 5.12: $R$ as a function of depth.

In figure 5.13 $\alpha_s$ and the eigenvalues are plotted as functions of depth. $\alpha_s$ lies around 20–25° and shows a decrease with depth, confirming the fabric strengthening found from the $R$-value. $\alpha_s$ is almost a mirror-image of the $R$-value.

The largest eigenvalue lies around 0.85–0.9, and the other two around 0.05–0.1, which is another confirmation of a strong single maximum fabric. There are only small variations in the eigenvalues with depth. There is a trend of a slight increase in the largest eigenvalue, and a slight decrease of the other two. Both the calculated values and the trends of $R$, $\alpha_s$ and the eigenvalues verifies the results of Thorsteinsson et al. (1997) within few per cent.

The $q$-parameter, as given in equation (3.3) on page 28 is calculated for each sample. $q$ lies in the interval 2.2–56.4 for the measured samples also confirming that the fabric is a single maximum.

Due to the low intersample variability, all the statistical parameters shows almost identical features. In the following treatment of the fabrics, I will only refer to one statistical parameter. I have chosen $R$ as the main statistical parameter, since no additional information is obtained from $\alpha_s$ and the eigenvalues.
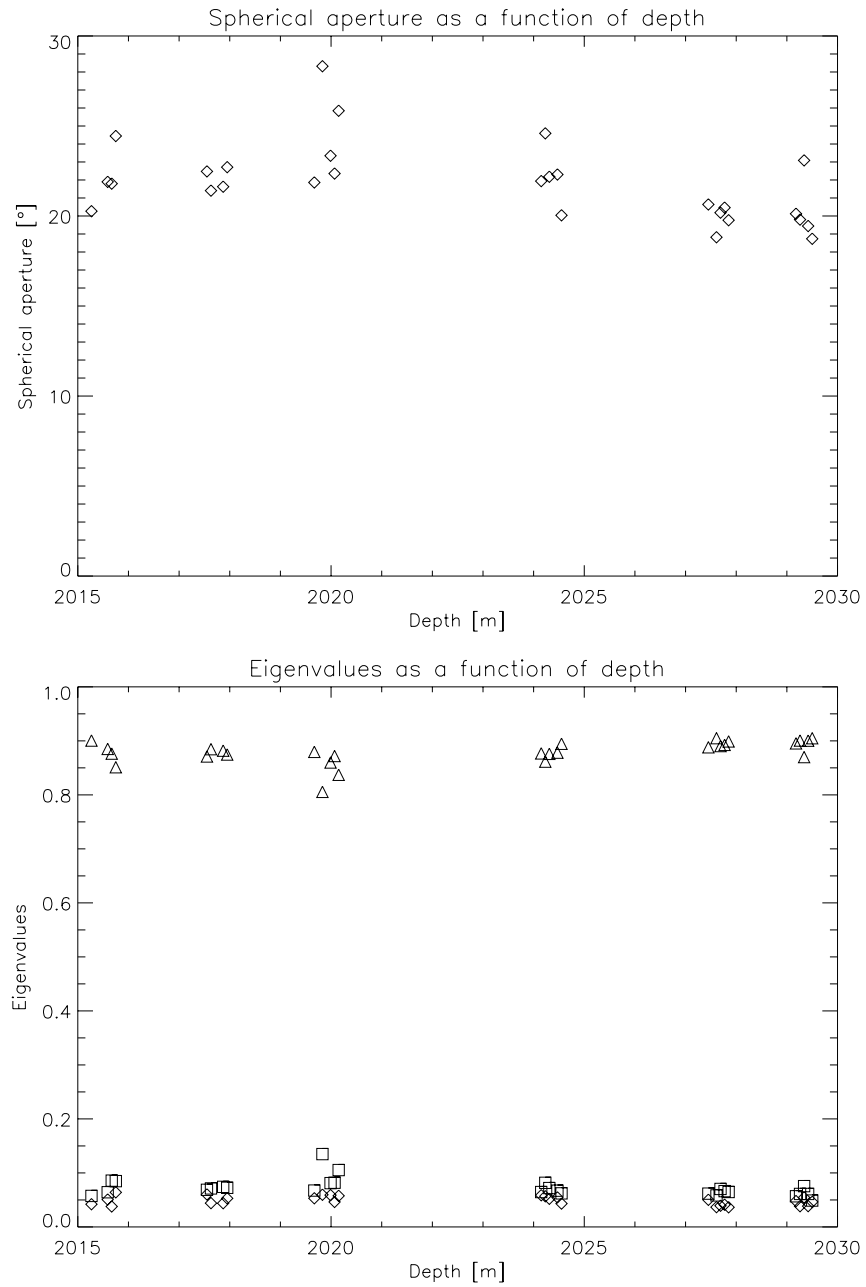
Figure 5.13: $\alpha_s$ (top) and the eigenvalues (bottom) as a function of depth. The eigenvalues are plotted in descending order (triangles, squares, diamonds).

### 5.4.4  Reproducibility of measurements

To obtain an expression for the accuracy of the AIFA, I have examined how well the instrument reproduces the results in five of the samples with two measurement points in each measured crystal, the four samples in group 2 and one sample from group 3. Crystals which had an overlap of one or more of the 9 measurement pixels from the two measurement points were not used. The result of this examination can be seen in table 5.2, yielding a reproducibility of the measurements for the 1213 examined crystals of 0.30° for the azimuth angle and 0.54° for the tilt angle. This lies within the accu-

| Depth [m] | Number of crystals | azimuth [°] | zenith [°] |
|---|---|---|---|
| 2015.27 | 419 | 0.27 | 0.54 |
| 2019.83 | 190 | 0.30 | 0.64 |
| 2024.15 | 217 | 0.28 | 0.40 |
| 2027.45 | 188 | 0.32 | 0.45 |
| 2029.34 | 199 | 0.39 | 0.65 |
| Total | 1213 | 0.30 | 0.54 |

Table 5.2: Sample depth, number of crystals examined, and mean deviation of azimuth and tilt angles from multiple measurements.

racy of the instrument of ±0.34° for the azimuth angle and < ±2° for the tilt angle and well within the reproducibility of < 1° as stated by Wang and Azuma (1999).

### 5.4.5  Angle between adjacent crystals

According to Alley et al. (1995b) the distribution of the angle between adjacent crystals can reveal information about the dominating recrystallization process. For the isotropic new fallen snow, the angle between two adjacent crystals should on average not be different than the angle between to randomly selected crystals in the sample. If polygonization is the dominating recrystallization process, many adjacent crystals have low angle boundaries, since they are the result of a division of one crystal. Therefore there will be a surplus of low angles between adjacent crystals. If migration recrystallization is the dominating recrystallization process, new crystals oriented with high angles to their neighbours nucleate and grow rapidly. This results in a surplus of high angles between adjacent crystals. A high content of impurities should reduce the crystal boundary migration by boundary pinning

and hence reduce the crystal growth. This will preserve the population of crystals, causing neighbour relations to be the same as in the upper layers.

Alley et al. (1995b) mapped 5 samples with about 100 crystals and around 200 neighbour pairs from between 200 and 870 m in the Byrd ice core, to test the reason for the stop in grain growth below 400 m. They found that the distribution of angles between adjacent pairs was evenly distributed in the uppermost samples. Further down, small angles became more abundant, indicating that polygonization is the dominant recrystallization process in the Byrd ice core which is stopping the increase in mean crystal size.

I have made a similar analysis on two samples, one interstadial and one stadial. I chose the interstadial sample with the highest $\delta^{18}O$ value and mean crystal area (4.27 mm$^2$). It is also one of the samples with the lowest amount of impurities. The stadial sample had one of the lowest $\delta^{18}O$ values and one of the highest amount of impurities and the lowest mean crystal area (2.16 mm$^2$). These two samples represents the end points of the mean crystal area interval. When these two samples are investigated, the area, $\delta^{18}O$ and the impurity intervals are spanned, which compensates for the poor statistics when examining only 2 out of 41 samples.

The crystals are mapped during the measurement process. Each pair of adjacent crystals is found and the angle between the c-axis orientation is calculated. 542 measured crystals gave 1021 neighbour crystal pairs in the stadial sample. In the interstadial sample, 331 crystals were measured, and 525 neighbour pairs were found.

Since the distribution of the angle between adjacent crystals depends on the overall fabric of the sample, the distribution has to be normalized. The normalization is made by comparing the angles between adjacent crystals and the angle between pairs of randomly chosen crystals in the sample. A random number generater [IDL, 1993] was used to select 10000 pairs of uniformly distributed crystals randomly from the sample and calculate the angle between them. Few pairs are sampled multiple times. The angles between the randomly chosen pairs are sorted by size and divided into ten bins, each containing 1000 angles. The bins will be equally large if the distribution is uniform ($R = 0\%$). Since the fabric is strongly confined in the depth interval of my samples, the bins with small angles are narrow, while the bins with large angles are wide.

The angles between adjacent crystals are then divided between the bins, and the weight of each bin (the number of pairs in the bin compared to the expected 10%) is calculated. In figure 5.14 the distribution of neighbouring angles for the stadial and the interstadial sample is shown.

The relatively flat distribution of the stadial sample shows that there is not a preferred orientation of the angle between adjacent crystals. This in-
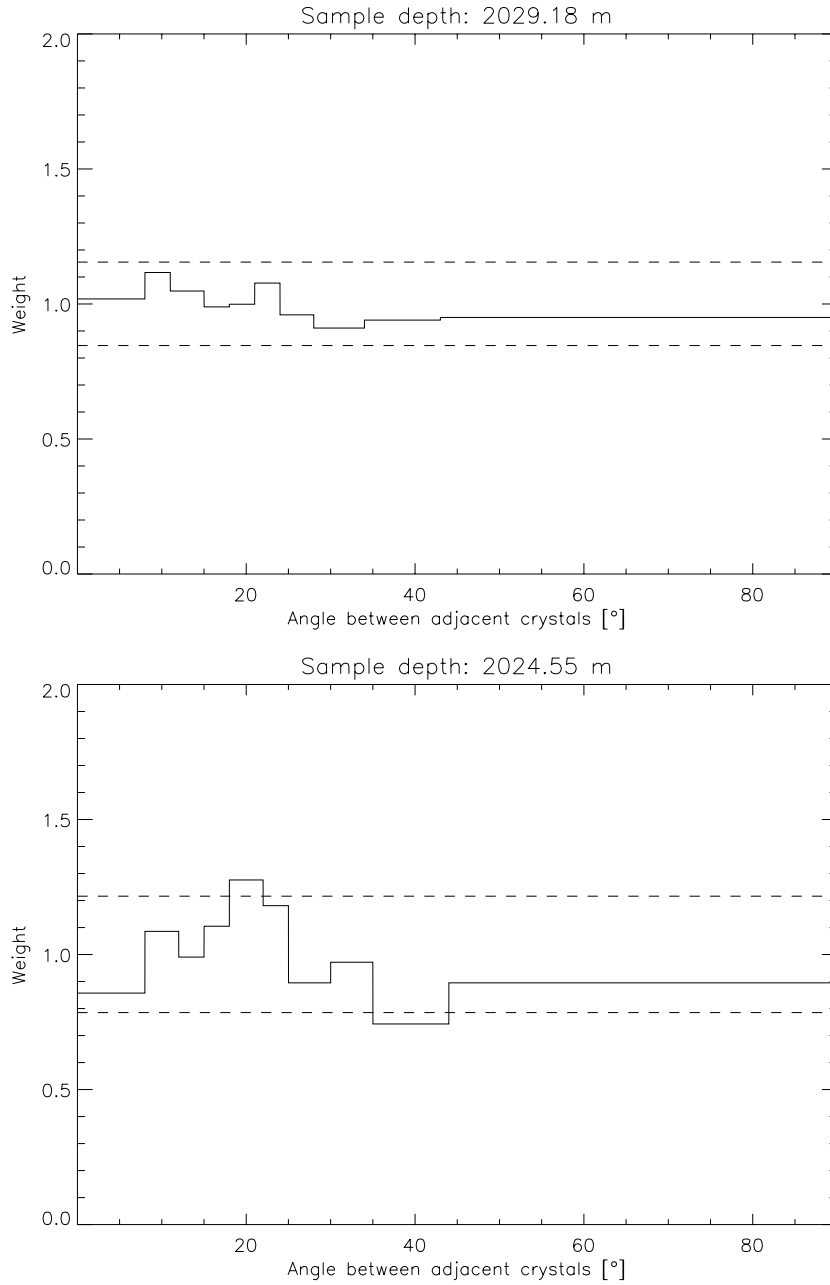
Figure 5.14: The angle between adjacent crystals for the stadial (upper) and the interstadial (lower) samples. The dashed lines mark the level of significant deviation from a random distribution at 95% confidence level in a binomial test. In the stadial sample, there are 542 crystals and 1021 pairs of neighbours, in the interstadial sample there is 331 crystals and 525 pairs of neighbours.

dicates that boundary pinning is the most dominant recrystallization effect. At this depth polygonization should take place, which is verified by the observation of strain shadows in the samples. But the amount of impurities is apparently so large that the effect of the inhibited crystal growth is larger than the effect of the polygonization.

The interstadial sample shows more variation in the angle distribution, because the number of adjacent crystal pairs is about half the number of the stadial sample. But it is evident, that neither polygonization nor migration recrystallization is the dominant recrystallization form in this sample either. This indicates that the dominating process of formation of texture both in the interstadial and in the stadials is the same, although the difference in mean crystal area is large between the two investigated samples (almost the double of the stadial sample in the interstadial sample). Also shown in the plots is the upper and lower limits for a deviation of the distribution from random at 95% confidence in a binomial test. The highest deviation for the stadial sample is significant at 89% in a binomial test. The deviation of the interstadial sample around 20° and 40° is difficult to interpretate. They are both significant at the 98% level. I have no knowledge of a process that theoretically would produce a deviation from normal with these angles. A further investigation of samples from the interstadial is needed to see if the deviations around this angle are a general feature.

I have also investigated whether the dominant recrystallization process in the cloudy bands and in the clear ice is different. I divided the crystals in the stadial sample into two groups from visual inspection. The two groups contained almost the same amount of crystals: 253 in the cloudy band and 289 outside the cloudy band. The random number generator was applied on each group separately. The angle betwen adjacent crystals of cloudy bands and clear ice can be seen in figure 5.15.

Although the result shows a little more variation than for the whole sample (due to the poorer statistics), there is no significant deviation from normal that can be explained by polygonization or migration recrystallization, either inside or outside the cloudy band. This indicates that boundary pinning is the dominating effect on recrystallization in both the cloudy bands and in the relatively clear ice in this depth interval. The deviation around 20° in the cloudy band is significant at the 99% level. Like for the deviations in the interstadial sample, I do not have any suggestions for the reason of this.

One can notice that the bins with high angles in the distribution of clear ice are much larger than the bins in the cloudy bands, indicating that the fabric is less well confined in the cloudy bands than in the clear ice.
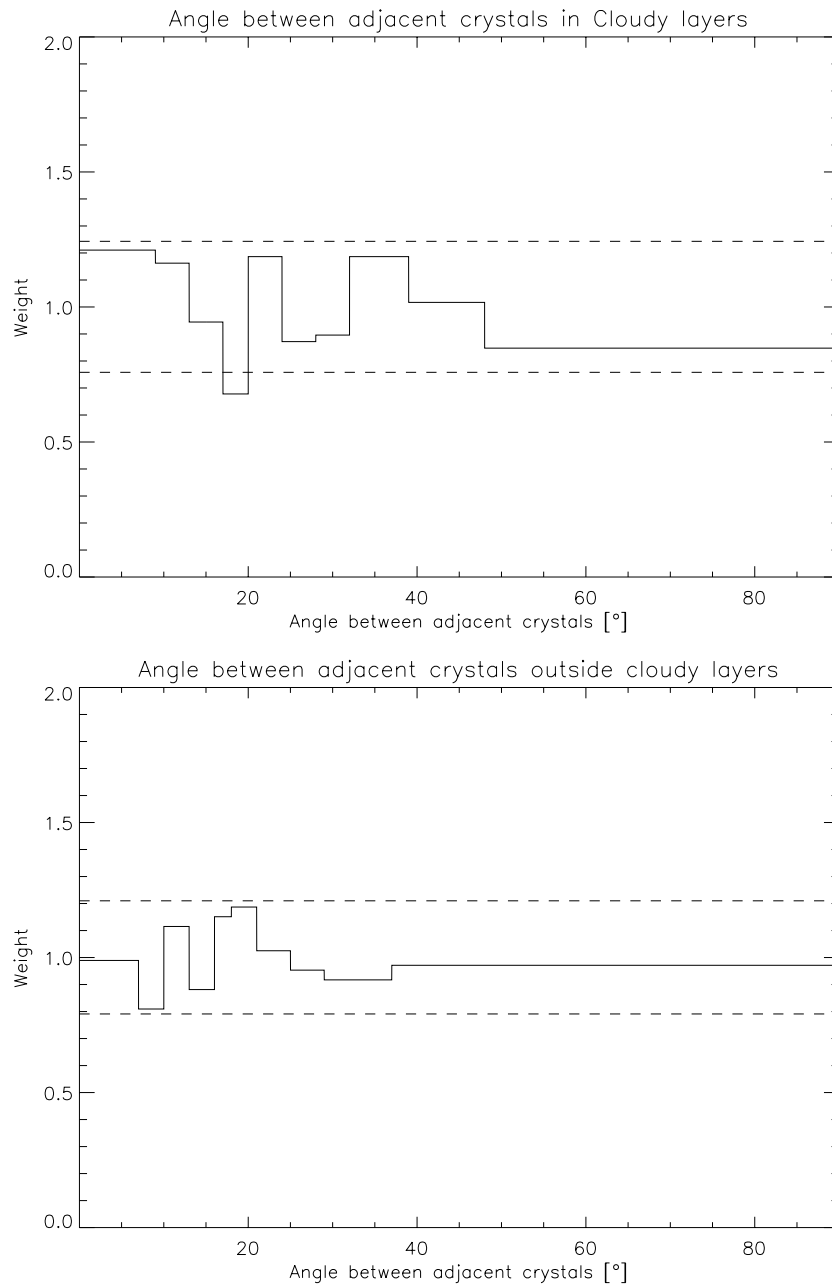
Figure 5.15: Upper: The angle between neighbour crystals inside cloudy bands. Lower: The angle between neighbour crystals outside cloudy layers. The dashed line mark the 95% confidence interval. Inside the cloudy band there is 253 crystals and 413 neighbour pairs, in the interstadial sample there is 289 crystals and 565 neighbour pairs.

# 5.5   Conventional mean area measurements

## 5.5.1   Linear intercept on horizontal thin sections

Test lines were applied 1 cm appart to the 6 horizontal thin sections, to prevent counting some crystals more than one time. About 100 crystals were sectioned by the test lines of the linear intercept method on each sample in each direction. The length of all test lines for the 6 samples and the number of crystals in each direction was added, and the mean crystal diameter in the direction was calculated. The results of the mean diameter in each direction is tabulated in table 5.3. It can be seen from the table, that there is no

| Direction [°] | $d$ [mm] |
|---|---|
| 0 | 2.52 |
| 45 | 2.62 |
| 90 | 2.54 |
| 135 | 2.54 |

Table 5.3: Mean crystal diameter ($d$) for the four measured directions on the horizontal thin sections.

significant difference between the diameter of the crystals in the four directions. The assumption about horizontal symmetry is therefore valid, and it is reasonable to investigate only vertical thin sections, since both horizontal and vertical crystal diameters can be obtained from them.

## 5.5.2   Vertical thin sections

The linear intercept measurements were carried out on 6 samples, one from each sample interval. For the measurement of the horizontal diameter on the vertical thin sections 7–8 test lines were applied, 1 cm appart, intersecting about 250 crystals in each sample. For the vertical measurements 5–6 test lines were applied, 1 cm appart, also intersecting about 250 crystals. I estimate the uncertainty on counting crystals intersecting the test lines to about 1–2 crystals per test line or about 5%. The results can be seen in table 5.4.

Thorsteinsson et al. (1997) repported a horizontal diameter of about 2 mm in 1982 m depth, and a horizontal diameter of about 2.3 mm and a vertical diameter of about 1.8 mm for sample at 2064 m depth. My results are thus in good agreement with the previous findings.

For the mean area measurements, a rectangle 10 mm wide was applied on each sample in the whole vertical extent of the sample, giving an area of

| Depth [m] | $d_H$ [mm] | $d_V$ [mm] | $A_{MA}$ [mm$^2$] |
|---|---|---|---|
| 2015.75 | 1.97 | 1.62 | 4.58 |
| 2017.95 | 1.90 | 1.82 | 4.38 |
| 2020.07 | 2.43 | 1.84 | 4.80 |
| 2024.55 | 2.75 | 2.09 | 6.18 |
| 2027.85 | 2.43 | 1.73 | 4.13 |
| 2029.42 | 2.26 | 1.78 | 4.28 |

Table 5.4: Depth of sample, horizontal ($d_H$) and vertical diameter ($d_V$) measured by linear intercept measurements and mean area ($A_{MA}$) measured by mean area measurements.

about 800 mm$^2$. The test area contained about 200 crystals in each sample. As for the linear intercept measurements, the uncertainty of the mean area measurement is about 5%. The result can also be seen in table 5.4.

# Chapter 6

# Discussion

In this chapter, I will comment on the results and compare them with other measured parameters from the GRIP ice core. I will start with a comparison of the mean area measurements, and an intercomparison of the textural parameters. Then I will make a comparison of the texture and fabric parameters, which is possible not only for the mean values, but also of the individual crystals. The texture and fabric results are also compared to measurements of $\delta^{18}$O, dust and soluble impurities in the ice. At the end, I will make an investigation of the textures and fabrics of cloudy bands.

## 6.1 Textural parameters

### 6.1.1 Comparison of mean area calculations

Since the individual crystal area method measures the area of each individual crystal, a mean area calculated from these measurements is the most accurate measure of the mean area in a section of the ice. Because the method is new, very few measurements have been carried out, and a comparison with conventional methods to determine the mean crystal area is therefore interesting.

The linear intercept measurements have been converted to a mean crystal area, by assuming ellipse shaped crystals. The area is then given by: $A_{LI} = d_H d_V \pi / 4$. The result is given in table 6.1 together with the mean area measured with the mean area method, and the calculated mean area from the individual crystal area method. It is seen from the table, that the mean area measured with the linear intercept and the mean area methods are both generally larger than the mean area found by the individual crystal area method.

| Depth [m] | $A_{LI}$ [mm$^2$] | $A_{MA}$ [mm$^2$] | $A_{ICA}$ [mm$^2$] | Flattening LI | Flattening ICA |
|-----------|-------------------|-------------------|--------------------|---------------|----------------|
| 2015.75   | 2.51              | 4.58              | 2.68               | 1.21          | 1.31           |
| 2017.95   | 2.72              | 4.38              | 2.72               | 1.05          | 1.36           |
| 2020.07   | 3.51              | 4.80              | 3.13               | 1.32          | 1.34           |
| 2024.55   | 4.52              | 6.18              | 4.27               | 1.31          | 1.35           |
| 2027.85   | 3.32              | 4.13              | 2.92               | 1.40          | 1.31           |
| 2029.42   | 3.16              | 4.28              | 2.41               | 1.27          | 1.31           |

Table 6.1: Depth of sample, mean area calculated from the linear intercept measurements ($A_{LI}$), the mean area measurements ($A_{MA}$) and the individual crystal area measurements ($A_{ICA}$). Flattening calculated from the linear intercept measurements and the individual crystal area measurements.

The values of $A_{LI}$ are both larger and smaller than $A_{ICA}$, indicating that there is no simple correlation between them. The mean ratio between $A_{ICA}$ and $A_{LI}$ is found to be 0.9, but with large variations (0.8–1.1) between the individual samples. When the test lines for the horizontal linear intercept measurements are placed with a constant spacing, the test lines are less likely to intersect narrow bands with small crystals, which contains a large number of crystals compared to the area they are occupying. This will thus tend to give a too large mean area of the linear intercept measurements.

A better measurement of the mean area of a sample with a horizontal band structure, is obtained with the mean area method, if the test area is covering the whole vertical extent of the sample. Thereby all the band structure will contribute to the calculated area. Small variations in the horizontal direction is not accounted for with a narrow test area. These could be included if the test area filled the whole area of the sample, an overwhelming task with 1500 crystals in each sample. The mean ratio between $A_{MA}$ and $A_{ICA}$ is found to be 0.6, with only small variations between the individual samples (0.6–0.7). Although counting the number of crystals within a given area is almost the same as the calculation of the mean area from the individual crystal area method, there is a somewhat large deviation, which is due to the treatment of the crystals at the boundaries of the test area. Apparently too few crystals are counted in this way, giving rise to a too large mean crystal area. Another factor that might account for some of the discrepancy between the two methods is the high resolution of the pictures used to the individual crystal area method. Crystals smaller than 0.2 mm$^2$ are measured, which will probably not be detected by the observer when the mean area method is measured on the sample.

The mean ratio between $A_{MA}$ and $A_{LI}$ is found to be 1.5, also with quite large variations (1.2–1.8). Jacka (1984) reported a correlation between the mean area measured by the linear intercept and the mean area methods of $A_{MA} = 1.7A_{LI}$. My results agree fairly well with this.

The flattening is in general a little lower for the linear intercept measurements than for the individual crystal area measurements, but with large variations. As for the mean area, this is because, when measuring the mean horizontal diameter, the bandy structure is not well covered with equidistant test lines.

This examination gives an indication of how to compare mean area calculated from the individual crystal area measurement with measurements of the conventional methods. To obtain a complete picture of the relation between the individual crystal area method and the conventional methods, a more thorough investigation is needed.

### 6.1.2 Intercomparison of textural parameters

To examine whether there is a correlation between the area, the flattening and the elongation direction of the crystals, the parameters were plotted in scatterdiagrams. This investigation did not reveal any unknown relations. The area is not correlating with the flattening or the elongation direction, neither for the individual crystals nor for the mean values of each sample. Not surprisingly there is a correlation between the flattening and the elongation direction for the individual crystals (The larger the elongation direction, the smaller is the flattening), but no correlation of the mean values of the two parameters.

There is thus no evidence that crystals with different areas have different flattening and/or elongation direction. This indicates that the physical processes determining the crystal textural properties are size independent at this depth interval.

## 6.2 Comparison of textures and fabrics

In figure 6.1, the mean crystal area and $R$, as an expression of the mean orientation of the crystals, is compared for the 28 samples with orientation measurements. Since the orientation measurements does not cover the whole sample, there might be some variations of the mean area in the part of the sample where the orientation is not measured that can influence the result. In general, I do not think the variations are significant. No general pattern can be seen from the figure, indicating that the general development
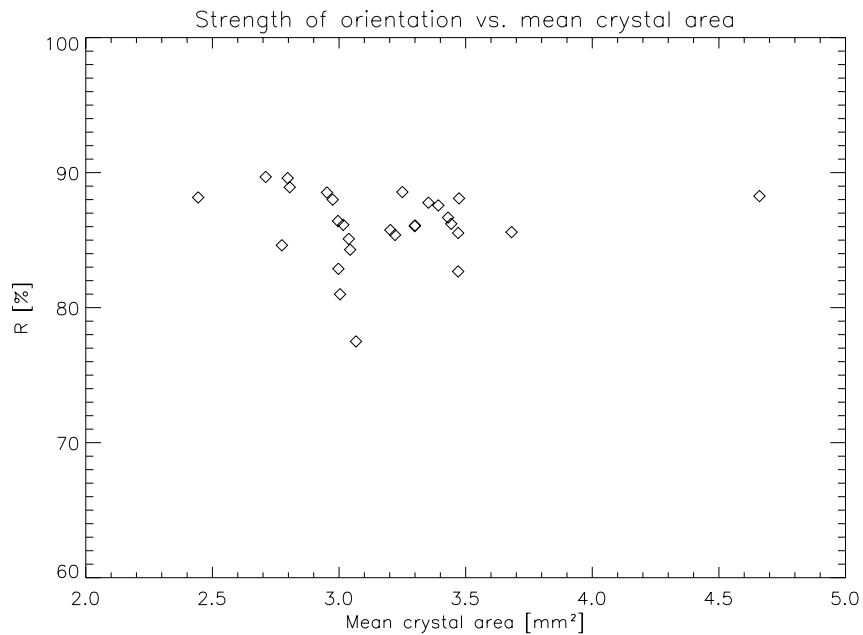
Figure 6.1: $R$ versus the mean crystal area.

of texture and fabric at this depth is independent. This does not exclude local variations, e.g. in the cloudy bands.

A comparison of $R$ with the mean flattening and mean elongation direction for the measured samples do not either show a correlation.

## 6.2.1   Texture and orientation of individual crystals

To find out whether there is a correlation between the size and the shape of a crystal and its orientation, the data for the texture and the c-axes orientation measurements were grouped for the interstadial sample from 2019.67 m depth. This sample was chosen, because it contains the largest number of measured c-axes (644) and has the smallest number of orientation errors. No distinct layers were observed in the sample.

Both textures and fabrics are measured using Image-Pro, but with different coordinate systems, due to different resolution of the pictures used. Therefore a coordinate transformation was applied to find the "texture" coordinate of a pixel from the fabric coordinate system.

If, e.g. small crystals deform more easily than large crystals, one should expect this to show in a plot of the crystal area versus the tilt angle, as small crystals would have lower tilt angles. Figure 6.2 shows the crystal area

as a function of the tilt angle. It is seen that there is no obvious correlation between the area of the crystal and its orientation. The other textural parameters gives similar results.
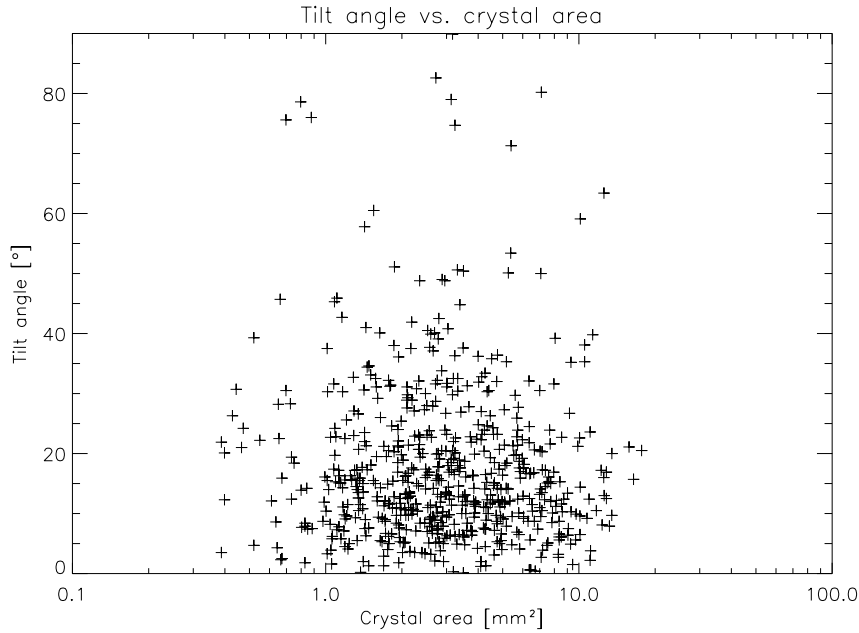


Figure 6.2: The area vs. the tilt angle of individual crystals in the sample from 2019.67 m depth.

Gow and Williamson (1976) examined the orientation of crystals larger than the double of the mean crystal area throughout the Byrd ice core. They repported no strong correlation between the area and orientation of the examined crystals.

The conclusion of this investigation is that there do not appear to be an overall correlation between the size and shape of a crystal and its orientation. This indicates that it is not the same processes that determines the texture and the fabric of ice crystals at this depth interval.

## 6.3 Mean area vs. $\delta^{18}O$ and impurities

There is in general a difference between the mean crystal area in the stadial and the interstadial samples, although it does not seem to follow the climate transitions defined by the $\delta^{18}O$ values (see figure 5.3). The transition between Holocene and Wisconsin is seen as a rapid drop in the $\delta^{18}O$

value in ice sheets. The transition has also been observed as a decrease
in the mean crystal size in all ice cores containing ice from the last ice
age [Paterson, 1991, Thorsteinsson et al., 1997]. Several explanations have
been suggested to account for the smaller crystals in the Wisconsin, in-
cluding temperature [Petit et al., 1987], zones with high horizontal shear
[Gow and Williamson, 1976], microparticles [Koerner and Fisher, 1979] and
soluble impurities [Alley et al., 1986b]. Many intercomparisons with other
measured parameters, such as $\delta^{18}O$ and soluble and insoluble impurities have
been made to test the proposed theories. One (or more) of the theories might
also explain why there is a difference in the crystal area between the inter-
stadials and the stadials.

It has been suggested that the decrease of the mean crystal size is due
to a built in "memory" of the lower surface temperature at the time of
deposition [Petit et al., 1987], but the theory is generally not believed, since
it does not take the effect of polygonization into account [Alley et al., 1988,
Thorsteinsson et al., 1997]. High shear zones can also be outruled, since
horizontal movements are negligible in the Wisconsin ice of the GRIP ice
core [Thorsteinsson et al., 1997]. This leave the concentration of impurities
as a possible cause for crystal area control.

I have made a comparison between the concentration of impurities, $\delta^{18}O$
and the mean crystal area of the samples. The GRIP $\delta^{18}O$ values have been
measured on the mass spectrometer in Copenhagen with a resolution of 8
samples per bag (6–7 cm per. sample) in the interval covering my samples
[Johnsen et al., 1992a]. Dust was measured on site at GRIP in a continuous
measurement with a resolution of 1 mm [Hammer, 2001b]. ECM (Electrical
Conductivity Measurement), which is a measure of the acidity of the ice, was
also measured continuously in camp [Taylor et al., 1993]. Ten different solu-
ble impurities ($Ca^{2+}$, $Cl^-$, $Na^+$, $Mg^{2+}$, $K^+$, $F^-$, $NH_4^+$, $SO_4^{2-}$, $NO_3^-$ and MSA)
have been measured on the ionchromatograph in Copenhagen with a resolu-
tion of 5 cm in the depth interval covering my samples [Steffensen, 2001]. Of
these, I chose not to use $F^-$, $NH_4^+$ and MSA since the concentration levels
were very low, almost at the detection level (for $NH_4^+$ mostly below the de-
tection level). ECM was not used either, since almost no signal is found at
this depth interval due to the high concentration of alkaline impurities.

There is a general correlation among the impurities including dust, and
an anticorrelation between the impurities and $\delta^{18}O$. Some of the soluble im-
purities are believed to have the same sources, and they correlates very well
[Hansson, 1994]. E.g. $Ca^{2+}$, $Mg^{2+}$ and $K^+$ mostly derive from continental
sources and show the same general pattern when compared to the mean area.
I will therefore only show the comparison between impurities and textures
and fabrics of some of the impurities. I have chosen $Ca^{2+}$ as a typical con-

tinental derived ion and $Cl^-$, which originates mainly from sea salt, as an ion with a marine source. $NO_3^-$ derives from atmospheric processes, and is mainly deposited as $HNO_3$. $SO_4^{2-}$ is mainly deposited as $H_2SO_4$ and has several sources, both continental and marine, and both volcanic, biogenic and non-biogenic. These four ions are also independently reported as inhibiting crystal growth in polar ice (see description below).

### $\delta^{18}$O

The mean area was resampled to a resolution of 7 cm, so a direct comparison with $\delta^{18}$O could be made. $\delta^{18}$O is plotted versus the mean crystal area in figure 6.3. $\delta^{18}$O tends to correlate with the mean crystal area, but with a
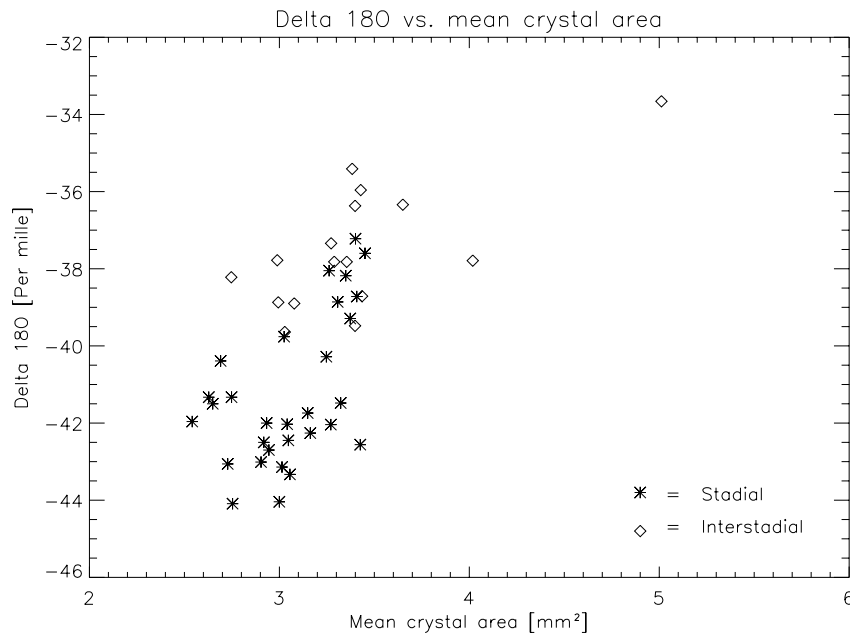


Figure 6.3: $\delta^{18}$O versus the mean crystal area. Samples from the interstadial are plotted with diamonds, and samples from the stadials are plotted with asterisks.

lot of scatter. There is though a clear evidence of a correlation between the crystal area and the climate.

Thorsteinsson et al. (1995) found that the crystal size correlates well with $\delta^{18}$O for values between $-39^0/_{00}$ and $-33^0/_{00}$ in the Eemian ice in the GRIP ice core, but the correlation breaks down for values greater than $-33^0/_{00}$. In the Eemian part of the ice core, the temperature is much higher than in the late

Wisconsin part. The higher temperature influences the grain growth, and could be the reason for the observed correlation in the Eemian ice.

I also find a general correlation between $\delta^{18}O$ and the mean crystal area although it is characterized by a lot of scatter. I have made a simple calculation of the influence of the temperature difference between the interstadial and the stadials in IS3 on crystal growth (see appendix B). It shows that there is no significant effect on the resulting crystal areas, since the temperature difference diffuse out fairly rapidly. Therefore another effect correlating with $\delta^{18}O$ is most likely the reason for the difference in crystal areas between stadials and interstadial. Since $\delta^{18}O$ anticorrelates with the concentration of impurities, these could be the reason. This idea is supported further by the investigation of the angle between adjacent crystals, that shows no preferred orientation between adjacent crystals (see figure 5.14). This indicates that boundary pinning is the most dominating effect determining the crystal size.

**Dust**

The mean area of the samples was resampled to a resolution of 5 cm in order to be compared directly to the measured impurities. The high resolution dust record was also resampled to a 5 cm resolution. Dust is plotted versus the mean crystal area in figure 6.4. There is no mixing between the interstadial and the stadial group of measurements. The samples from the interstadial all have relatively low levels of dust content, independent of crystal area, and the samples from the stadials show a lot of scatter.

Koerner and Fisher (1979) reported a strong relationship between microparticles and crystal size in the lowermost part of two ice cores from the Devon Island ice cap. The ice cores were believed to penetrate to the Wisconsin, where layers with small crystal sizes had a high content of microparticles. The concentration of soluble impurities in these cores was not measured. Duval and Lorius (1980) made a theoretic analysis of the effect of microparticles on the crystal growth, and concluded that the concentrations of microparticles was too low in existing ice sheets to have significant effect. This conclusion was also reached in a theoretic study of Alley et al. (1986a).

My results support the findings that microparticles does not seem to inhibit crystal growth. The concentration of dust in the stadial samples are up to 8 times as large as the concentration in interstadial samples containing crystals with the same mean crystal area. The general anticorrelation between dust and crystal size found by, e.g. Koerner and Fisher (1979), could also be ascribed to the soluble impurities which in general are found to correlate with dust in the ice sheets, e.g. [Langway, Jr. et al., 1988].
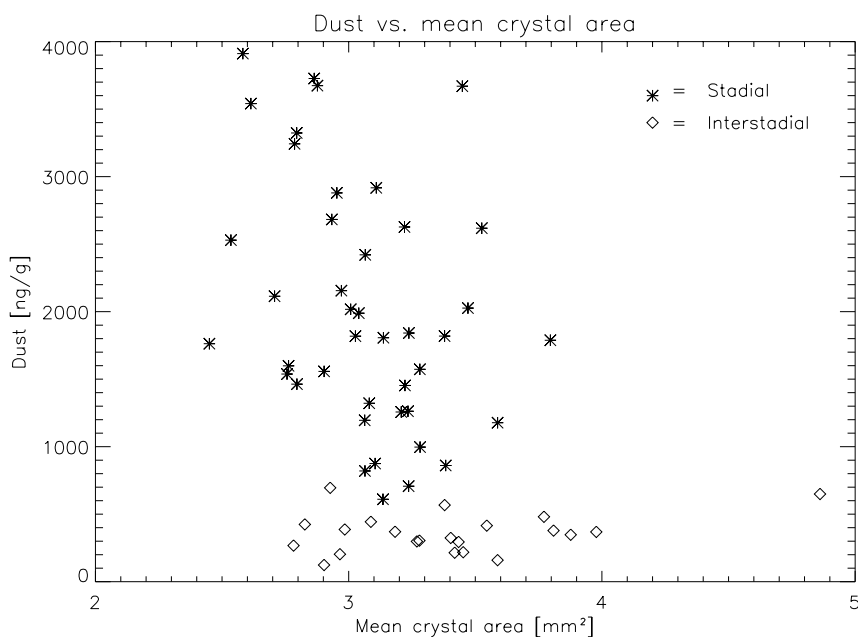
Figure 6.4: Dust concentration versus the mean crystal area. Samples from the intersta-dial are plotted with diamonds, and samples from the stadials are plotted with asterisks.

## Soluble impurities

The four ions $Ca^{2+}$, $Cl^-$, $SO_4^{2-}$ and $NO_3^-$ are plotted versus the mean crystal area in figure 6.5 and 6.6. The Calcium measurements show a clear division into two groups, one with the stadial samples, and one with the interstadial samples. The two groups have similar mean crystal area ranges. There is a tendency for a decrease in $Ca^{2+}$ with increasing crystal area for the stadial group, whereas the concentration of calcium in the interstadial group remains almost constant with increasing crystal area.

The chloride measurements also displays a tendency of division into two groups, although the groups are a bit mingled. There is more scatter in the chloride plot than in the calcium plot. The plot shows also a very weak tendency of an anticorrelation between the mean crystal area and the concentration of chloride in the stadial group, but not in the interstadial.

The sulfate measurements are also divided into two groups. Here there is a stronger tendency of an anticorrelation between sulfate and the mean crystal area in the stadial group than for the calcium, and also no apparent correlation in the interstadial group.
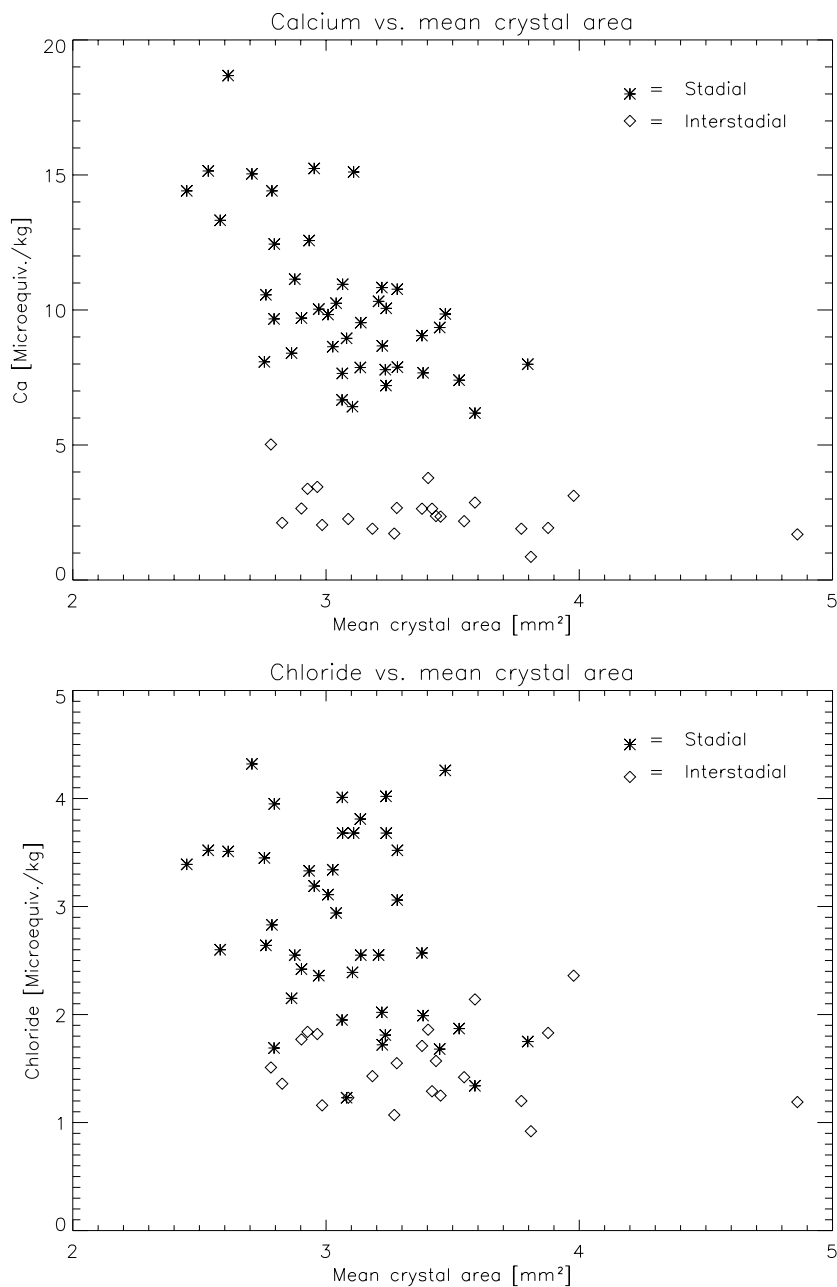
Figure 6.5: $Ca^{2+}$ (upper) and $Cl^-$ (lower) concentrations versus the mean crystal area. Samples from the interstadial are plotted with diamonds, and samples from the stadials are plotted with asterisks.

Figure 6.6: $SO_4^{2+}$ (upper) and $NO_3^-$ (lower) concentrations versus the mean crystal area. Samples from the interstadial are plotted with diamonds, and samples from the stadials are plotted with asterisks.
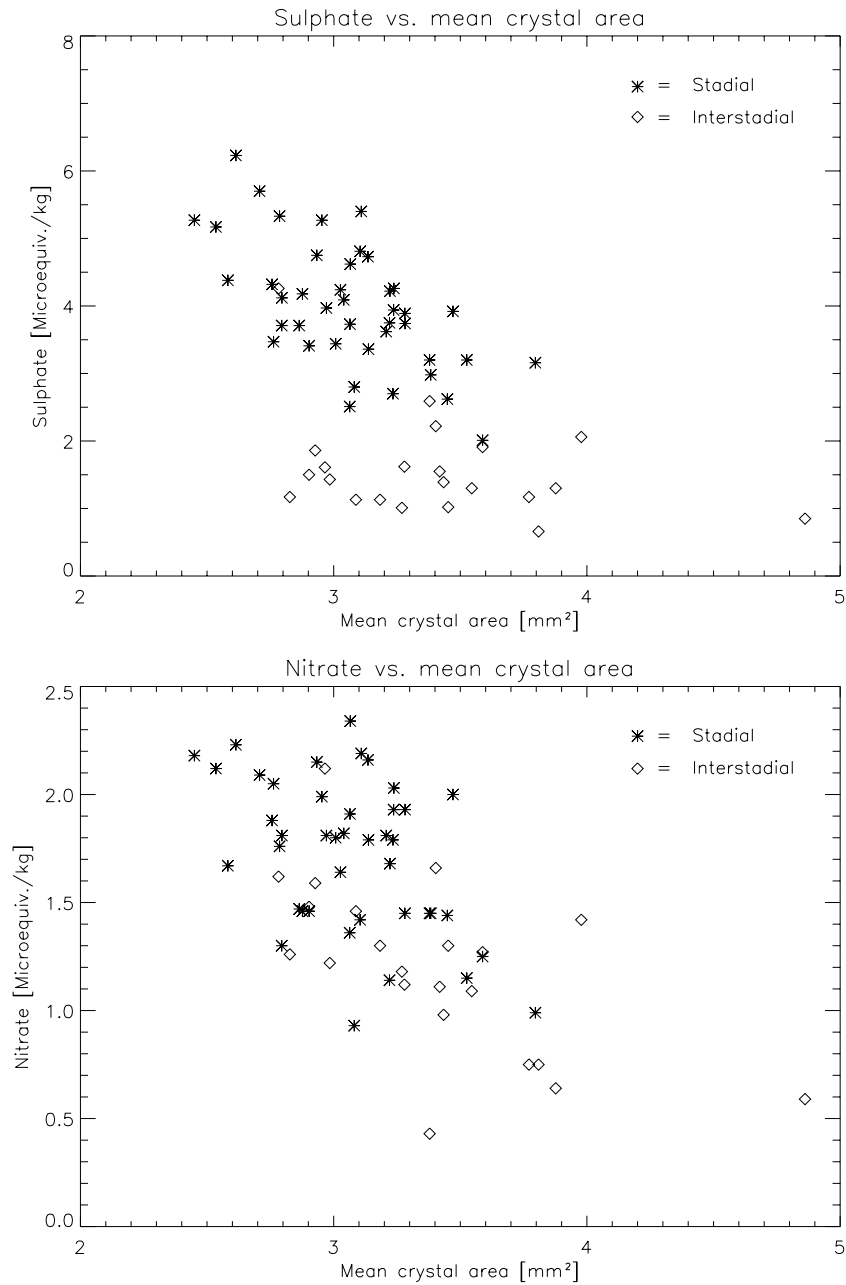
For the nitrate measurements, the samples in the stadials and the interstadial are clearly mixed. Here is also a tendency for an anticorrelation between the concentration of nitrate and the mean crystal area, although with a lot of scatter. Since the two groups of measurements are mixed, the anticorrelation is stronger than for any other impurity.

In a data study, Alley et al. (1986b), showed that the concentration of $Na^+$ and $Cl^-$ in the Dome C ice core could induce the impurity-drag force required to inhibit crystal growth. They stated that the dominant impurities inhibiting grain growth in the Wisconsin in Antarctica probably is sodium and chloride but that other impurities also could play a role. Langway et al. (1988) found an anticorrelation between crystal size and both $Cl^-$ and $SO_4^{2-}$ in the Wisconsin part of the Dye 3 ice core, and Madsen (1997) found that $SO_4^{2-}$ was the most likely impurity to inhibit grain growth in the Hans Tausen ice core. Azuma et al. (2001) has reported an anticorrelation between crystal size and $Ca(NO_3)_2$ in the Dome F core. Thorsteinsson (1996) used calcium as representing the concentration of impurities and found a general good anticorrelation between the impurities and the crystal diameter from 1300–2780 m depth in the GRIP ice core.

My analysis of the impurity content versus the mean crystal area shows that for chloride there is much scatter and an anticorrelation between the concentration of $Cl^-$ and the crystal area is hard to detect. The crystals in the interstadial and in the stadials can be divided in separate groups for $Ca^{2+}$ and $SO_4^{2+}$ measurements, each showing an anticorrelation with mean crystal area for the stadial group, but an independence of crystal area in the interstadial group. This indicates that there is a level of the concentration of impurities, that can trigger an area dependence. For calcium, the level appear to be around 6 $\mu$equiv./kg. This does not corresponds well with the results of Thorsteinsson et al. (1995), who repported a correlation of mean crystal size and calcium between 0.6 and 1.2 $\mu$equiv./kg for the Eemian ice. For values smaller or larger than this interval, the correlation breaks down. Thorsteinson et al. (1997) concludes that the saturation value also appears to be valid in the Wisconsin, but their curves show a significant correlation between the concentration of calcium and the mean crystal size also for much larger values. All values of the concentration of calcium in my samples, except 1, are larger than the saturation value of Thorsteinsson et al. (1997). This indicates either that there is a much more complex structure of the influence of the impurities on grain growth (e.g. a temperature dependence), or that calcium is not a main impurity in inhibiting grain growth. Although a temperature dependence can not be outruled, I tend to accept the last suggestion, also supported by the other observations in my samples.

For sulfate ions, there appear to be a trigger level at about 2 $\mu$equiv./kg. Langway et al. (1988) does not reports a breakdown of the correlation between the concentration of sulfate and the mean crystal area in the Dye 3 ice core. The lowest concentration in the Wisconsin part of this core is about 1 $\mu$equiv./kg at about 2000 m depth (length of core is 2037 m). There appear to be a less well correlation between the crystal area and the concentration of $SO_4^{2-}$ at this depth, and it could indicate a trigger level. The reason for the apparent break down of the correlation at this depth could also be that it is close to the bottom. This level is about half the level I found, which gives the same indications as for the calcium. Since the observations are not very certain, I will not draw any conclusions from them.

Nitrate is the only impurity where the stadial and interstadial measurements are mixed. This is a strong indication that $NO_3^-$ plays a larger role in the inhibition of the crystal growth than do other examined soluble impurities. The concentration of nitrate in IS3 is not different than the concentration in the Holocene part of the ice in the GRIP core. In the Camp Century and Dye 3 ice cores, the concentration of $NO_3^-$ is lower in the Wisconsin than in the Holocene [Paterson, 1991]. This weakens the argument of nitrate as the controlling impurity of the crystal boundary pinning. I suggest that the reason that boundary pinning does not take place in the Holocene is due to the higher temperature at the time of precipitation, and hence a higher growth rates for crystals in this ice.

## 6.4 Fabrics compared to $\delta^{18}$O and chemistry

The strength of the fabric ($R$) has also been compared to $\delta^{18}$O and the impurity concentration of the ice. The resolution of the fabric measurements are about 5 cm, but not necessarily the same 5 cm that the impurities are measured in. The two data set have been compared sample for sample where it was possible, which was half of the measurements. For the other half, the fabric measurement was covering parts of two impurity measurements, the mean of these two were taken and compared to the fabric measurement.

A re-sampling of the $\delta^{18}$O measurements was made in the same way. The result of the comparison between $R$ and $\delta^{18}$O can be seen in figure 6.7. As can be seen from the figure, the strength of the single maximum fabric does not appear to correlate with the climate.

The concentration of dust in each sample has been plotted versus $R$ in figure 6.8. There is a clear division of the samples into two groups, one with the stadial samples and one with the interstadial samples. There is far more scatter in the $R$-value for the interstadial samples than for the
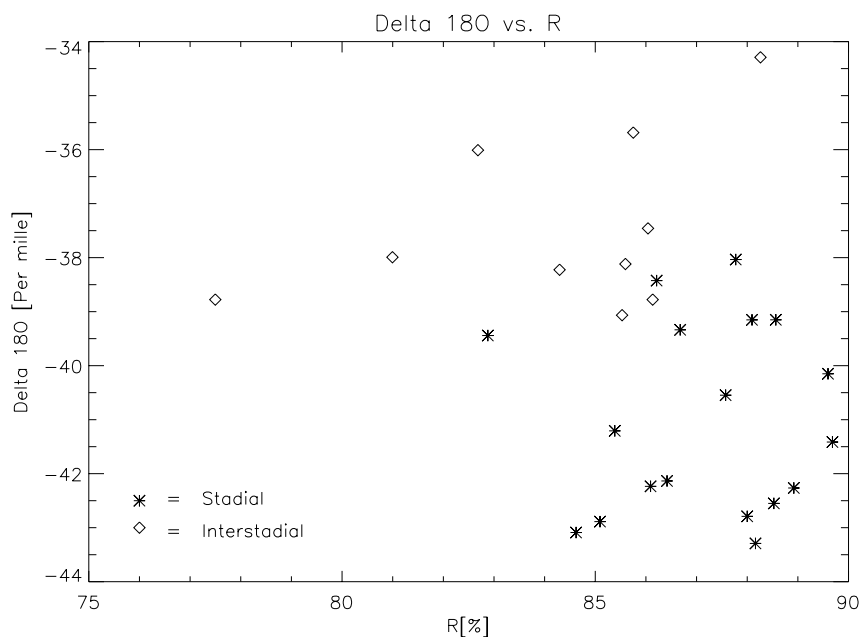
Figure 6.7: $\delta^{18}$O versus the strength of the single maximum fabric. Samples from the interstadial are plotted with diamonds, and samples from the stadials are plotted with asterisks.

stadial samples. The strength of the single maximum fabric appear to be independent of the concentration of dust for the samples from the interstadial, whereas there is a tendency of a correlation between the concentration of dust and the fabric strength for the samples from the stadials.

As an example of the plots of the soluble impurities versus fabric, nitrate has been plotted as a function of $R$ in figure 6.9. It can be seen that there is no correlation between the concentration of nitrate and the strength of the fabric. This appear to be the case also for Sulfate, Sodium and Chloride. For Potassium, Calcium and Magnesium there appear to be a correlation for the stadial samples like for the dust concentration, which is not surprising, since all three impurities are believed to have mainly continental sources and correlates very well with dust.

From figure 5.12, there is an indication of a strengthening of the fabric with depth, which is the overall tendency in the GRIP core in this depth interval [Thorsteinsson et al., 1997]. Therefore one should be carefull of stating a correlation between dust and fabric, since the strongest fabric is found in the deepest samples, which also happens to be from the coldest period, and have the largest concentration of impurities, both soluble and insoluble.
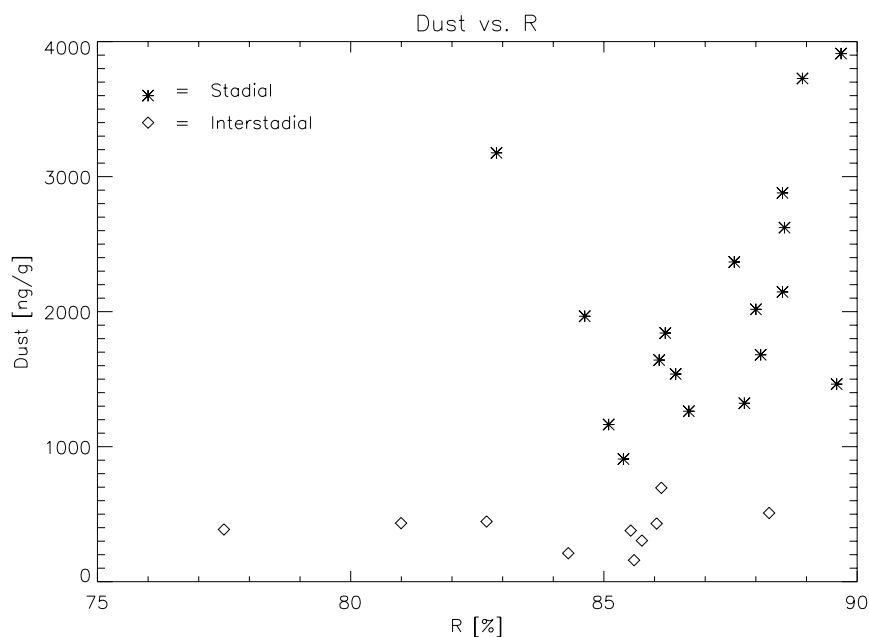
Figure 6.8: Dust concentration versus the strength of the single maximum fabric. Samples from the interstadial are plotted with diamonds, and samples from the stadials are plotted with asterisks.

On the other hand, "soft" ice, easily deformable by horizontal shear, is characterized by a strong single maximum fabric and a high content of impurities is found in the Wisconsin part of e.g. the Dye 3 and Camp Century ice cores [Paterson, 1991]. The strong fabric in this impurity-ladden ice and the correlation with dust content could thus be a sign of increased horizontal shear. What contradicts this is, that the horizontal movement of the ice at this depth is negligible [Thorsteinsson, 1996], and that dust is unlikely to be the controlling factor for a "soft" ice [Paterson, 1991]. Since no correlation has been found for the fabric with crystal area and the non-continental soluble impurities, there is most likely no increased horizontal shear at this depth interval. This makes it more probable, that the apparent correlation is a feature of the sampling.

## 6.5   cloudy bands

The ice in the stadials is dominated by very distinct cloudy bands (see figure 5.1 and appendix A). Some of the cloudy bands can be seen as bands of crystals with smaller area than the surrounding ice. To find out more about
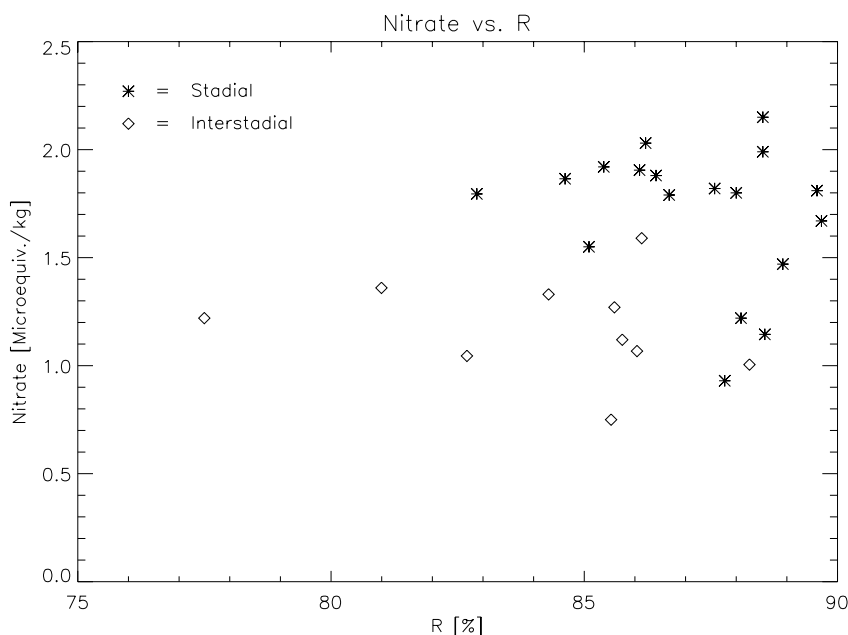
Figure 6.9: Nitrate versus the strength of the single maximum fabric. Samples from the interstadial are plotted with diamonds, and samples from the stadials are plotted with asterisks.

the composition of the crystals in the cloudy bands, an investigation of the textures and fabrics of cloudy bands was made.

## 6.5.1  Visual stratigraphy compared to the mean area

A mean intensity of each sample was calculated from the intensity measurements (see section 5.1), and this was compared to the mean crystal area of each sample. This comparison revealed a slight anti-correlation between the mean intensity and the mean crystal area, with a tendency of splitting into two groups: The samples from the stadials and the samples from the interstadial, like for the calcium measurements.

A more detailed comparison was made between the intensity and the number of crystals in bands of the samples. The intensity records were assembled in bags by putting the mean horizontal intensity of the individual samples together, and calculating the mean intensity in bands of 1 cm. The texture data was assembled in the same way, and the number of crystals in each 1 cm interval was counted as a measure of the area of the crystals. A crystal is said to be inside the interval if its center is in the interval. A

resolution of 1 cm was chosen to have a statistically significant number of crystals in each interval. It is seen from figure 6.10, that there is about 200 crystals in each interval. Since crystals at the edges of a sample are removed from the texture analysis, the intervals near the boundaries between the individual samples are incomplete and do not show the real number of crystals in these intervals. The intensity measurements lack typically a couple of mm at each edge, so there is an uncertainty on this assembly of about 0.5 cm for each sample. The curves for the mean intensity and the number of crystals in each interval has been plotted with depth in figure 6.10.
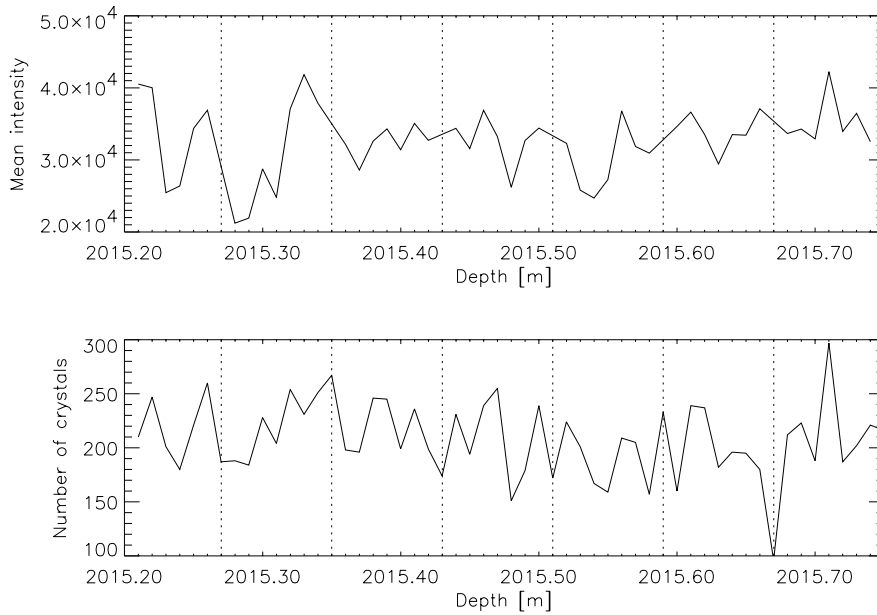
Figure 6.10: The mean intensity in 1 cm intervals (top) and the number of crystals in the same interval (bottom) for the samples in 2015.20–2015.75 m depth. The dotted lines marks the boundaries between the individual samples, where the two records are incomplete.

It can be seen from the figure, that the two curves overall correlates fairly well. The correlation is in general lower for the samples in the interstadial than in the stadials. This is because the intensity is lower in the interstadial and does not show as large a variation. A calculated correlation for each of the six sample intervals gives correlation coefficients of less than 50%. The boundaries between the individual samples are also marked in figure 6.10, and it is seen that the two curves differ at all these locations, indicating that the overall correlation is better that the calculated.

It is also seen that the interval with the largest amount of crystals is one of the brightest intervals, but that intervals with the same brightness does not contain as many crystals. This indicates that not all layers seen as cloudy bands on the thick sections contains small crystals. This is confirmed by a visual inspection of individual samples, where some cloudy bands not can be seen as bands with small crystals.

Cloudy bands in the Byrd core have been found always to be associated with smaller crystals than outside the layers [Gow and Williamson, 1976]. A similar strong conclusion can not be reach from my investigation of the intensity of the cloudy bands. If the cloudy bands are associated with a high content of microparticles, as generally assumed [Thorsteinsson, 1996], this supports the conclusion that insoluble impurities does not hinder the crystal boundary migration, since there is only an overall correlation between the abundance of cloudy bands and layers with small crystals. This is further investigated in section 6.6.

### 6.5.2   Textures of cloudy bands

In figure 5.6 on page 55, the area distribution of the crystals in cloudy bands in 7 stadial samples are plotted together with the distribution of the crystals outside the cloudy bands, and for all the crystals in the 7 samples. It is seen, that the area distribution has the same form inside and outside the cloudy bands, but with considerably smaller log-normal mode inside the bands than outside.

3 interstadial samples were added to the above mentioned 7 samples, to make a further analysis of the textural parameters of the cloudy bands. The sections all had very distinct cloudy bands on the photos of the thick sections, and distinct bands of crystals smaller than average on the photos of the thin sections. The boundaries separating cloudy bands from clear ice were determined by visual inspection. The mean crystal area and the mean flattening for the crystals inside and outside the cloudy bands is seen in table 6.2. Four of the samples had more than one cloudy band. For these samples, the calculations of mean area and flattening were made for each cloudy band. Since no significant difference between the bands was found, the mean area and flattening was calculated for the sum of the crystals in the bands, which is the reported result in the table. From the table it can be seen, that not only are the mean crystals area smaller in the cloudy bands than outside, they are are also slightly more flattened. The crystals inside the cloudy bands are on average 46% smaller, and on average 6% more flattened than the crystals outside the cloudy bands. The more flattened crystals indicates that there is a higher horizontal strain inside the cloudy bands than outside the bands.

| Depth [m] | CB Mean area [mm$^2$] | NCB Mean area [mm$^2$] | CB mean flattening | NCB mean flattening |
|---|---|---|---|---|
| 2017.95 | 1.84 | 3.40 | 1.38 | 1.35 |
| 2017.87 | 1.79 | 3.27 | 1.40 | 1.32 |
| 2019.75 | 1.87 | 2.90 | 1.43 | 1.33 |
| 2024.31 | 1.69 | 3.30 | 1.38 | 1.35 |
| 2024.23 | 1.84 | 3.72 | 1.39 | 1.25 |
| 2027.77 | 1.70 | 3.63 | 1.32 | 1.30 |
| 2027.61 | 1.64 | 2.99 | 1.41 | 1.31 |
| 2027.37 | 1.77 | 3.38 | 1.36 | 1.33 |
| 2029.18 | 1.60 | 2.75 | 1.43 | 1.29 |
| 2029.10 | 1.76 | 3.29 | 1.37 | 1.32 |

Table 6.2: Depth of samples, mean area, and mean flattening for crystals inside cloudy bands (CB) and outside cloudy bands (NCB). The double horizontal lines marks the boundaries between interstadial and stadials.

## 6.5.3 Fabrics of cloudy bands

The angle between adjacent crystals inside and outside a cloudy band was investigated in section 5.4.5. This investigation indicated that crystal boundary migration was slowed by boundary pinning both inside and outside the cloudy band.

For 7 of the samples from the cloudy band texture analysis, the c-axes orientation was measured in detail. The $R$-parameter was calculated for the crystals inside and outside the cloudy bands. Two of the samples had more than one cloudy band. For these samples, the calculation of $R$ was made both for each band separately and for the sum of the bands. The results for each band separately had the same characteristics as the result of the sum of the bands, and the latter is reported. Two fabric diagrams, one for the crystals inside the cloudy bands and one for the crystals outside is seen in figure 6.11, and $R$ and the number of crystals used to calculate $R$ is found in table 6.3.

The result clearly shows a tendency of a less strong single maximum inside the cloudy bands than outside. This result has earlier been reported by [Miyamoto et al., 1999] for the GRIP ice core. It is in contradiction to what Gow and Williamson (1976) found from the Byrd ice core. Except for the uppermost cloudy band in the Byrd core, crystals inside the cloudy bands were more tightly clustered around the vertical than was crystals in the surrounding ice. They argued that these bands with fine grained ice could

Figure 6.11: Fabric diagrams for the crystals inside a cloudy band (left) and outside (right) for the sample at 2029.18 m depth. 200 randomly chosen c-axes inside and outside the cloudy band respectively are plotted in the fabric diagrams.

| Depth [m] | CB No. of crystals | CB R [%] | NCB No. of crystals | NCB R [%] |
|-----------|--------------------|----------|---------------------|-----------|
| 2017.95   | 130                | 82.2     | 426                 | 86.0      |
| 2017.87   | 148                | 84.5     | 387                 | 87.2      |
| 2024.23   | 119                | 75.9     | 428                 | 85.3      |
| 2027.77   | 70                 | 82.2     | 495                 | 88.6      |
| 2027.61   | 118                | 85.0     | 415                 | 90.9      |
| 2029.18   | 253                | 85.3     | 289                 | 90.8      |

Table 6.3: Depth of samples, $R$ and number of crystals in the calculation of $R$ for crystals inside cloudy bands (CB) and outside cloudy bands (NCB).

constitute zones with higher horizontal shear stress. High horizontal shear stress should increase the strengthening of the single maximum fabric. Since I find a less well confined fabric in the cloudy bands, this clearly indicates that there is not an enhanced horizontal shear stress in the cloudy bands in this part of the GRIP core.

Non-uniform deformation was observed on a centimeter scale in deformation tests on GRIP ice core ice, and the deformation mechanism is expected to be different in the cloudy bands than in clear ice [Miyamoto et al., 1999]. According to Miyamoto et al. (1999), Miyamoto et al. (1997) found that there was no clear correlation between the deformation rate and the number of cloudy bands in uniaxial deformation tests.

To explain the reason for the smaller and more elongated crystals inside the cloudy bands than outside, I assume that the crystals are small due to a high concentration of soluble impurities. In section 6.6, I will investigate

this assumption further. If we discart the idea of a higher deformation rate in the cloudy bands than outside, the more elongated crystals in the cloudy bands is most probably due to a lower polygonization rate. This would be in good agreement with the common believe, that polygonization acts on large crystals, where all crystals in the cloudy bands are small. This is supported further by the visual observation of no or very few strain shadows in the cloudy bands.

The less well confined fabric in the cloudy bands is more difficult to interpretate. Small crystals tend to have a higher dislocation density, because crystal boundaries block the movement of dislocations, and small crystals have a larger area of boundaries per. unit volume. Therefore small crystals have more stored energy, and should be able to recrystallize more rapidly by migration recrystallization [Paterson, 1991]. According to Duval and Castelnau (1995), the temperature acquired for migration recrystallization is about -10°C, a temperature much higher than the measured temperature of -30°C at 2000 m depth in the GRIP core [Gundestrup et al., 1993]. It is therefore not likely that the less well confined fabric is due to migration recrystallization.

Another explanation for a less well confined fabric inside the cloudy bands is a higher grain boundary mobility. If the boundaries are more mobile, some of the deformation energy will go into sliding of the crystal boundaries, which would result in a lower stress on the individual crystal, and a lower deformation of the crystal.

Zhang et al. (1994) made a simulation of the effect of grain boundary sliding on polycrystalline aggregates in pure shear. They found that, including grain boundary sliding in the deformation of polycrystals strengthened the fabric compared to deformation by sliding of basal planes only. This is explained by a reduction in grain interaction, which makes strain compatibility between adjacent grains less significant. However, if the grain boundary sliding was increased in the simulation, the fabric weakened, in consistence with the general assumption about the role of grain boundary sliding by structural geologists [Zhang et al., 1994]. The weakened fabric is explained by an accommodation of a significant part of the bulk deformation by the grain boundary sliding, hence a lower deformation by basal plane sliding and the accompanied grain rotation.

A drawback of this theory is that the grain boundary sliding is accompanied by the formation of vacancies between the crystals, which seems very unlikely at a depth of 2000 m in an ice sheet. Significant intragranular deformation processes must therefore be involved to compensate for the vacancies [Zhang et al., 1994].

I suggest, that the factor making the boundaries more mobile in the cloudy bands might be dust, although I have not found any information about the role of dust on grain boundary sliding in the literature. This would fit with the general opinion on cloudy bands as ice with a high dust concentration.

More mobile crystal boundaries would also support the proposed lower polygonization rate, since crystals subject to a high stress, might be able to lower the high stress by grain boundary sliding, without being polygonized. A lower polygonization rate is also observed in the grain boundary sliding simulation of Zhang et al. (1994).

## 6.6   High resolution dust and $NO_3^-$

In the GRIP camp, dust and nitrate was measured continuously along the core [Hammer, 2001b]. A 1 cm deep channel was melted in the core, and the water sucked into an instrument for analysis. The resolution of the data is in principle 1 mm. In practice the resolution is lower, since it depends on several factors, such as a constant melting rate. The exact resolution is not known, like the validity of the data has not been established. I have taken the mean of the data over a 1 cm interval, which for the $NO_3^-$ might be to low a resolution [Hammer, 2001a]. The estimated error is within few centimeters. The continuous nitrate measurements do not reproduce the nitrate measurements from the ionchromatograph exactly. The general level in the depth interval is about the same, but locally the two measurements differ up to 100%.

I have compared the 1 cm mean dust and nitrate data with the intensity and the crystal texture data. As for the intensity analysis, the crystals in 1 cm intervals have been counted as an expression of the mean area. An example of the comparison can be found in figure 6.12. It is evident from the figure that there is a general correlation between dust and nitrate, although they do not correlate perfectly. There is in general more variation in the dust content than in the nitrate content. A calculated correlation coefficient between the two curves gives about 50% for the showed depth interval. For the stadials it is generally about 30% and for the interstadial intervals it is less than 20%.

There do not appear to be a direct correlation between the concentration of impurities and the intensity of the ice. But the two two curves can be wiggle-matched fairly well. Although the data records should be quite equidistant on the 55 cm interval, a wiggle-matching may be justified by the uncertainty of both the assembly of the individual samples of the intensity
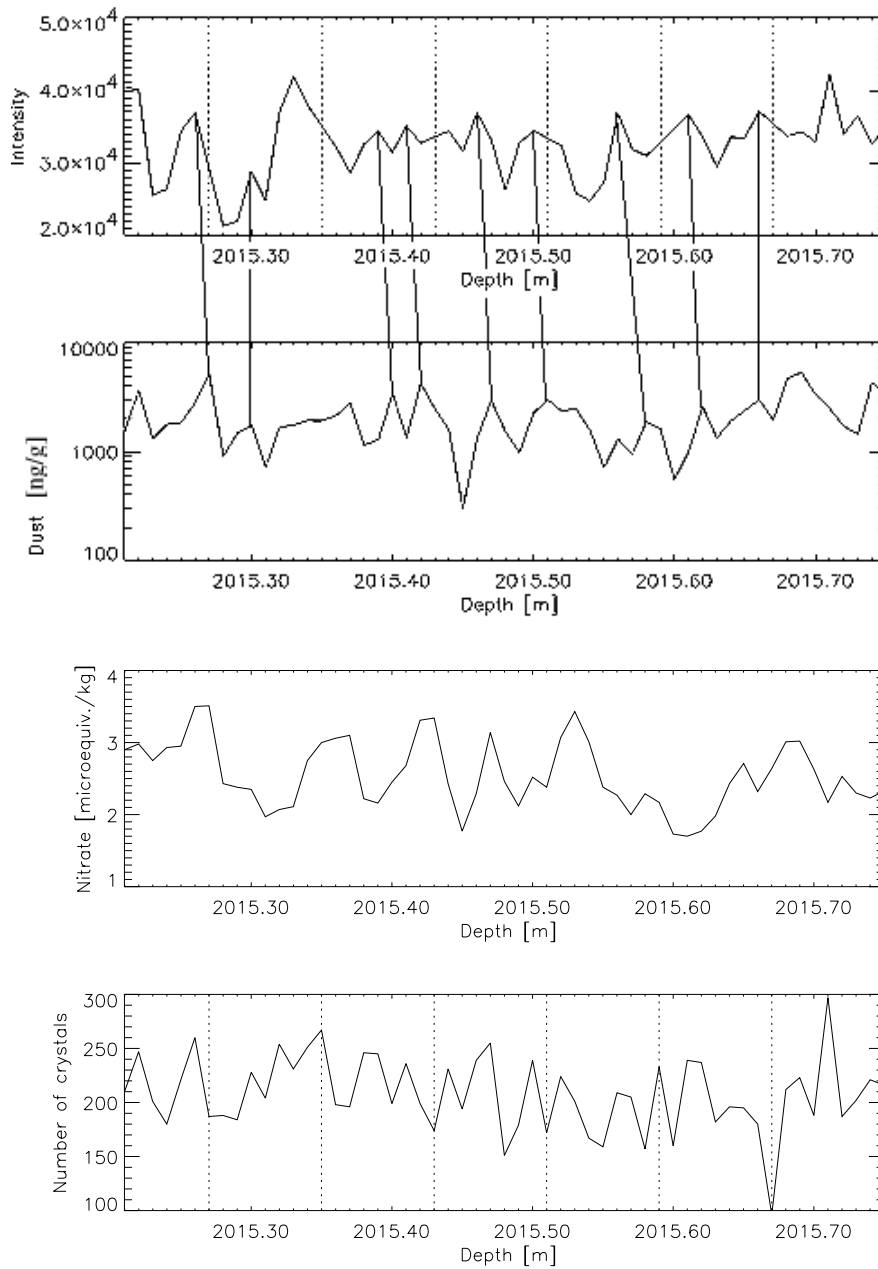
Figure 6.12: Mean horizontal intensity (upper), mean dust (upper middle), the mean nitrate (lower middle) and number of crystals (lower) in 1 cm intervals through the bag at 2015.20–2015.75 m depth. The dust have been plotted on a logarithmic scale. The dotted lines in the intensity and crystal plots shows the borders between the individual samples. The solid lines between the intensity and the dust concentration indicates where the curves can be wiggle-matched.

analysis, and by the uncertainty of the continuous dust measurement. It seams like the intensity record lags the dust concentration record with about 1 cm throughout the sample interval. A direct correlation can not be obtained, even with the wiggle-matching. This questions the general opinion, that the cloudy bands consist of a large concentration of dust particles. On the other hand, it could also be the reason that Miyamoto et al. (1997) did not find any clear correlation between the deformation rate and the number of cloudy bands in the ice. A firm conclusion can though not be made from this comparison.

It can also be seen from the figure, that there is no direct correlation between the dust and nitrate content and the crystal area. Even when the discrepancies at the borders between the individual samples are removed, there do not appear to be a correlation. A wiggle-mathing between the curves can also be made here, although more speculative than for the intensity. This is a general feature for all the samples. This questions my assumption from the previous section, that the small crystals in the cloudy bands are due to the concentration of impurities. It could also be taken as an evidence for, that it is not nitrate that is the dominating impurity in the boundary pinning. Since the validation of the data has not been established, a firm conclusion from this investigation can not be made.

# Chapter 7

# Conclusion

The purpose of this thesis was to implement semi-automatic methods to measure textures and fabrics of ice crystals, and to investigate changes in textures and fabrics of ice crystals across a Dansgaard-Oeschger event about 25000 years ago in samples from the GRIP ice core. In this chapter, I will summarize and conclude on the results and discussions from the previous chapters. At the end, I will suggest subjects for further studies.

**Measurements of textures and fabrics**

To measure ice crystal textures, I have implemented a new semi-automatic method based on image processing software [Wang and Azuma, 1999]. The measurements were very successful. I have measured the textures of more than 60000 crystals from 41 samples and found that the men crystal area inside and outside the interstadial is 3.36 mm$^2$ and 3.04 mm$^2$ respectively, yielding a difference of about 10%. I also found, that the area distribution approximately can be fitted with a log-normal distribution, which for all crystals have a log-normal mode of 2.12 mm$^2$. The shape of the distribution is invariant across the Dansgaard-Oeschger event, indicating that the dominating physical process determining the crystal area distribution is not changing. This is supported by a constant mean form factor. A further support for no changes in the process determining the crystal area, is given by an examination of the angle between c-axes of adjacent crystals. Two samples were investigated, one stadial and one interstadial, and no significant difference between the samples was found.

The investigation of the angle between c-axes of adjacent crystals also indicates that boundary pinning is the dominating process determining the crystal texture. This is further supported by a comparison of the mean area with the amount of impurities. There is a general correlation between the

mean area and soluble impurities, with strong indications of nitrate as the most dominating impurity in the boundary pinning process. A correlation between the mean area and the climate ($\delta^{18}$O) was also found. This can be explained by the correlation between the mean crystal area and the soluble impurities, since $\delta^{18}$O and the impurities correlates in general.

The finding of an apparent log-normal area distribution is in agreement with the indication that boundary pinning is the dominant process in determining the crystal texture. Boundary pinning should result in no or very slow development of the texture, basically preserving the normal grain growth properties of the texture [Alley et al., 1995b], where one of the properties is a log-normal area distribution.

A better fit to the area distribution was found to consist of two log-normal distributions, one containing the bulk of the crystals with a log-normal mode of 2.46 mm$^2$, and a small distribution containing about 10% of the crystals, with log-normal mode of 0.59 mm$^2$. The reason for an overlying distribution with very small crystals is possibly due to the sectioning effect, where only corners of some of the crystals are cut by the sample plane, although there is no experimental evidence for this.

The orientation of more than 10000 crystals was measured using a newly constructed Automatic Ice Fabric Analyzer [Wang and Azuma, 1999]. Although the resolution of the optics in the instrument was not completely satisfying, and about 10% of the measurements had to be discarded, essentially because the crystals were too small to be measured, enough crystals were measured to make a thorough analysis of the fabrics of an interstadial.

The fabric diagrams displays a strong single maximum fabric, and the degree of orientation is on average $R \approx 85\%$. There appear to be a general strengthening of the fabric with depth, with small variations across the interstadial. These variations do not seem to be significant, since there is no correlation between the strength of the fabric ($R$) and neither $\delta^{18}$O, nor mean crystal area or non-continental soluble impurities. An apparent correlation between $R$ and the dust concentration of the ice can be a coincidence, and must be investigated further before a conclusion can be drawn.

An interesting new comparison, made possible with the automatic measurements of textures and fabrics, showed that there do not appear to be a general correlation between the size and shape of the individual crystals and the orientation of their c-axes.

### Investigation of cloudy bands

Cloudy bands are seen in thick sections of the ice. In the thin sections, some of the cloudy bands can be found as bands of small elongated crystals compared

to the crystals in the rest of the sample. An evident, but weak anticorrelation is found between the mean horizontal intensity of the thick sections and the mean area of crystals. It is believed, that cloudy bands in general are associated with a high dust concentration. Since the cloudy bands do not correlates very well with the abundance of small crystals, one could take it as a confirmation that small crystals in the ice do not originate from boundary pinning by the concentration of insoluble impurities. A correlation between a high resolution dust and nitrate concentration data record with the mean area and intensity shows no direct correlation, although a wiggle-mathing of the curves for the dust concentration and intensity gives an indication of a correlation. The general believe of cloudy bands as originating from the dust concentration may thus not be valid. The correlation between nitrate and the crystal area can also be wiggle-matched, but the correlation is even weaker.

If the high resolution analysis is not considered, it can be assumed that the small crystals in the cloudy bands are due to high amount of soluble impurities, and the cloudiness of the cloudy bands are due to a high concentration of dust. With these assumptions, the larger flattening of the crystals in the cloudy bands can be explained by a lower polygonization rate. This is confirmed by a visual inspection, yielding almost no strain shadows in the cloudy bands. The fabrics of the cloudy bands are less well confined than the fabrics outside the cloudy bands. This is in accordance with earlier findings for the GRIP ice core, but in contradiction with findings from the Byrd ice core. With the assumptions mentioned above, I suggest, that the less well confined fabrics are due to grain boundary sliding. This further supports the idea of a lower polygonization rate as a reason for the more elongated crystals, since crystals with a high imposed stress could relieve some of the stress by grain boundary sliding. A higher grain boundary sliding rate could be due to a high dust concentration, although no experimental evidence for this is given.

These ideas depends on the two assumptions, which the high resolution impurity analysis does not support directly. Further investigations have to be made to either verify or discard the high resolution impurity analysis before a firm conclusion can be made on the subject.

## Recommendations for further studies

The implemented semi-automatic method to measure textures has proven to be very efficient by measuring a large number of very small crystals, although 10–15% of the crystal outlines had to be corrected. The need for correcting the automatic determined crystal outline shows the limitations of

the method, like it is not evident that the found combination of filter parameters will give just as good results with samples from other depths in ice sheets, containing crystals with other textural properties. I would therefore recommend that samples from different depths is measured with the method, and that the effect of the individual filter parameters from Image-Pro and their combination is studied thouroughly. This would hopefully show if there is an optimal adjustment of the filter parameters that would be efficient on all samples, which would be preferable, or if the method has to be adjusted to the individual samples.

When the crystal boundary detection method has been optimized (if necessary) many interesting investigations can be undertaken. One of the most interesting would be to investigate the area distribution in other parts of the ice sheet than the late Wisconsin that I have investigated. It would especially be interesting to find out whether the area distribution is log-normal shaped in the normal grain growth regime and whether it does change in the polygonization regime as suggested by the measurements of Thorsteinsson et al. (1997).

When the area distributions of samples from different climatic periods and different recrystallization regimes has been established, it would be interesting to determine the three dimensional crystal volume distribution. The determination of the three dimensional structure from a two dimensional measurement is a classic problem in the stereology. A deeper search into the literature of stereology would perhaps give some clues to solve this problem. Another way of approaching the problem would be numerical modeling of the crystal volume, and how different volume shapes would be represented in an intersected area.

A not very comprehensive investigation of the correlation between the individual crystal area method and two of the conventional methods, the linear intercept and the mean area methods was made in this study. This gave an indication of the relation between the new and the conventional methods, but a more comprehensive study is necessary to complement the picture which have been sketched with the first intermistic investigation. Again it is necessary to investigate samples from different depths to cover the wide range of crystal areas and shapes. Although a straight forward result is not likely, I recommend that a study of this is made, to be able to compare old crystal size measurements with results from the new method.

At the North GReenland Ice core Project (NGRIP) ice core drilling in the northern part of central Greenland, an extensive high resolution impurity analysis has been made, on a large part of the 3000 m long core. This impurity record is an excellent opportunity to investigate the role of the different soluble impurities on grain boundary migration. I would therefore recom-

mend a comprehensive study of vertical thin sections from the NGRIP ice core together with the impurity record, which could be very fruitful in determining the importance of the difference impurities influence on the crystal boundary migration.

With the high resolution impurity record it is also possible to investigate the cloudy bands more comprehensive, to determine the origin of the cloudiness. It would also be interesting to investigate the cloudy bands in the deepest part of the core where horizontal shear is believed to be the dominating deformation process. This would perhaps reveal whether the weaker fabric strength is a general characteristic of cloudy bands in the GRIP ice core or if the fabrics in cloudy bands in the horizontal shear is stronger as in the Byrd ice core.

The proposed idea of an increased grain boundary sliding in the cloudy bands could be tested by further deformation tests on ice containing cloudy bands. Here it is inconvenient, that not all cloudy bands contains very small crystals, which seams to give a bias.

A combination of the two methods to measure the texture and the fabric of ice crystals has opened for interesting possibilities for comparison of the parameters. The investigation of one sample in this study revealed no correlation between the size and shape of individual crystals and their orientation. A more extensive study covering samples form different depths and different recrystallization regimes could determine if this is a common feature.

With the possibility of determining both the size and shape and the orientation of the individual crystals comes also the possibility of examining the relationship between adjacent crystals more extensive. One could e.g. investigate how polygonization (indicated by low-angle boundaries) effects the area distribution. In this way it can be tested if the overlying distribution of very small crystals found in my investigation of the area distribution (see section 5.3.3) originates from polygonization.

Finally, there exists a large challenge in incorporating the knowledge about the crystal properties obtained in the studies recommended above into flow laws, e.g. how does the less well confined fabrics in the cloudy bands effect the flow of the ice?

# Appendix A

# Samples and fabric diagrams

In this appendix, thick sections and thin sections are showed together with the fabric diagram where thay have been measured, for two bags, one stadial and one interstadial. The stadial samples are from 2017.40–2017.95 m depth and are shown on page 104. The interstadial samples shown on page 105 are from 2024.00–2024.55 m depth. The samples are shown from top to bottom, with the oldest/deepest ice in the top. Each sample is 8 cm long, except for the lowermost in figure (the youngest) which is 7 cm long. In the fabric diagrams, 200 randomly chosen c-axes are shown.
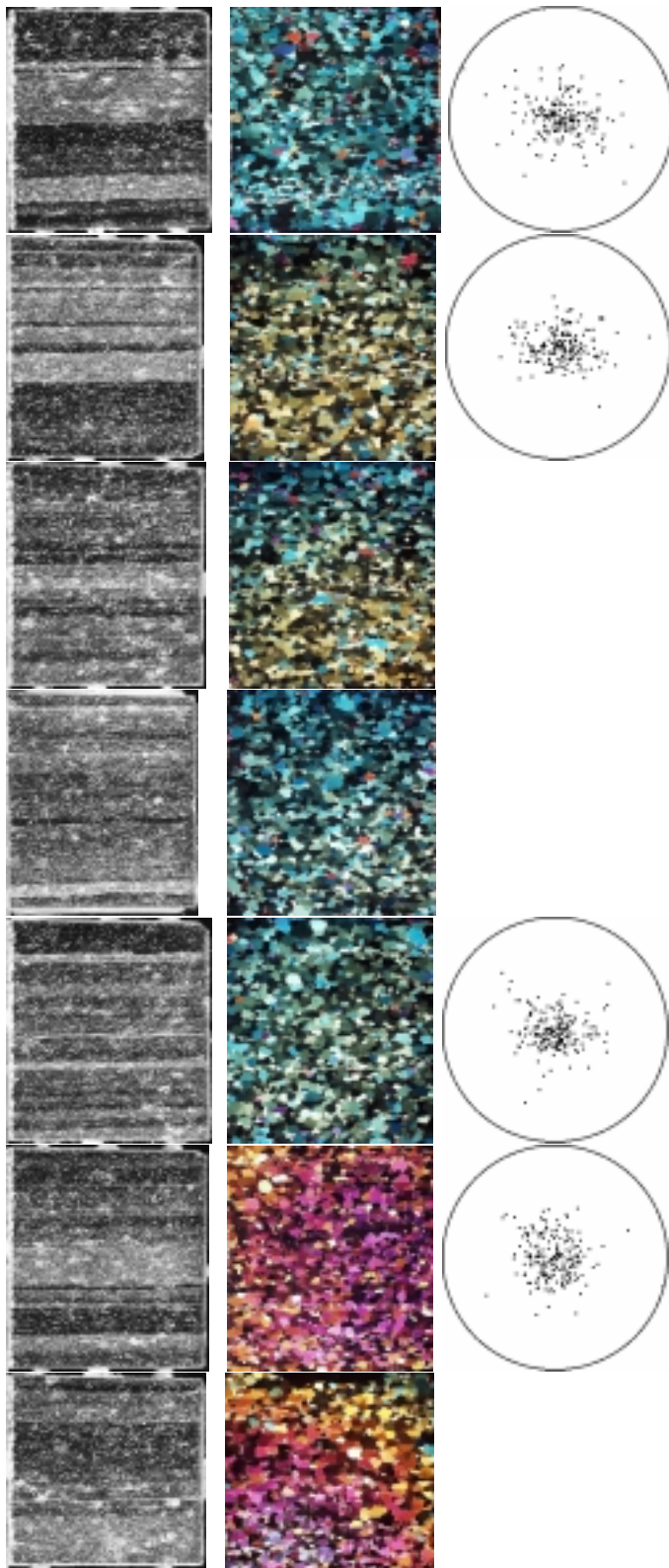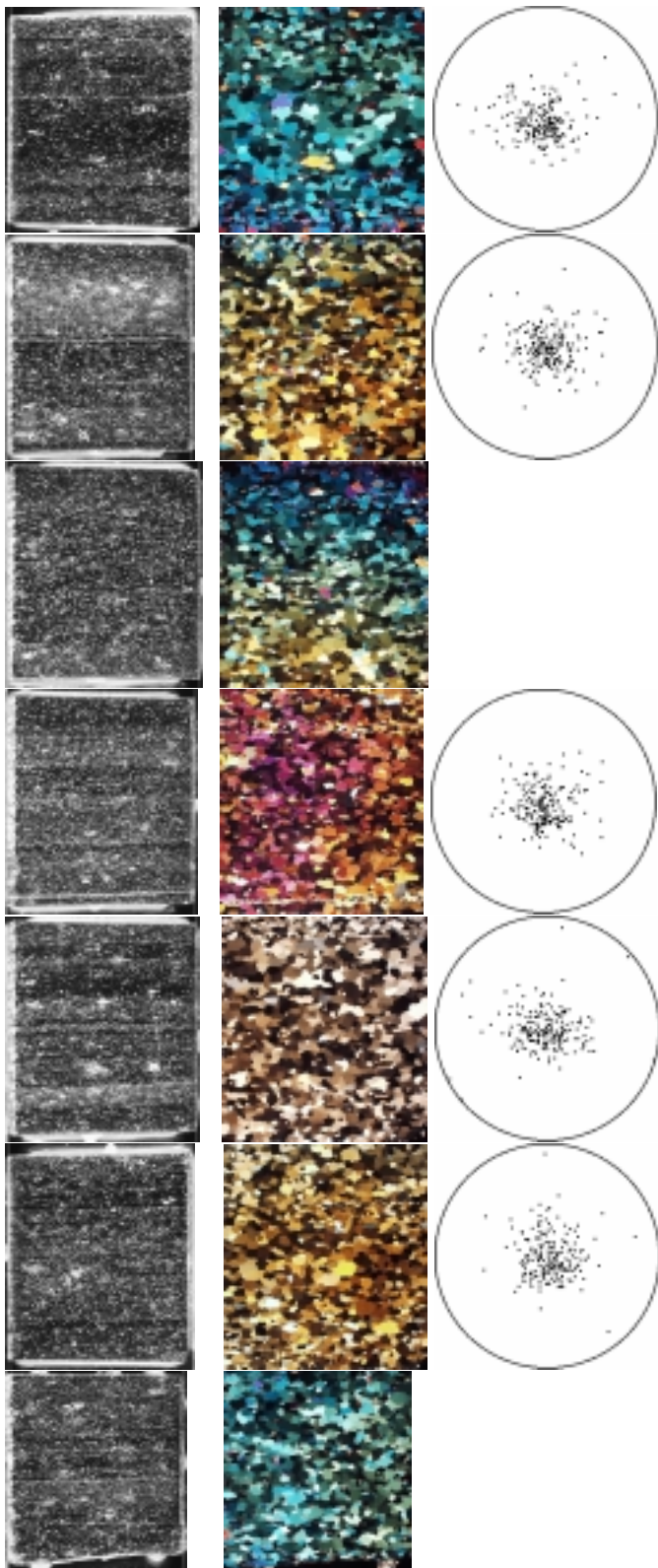
# Appendix B

# Temperature and crystal growth

**The influence of the temperature difference on crystal growth**

The mean crystal size increases with time in the upper part of the ice sheet. This increase depends on the temperature as stated in equations (2.1) and (2.2) on page 13. During glacial interstadial 3, there is a shift in the $\delta^{18}$O parameter from about -41 $^0\!/_{00}$ before the event to about -37 $^0\!/_{00}$ at the peak of the event and back to about -41 $^0\!/_{00}$. The $\delta^{18}$O can be converted to a temperature shift. To find out whether this temperature difference has a significant influence on the mean crystal area found in the thin sections, a simple calculation has been made. This calculation involves an estimation of the temperature difference calculated from the $\delta^{18}$O values and a numerical solution of the equation of heat-flow.

**The temperature difference between interstadial and stadials**

The ice sheet surface temperature is assumed to be related to the $\delta^{18}$O by:

$$T = \alpha + \beta \cdot \delta + \gamma \cdot \delta^2, \tag{B.1}$$

where $\alpha$, $\beta$ and $\gamma$ are constants. The three parameters have been estimated to be $\alpha = -211.4°$C, $\beta = -11.88°$C$/^0\!/_{00}$, and $\gamma = -0.1925°$C$/(^0\!/_{00})^2$ from a comparison of the results of a combined flow/transport model to the measured temperature profile at GRIP [Johnsen et al., 1995]. Substituting these values into equation (B.1) yields a surface temperature of -48°C for the stadial values of $\delta^{18}$O $= -41^0\!/_{00}$, and a temperature of -35°C for the interstadial value of $\delta^{18}$O $= -37^0\!/_{00}$. The shift in $\delta^{18}$O thus corresponds to a temperature change of about 13°C.

**Age of ice**

The normal grain growth regime prevails to a depth of about 700 m in the GRIP ice core [Thorsteinsson et al., 1997]. The cease in growth of the mean crystal size is determined by the increasing stress with depth. Although the ice thickness have changed with time during the Wisconsin [Johnsen et al., 1995], the extension of the normal grain growth regime is assumed constant.

The age of the ice at 700 m depth can be estimated from a Dansgaard-Johnsen flow model, which in the upper part of the ice sheet is given by:

$$t = \frac{(2H - h)}{2\lambda} \ln\left(\frac{(2H - h)}{(2z - h)}\right), \qquad H \geq z \geq h, \qquad (B.2)$$

where $t$ is time, $H$ is the ice thickness, $h$ is the thickness of an intermediate shear layer, $\lambda$ is the accumulation rate and $z$ is height above bedrock [Dansgaard and Johnsen, 1969]. This model has been used to establish a time scale for the GRIP ice core, with the parameters: $H = 3003.8$ m of ice equivalent, and $h = 1200$ m of ice equivalent [Dansgaard et al., 1993]. The accumulation rate, $\lambda$, has been slightly modified from this model calculation by Johnsen et al. (1995) to be:

$$\lambda = 0.23 \exp(-10.9 - 0.653\delta - 0.0104\delta^2) \qquad (B.3)$$

m ice equivalent per year, where 0.23 m ice equivalent per year is the present accumulation rate at GRIP [Johnsen et al., 1995]. $\delta^{18}O$ values for the stadial and interstadial IS3 gives accumulation rates of $\lambda_S = 0.10$, $\lambda_{IS} = 0.17$ m of ice equivalent per year respectively.

If $\lambda$ is taken to be $0.12 \pm 0.02$ as a mean for typical glacial conditions, the age of the ice at 700 m depth, as calculated from equation (B.2), is about $7000 \pm 1400$ year for the period around IS3.

**The heat-flow equation**

The coupled heat- and ice-flow equation is given by:

$$\rho c \frac{\partial T}{\partial t} = \nabla \cdot (K \nabla T) - \rho c \vec{v} \cdot \nabla T + f, \qquad (B.4)$$

where $T$ is temperature, $t$ is time, $\rho$ is density, $c$, $K$ are specific heat capacity and thermal conductivity, $\vec{v}$ is velocity and $f$ is the heat production term. This equation have been used to calculate the temperature history from the measured borehole temperature of the Dye 3 and GRIP ice cores [Dahl-Jensen and Johnsen, 1986, Johnsen et al., 1995, Dahl-Jensen et al., 1998] with great success.

For this purpose a few assumptions are made to simplify the equation. The heat production term arise, e.g. from deformation processes in the ice. Although the deformation changes with depth, the depth interval is so small, that there is almost no differences, and the term can be neglected. The horizontal ice-flow term can be neglected, since there is almost no horizontal flow in the Wisconsin part of the GRIP ice core [Thorsteinsson, 1996]. If the vertical ice-flow term is neglected, the temperature will diffuse more slowly, e.g. because the layer thinning is not taken into account, which would result in an overestimate of the temperature influence. $K$, $\rho$ and $c$ can be assumed independent of $T$ and $z$. This would result in a higher temperature, than if the terms very included [Johnsen, 1977], again resulting in an overestimation of the temperature influence.

With these assumptions, equation (B.4) reduces to the heat-flow equation:

$$\frac{\partial T}{\partial t} = k\frac{\partial^2 T}{\partial z^2}, \tag{B.5}$$

where $k = K/\rho c$ is the thermal diffusivity.

From equation (B.5), a temperature history for the ice containing interstadial 3 can be calculated. This is done numerically, by dividing the ice into depth intervals. As depth intervals, I have chosen the bags (0.55 cm), and from the mean $\delta^{18}$O value of each bag, the temperature of the depth intervals are calculated from equation (B.1). The $\delta^{18}$O values from 2010–2035 m were used for the calculations (45 measurements). This interval was expanded for a further 40 records, by ascribing the value in each end point to 20 more points, an estimate which is very realistic.

The annual layers have thinned to about 20% of their original values at 2000 m depth in the GRIP ice core [?]. Using this, a bag represents about 2.75 m of ice equivalent at the surface, which is used as the size of each depth interval. Note, that each depth interval does not contains an equal amount of yearly layers since the precipitation in the interstadial was higher, and the yearly layers thicker. The temperature in each depth interval is then calculated from:

$$T(t) = T(t - \Delta t) + k\frac{\partial^2 T}{\partial z^2}\Delta t, \tag{B.6}$$

where the second derivative with respect to depth is estimated as:

$$\frac{\partial^2 T}{\partial z^2} \approx \frac{T(z+h) - 2T(z) + T(z-h)}{h^2}, \tag{B.7}$$

where $h$ is the length of the depth intervals ($h = 2.75$ m). For the thermal diffusivity, $k = 1.7 \cdot 10^{-6}$ m$^2$s$^{-1}$ [Paterson, 1994] is used. $\Delta t = 10$ days is used as time step in the numerical model.

**Crystal growth**

The temperature history of the layers is used to calculate the growth of the mean crystal area in each depth interval from equations (2.1) and (2.2) on page 13. The parameters used are: $k_0 = 8.3 \cdot 10^6$ mm/yr [Thorsteinsson et al., 1995], $Q = 42.3$kJ/mol [Paterson, 1994] and $R = 8.314$ J/(K mol). The mean crystal growth is calculated in each depth interval. To find the difference in crystal growth between interstadial and stadials, two depth intervals were chosen, one in the middle of IS3 and one in the stadial before IS3. The mean crystal growth as a function of time in these two depth intervals were subtracted, which is seen in figure B.1. It is seen that the temperature dif-
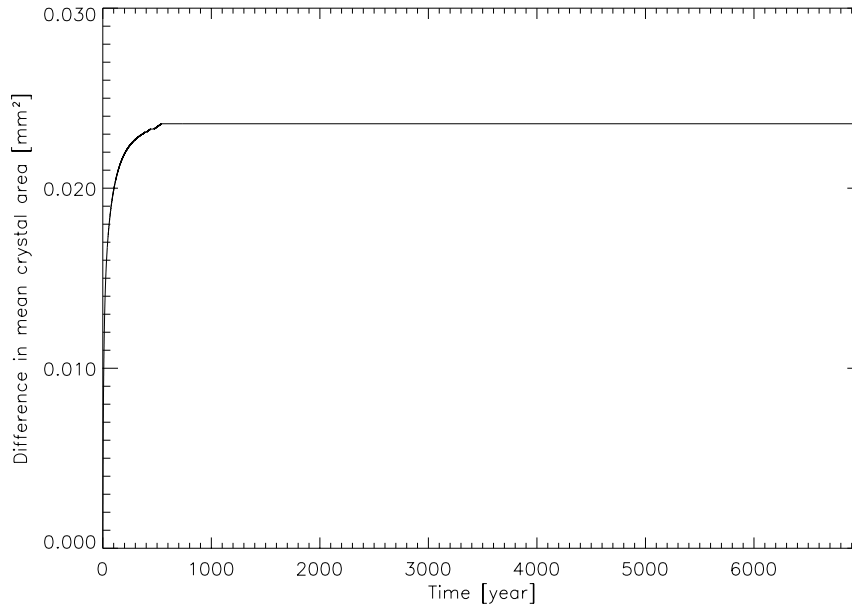


Figure B.1: The difference between the mean crystal area inside and outside the inter-stadial as a function of time in the top 700 m.

ference damps out in about 500 years. During these 500 years, the difference between crystals in the interstadial and in the stadials increases to 0.024 mm$^2$. The result in the simulation is a mean crystal area of about 7 mm$^2$. The difference between crystals in the interstadial and in the stadials is less than 1% of the final mean crystal area, and is thus insignificant. It is also insignificant compared to the measured mean crystal area of about 3 mm$^2$ (see section 5.3.2), which is smaller than the calculated due to the impurity effect.

# Bibliography

[Alley, 1988] Alley, R. B. (1988). Fabrics in polar ice sheets: Development and prediction. *Science*, 240:493–495.

[Alley, 1992] Alley, R. B. (1992). Flow-law hypothesis for ice-sheet modeling. *Journal of Glaciology*, 38(129):245–256.

[Alley and Bentley, 1988] Alley, R. B. and Bentley, C. R. (1988). Ice-core analysis on the siple coast of West Antarctica. *Annals of Glaciology*, 11:1–7.

[Alley et al., 1995a] Alley, R. B., Gow, A. J., Johnsen, S. J., Kipfstuhl, J., Meese, D., and Thorsteinsson, T. (1995a). Comparison of deep ice cores. *Nature*, 373:393–394.

[Alley et al., 1995b] Alley, R. B., Gow, A. J., and Meese, D. (1995b). Mapping c-axis fabrics to study physical processes in ice. *Journel of Glaciology*, 41(137):197–203.

[Alley and Koci, 1988] Alley, R. B. and Koci, B. R. (1988). Ice-core analysis at Site A, Greenland: Preliminary results. *Annals of Glaciology*, 10:1–4.

[Alley et al., 1986a] Alley, R. B., Perepezko, J. H., and Bentley, C. R. (1986a). Grain growth in polar ice: I. Theory. *Journal of Glaciology*, 32(112):415–424.

[Alley et al., 1986b] Alley, R. B., Perepezko, J. H., and Bentley, C. R. (1986b). Grain growth in polar ice: II. Application. *Journal of Glaciology*, 32(112):425–433.

[Alley et al., 1988] Alley, R. B., Perepezko, J. H., and Bentley, C. R. (1988). Long-term climate changes from crystal growth. *Nature*, 332:592–593.

[Alley et al., 1997] Alley, R. B., Shuman, C. A., Meese, D. A., Gow, A. J., Taylor, K. C., Cuffy, K. M., Fitzpatrick, J. J., Grootes, P. M., Zielinski, G. A., Ram, M., Spinelli, G., and Elder, B. C. (1997). Visual-stratigraphic dating of the GISP2 ice core: Basis, reproducibility, and application. *Journal of Geophysical Research*, 102(C12):26367–26381.

[Alley and Woods, 1996] Alley, R. B. and Woods, G. A. (1996). Impurity influence on normal grain growth in the GISP2 ice core, Greenland. *Journal of Glaciology*, 42(141):255–260.

[Anandakrishnan et al., 1994] Anandakrishnan, S., Fitzpatrick, J. J., Alley, R. B., Gow, A. J., and Meese, D. A. (1994). Shear-wave detection of asymetric c-axis fabrics in the GISP2 ice core, Greenland. *Journal of Glaciology*, 40(136).

[Anderson et al., 1989] Anderson, M. P., Grest, G. S., and Srolovitz, D. J. (1989). Computer simulations of normal grain growth in three dimensions. *Philosophical Magazine B*, 59(3):293–329.

[Atkinson, 1988] Atkinson, H. V. (1988). Theories of normal grian growth in pure single phase systems. *Acta Metallurgica*, 36(3):469–491.

[Azuma and Goto-Azuma, 1996] Azuma, N. and Goto-Azuma, K. (1996). An anisotropic flow law for ice-sheet ice and its implications. *Annals of Glaciology*, 23:202–208.

[Azuma et al., 2001] Azuma, N., Goto-Azuma, K., Johnsen, S. J., Fujii, Y., and Watanabe, O. (2001). Factors impeding grain growth of ice in Antarctic ice sheet. In preparation.

[Azuma et al., 1999] Azuma, N., Wang, Y., Mori, K., Narita, H., Hondoh, T., Shoji, H., and Watanabe, O. (1999). Textures and fabrics in the Dome F (Antarctica) ice core. *Annals of Glaciology*, 29:163–168.

[Bentley, 1972] Bentley, C. R. (1972). Seismic-wave velocities in anisotropic ice: A comparison of measured and calculated values in and around the deep drill hole at Byrd station, Antarctica. *Journal of Geophysical Research*, 77(23):4406–4420.

[Bond et al., 1993] Bond, G., Broecker, W., Johnsen, S. J., McManus, J., Labeyrie, L., Jouzel, J., and Bonani, G. (1993). Correlations between climate records from North Atlantic sediments and Greenland ice. *Nature*, 365:143–147.

[Castelnau et al., 1998] Castelnau, O., Shoji, H., Mangeney, A., Milsch, H., Duval, P., Miyamoto, A., Kawada, K., and Watanabe, O. (1998). Anisotropic behaviour of GRIP ices and flow in Central Greenland. *Earth and Planetary Science Letters*, (154):307–322.

[Cuffy et al., 2000] Cuffy, K. M., Thorsteinsson, T., and Waddington, E. D. (2000). A renewed argument for crystal size control of ice sheet strain rates. *Journal of Geophysical Research*, 105(B12):27889–27894.

[Dahl-Jensen and Johnsen, 1986] Dahl-Jensen, D. and Johnsen, S. J. (1986). Palaeotemperatures still exist in the Greenland ice sheet. *Nature*, 320(6059):250–252.

[Dahl-Jensen et al., 1993] Dahl-Jensen, D., Johnsen, S. J., Hammer, C. U., Clausen, H. B., and Jouzel, J. (1993). Past accumulation rates derived from observed annual layers in the GRIP ice core from Summit, Central Greenland. In Peltier, W. R., editor, *Ice in the Climate System*, NATO ASI Series, pages 517–532. Springer-Verlag Berlin Heidelberg.

[Dahl-Jensen et al., 1998] Dahl-Jensen, D., Mosegaard, K., Gundestrup, N., Clow, G. D., Johnsen, S. J., Hansen, A. W., and Balling, N. (1998). Past temperatures directly from the Greenland ice sheet. *Science*, 282.

[Dansgaard and Johnsen, 1969] Dansgaard, W. and Johnsen, S. J. (1969). A flow model and a time scale for the core from Camp Century, Greenland. *Journal of Glaciology*, 8(53).

[Dansgaard et al., 1993] Dansgaard, W., Johnsen, S. J., Clausen, H. B., Dahl-Jensen, D., Gundestrup, N., Hammer, C. U., Hvidberg, C. S., Steffensen, J. P., Sveinbjörnsdóttir, A. E., Jouzel, J., and Bond, G. (1993). Evidence for general instability of past climate from a 250-kyr ice-core record. *Nature*, 364:218–220.

[Dansgaard et al., 1984] Dansgaard, W., Johnsen, S. J., Clausen, H. B., Dahl-Jensen, D., and Oeschger, H. (1984). North Atlantic climate oscillations revealed by deep Greenland ice cores. *AGU Geophys. Mono.*, 33:288–298.

[Dansggard et al., 1971] Dansggard, W., Johnsen, S. J., Clausen, H. B., and Langway, Jr., C. C. (1971). Climatic record revealed by the Camp Century ice core. In Turekian, K. K., editor, *Late Cenocoic glacial ages*, chapter 3, pages 37–56. Yale University Press.

[De Angelis et al., 1997] De Angelis, M., Steffensen, J. P., Legrand, M., Clausen, H. B., and Hammer, C. U. (1997). Primary aerosol (sea salt and soil dust) deposited in Greenland ice during the last climatic cycle: Comparison with east Antarctic records. *Journal of Geophysical Research*, 102(C12):26681–26698.

[Duval et al., 1983] Duval, P., Ashby, M. F., and Anderman, I. (1983). Rate-controlling processes in the creep of polycrystalline ice. *Journal of Physical Chemistry*, 87(21):4066–4074.

[Duval and Castelnau, 1995] Duval, P. and Castelnau, O. (1995). Dynamic re-crystallization of ice in polar ice sheets. *Journal de Physique IV*, (5):197–205.

[Duval and Lorius, 1980] Duval, P. and Lorius, C. (1980). Crystal size and climatic record down to the last ice age from Antarctic ice. *Earth and Planetary Science Letters*, (48):59–64.

[Eicken, 1993] Eicken, H. (1993). Automated image analysis of ice thin sections — instrumentation, methods and extraction of stereological and textural parameters. *Journal of Glaciology*, 39(132).

[Fisher and Koerner, 1986] Fisher, D. A. and Koerner, R. M. (1986). On the spe-
    cial rheological properties of ancient microparticle-laden northern hemisphere
    ice as derived from bore-hole and core measurements. *Journal of Glaciology*,
    32(112):501–510.

[Gay and Weiss, 1999] Gay, M. and Weiss, J. (1999). Automatic reconstruc-
    tion of polycrystalline ice microstructure from image analysis: Application to
    the EPICA ice core at Dome Concordia, Antarctica. *Journal of Glaciology*,
    45(151):547–554.

[Gow, 1969] Gow, A. J. (1969). On the rates of growth of grains and crystals in
    south polar firn. *Journal of Glaciology*, 8(53):241–252.

[Gow, 1994] Gow, A. J. (1994). Post-drilling recrystallization of the Byrd Station
    deep ice core and its relevance to current and future deep-core drilling on polar
    ice sheets. *Annals of Glaciology*, 20:231–236.

[Gow et al., 1997] Gow, A. J., Meese, D. A., Alley, R. B., Fitzpatrick, J. J.,
    Anadakrishnan, S., Woods, G. A., and Elder, B. C. (1997). Physical and struc-
    tural properties of the Greenland Ice Sheet Project 2 ice core: A review. *Journal
    of Geophysical Research*, 102(C12):26559–26575.

[Gow and Williamson, 1976] Gow, A. J. and Williamson, T. (1976). Rheological
    implications of the internal structure and crystal fabrics of the West Antarctic
    ice sheet as revealed by deep core drilling at Byrd Station. *Geol. Soc. Am. Bull.*,
    87:1665–1677.

[GRIP Members, 1993] GRIP Members (1993). Climate instability during the last
    interglacial period recorded in the GRIP ice core. *Nature*, 364:203–207.

[Gundestrup et al., 1993] Gundestrup, N. S., Dahl-Jensen, D., Johnsen, S. J., and
    Rossi, A. (1993). Bore-hole survey at dome GRIP 1991. *Cold Regions Science
    ad Technology*, 21:399–402.

[Hammer, 2001a] Hammer, C. U. (2001a). Personal communication.

[Hammer, 2001b] Hammer, C. U. (2001b). Unpublished data.

[Hansson, 1994] Hansson, M. E. (1994). The Renland ice core. A Northern Hemi-
    sphere record of aerosol composition over 120,000 years. *Tellus*, 46.

[Herron and Langway, Jr., 1982] Herron, S. L. and Langway, Jr., C. C. (1982). A
    comparison of ice fabrics and textures at Camp Century, Greenland and Byrd
    station, Antarctica. *Annals of Glaciology*, 3:118–124.

[Hirth and Lothe, 1982] Hirth, J. P. and Lothe, J. (1982). *Theory of Dislocations*.
    Wiley, second edition.

[Hobbs, 1974] Hobbs, P. V. (1974). *Ice Physics*. Oxford University Press.

[IDL, 1993] IDL (1993). *IDL Reference Guide*. Research Systems, Inc.

[Image-Pro, 1999] Image-Pro (1999). *Image-Pro plus reference guide for Windows*. Media Cybernetics.

[Jacka, 1984] Jacka, T. H. (1984). Laboratory studies on relationships between ice crystal size and flow rate. *Cold Regions Science and Technology*, 10:31–42.

[Johnsen, 1977] Johnsen, S. J. (1977). Stable isotope profiles compared with temperature profiles in firn with historical temperature records. *IAHS Publ. Procedings of the Grenoble Symposium: Isotopes and Impurities in Snow and Ice*, (118):388–392.

[Johnsen et al., 1992a] Johnsen, S. J., Clausen, H. B., Dansgaard, W., Fuhrer, K., Gundestrup, N., Hammer, C. U., Iversen, P., Jouzel, J., Stauffer, B., and Steffensen, J. P. (1992a). Irregular glacial interstadials recorded in a new Greenland ice core. *Nature*, 359:311–313.

[Johnsen et al., 1992b] Johnsen, S. J., Clausen, H. B., Dansgaard, W., Gundestrup, N., Hansson, M., Jonsson, P., Steffensen, J. P., and Sveinbjörnsdóttir, A. E. (1992b). A 'deep' ice core from East Greenland. *Meddelelser om Grønland, Geoscience*, 29:3–22.

[Johnsen et al., 1995] Johnsen, S. J., Dahl-Jensen, D., Dansgaard, W., and Gundestrup, N. (1995). Greenland palaeotemperatures derived from GRIP bore hole temperature and ice core isotope profiles. *Tellus*, 47B:624–629.

[Jun, 1995] Jun, L. (1995). *Interrelation between flow properties and crystal structure of snow and ice*. PhD dissertation, The University of Melbourne, School of Earth Sciences.

[Kamp, 1962] Kamp, B. (1962). Refraction corrections for Universal Stage measurements. I. Uniaxial crystals. *The American Mineralogist*, 47(3):227–245.

[Koerner and Fisher, 1979] Koerner, R. M. and Fisher, D. A. (1979). Discontinuous flow, ice texture, and dirt content in the basal layers of the Devon Island ice cap. *Journal of Glaciology*, 23(89):209–221.

[Kossevitch, 1999] Kossevitch, A. M. (1999). *The crystal lattice: Phonons, Solitons, Dislocations*. Wiley-VCH.

[Lange, 1988] Lange, M. A. (1988). A computer-controled system for ice-fabric analysis on a Rigsby stage. *Annals of Glaciology*, 10:92–94.

[Langway, Jr., 1958] Langway, Jr., C. C. (1958). Ice Fabrics and the Universal Stage. SIPRE Technical Report 62.

[Langway, Jr. et al., 1988] Langway, Jr., C. C., Shoji, H., and Azuma, N. (1988). Crystal size and orientation patterns in the Wisconsin-age ice from Dye 3, Greenland. *Annals of Glaciology*, 10:109–115.

[Madsen, 1997] Madsen, K. N. (1997). Hans Tausen iskernen — studier af krystalstruktur, datering og smeltelagsstratigrafi. Speciale, Niels Bohr Institutet, Københavns Universitet.

[Miyamoto et al., 1999] Miyamoto, A., Narita, H., Hondoh, T., Shoji, H., Kawada, K., Watanabe, O., Dahl-Jensen, D., Gundestrup, N., Clausen, H. B., and Duval, P. (1999). Ice-sheet flow conditions deduced from mechanical tests of ice core. *Annals of Glaciology*, 29:179–183.

[Miyamoto et al., 1997] Miyamoto, A., Shoji, H., Narita, H., Watanabe, O., Clausen, H. B., and Hondoh, T. (1997). An attempt at deformation tests of deep ice core samples containing cloudy bands. *Proc. NIPR Symp. Polar Meteorol. Glaciol.*, 11:87–93.

[Paterson, 1991] Paterson, W. S. B. (1991). Why ice-age is sometimes "soft". *Cold Regions Science and Technology*, 20:75–98.

[Paterson, 1994] Paterson, W. S. B. (1994). *The Physics of Glaciers*. Pergamon, third edition.

[Petit et al., 1987] Petit, J. R., Duval, P., and Lorius, C. (1987). Long-term climatic changes indicated by crystal growth in polar ice. *Nature*, 326:62–64.

[Petrenko and Whitworth, 1999] Petrenko, V. F. and Whitworth, R. W. (1999). *Physics of Ice*. Oxford University Press.

[Poirier, 1985] Poirier, J.-P. (1985). *Creep of crystals*. Cambridge Earth Science Series. Cambridge University Press.

[Rasmussen et al., 1996] Rasmussen, T. L., Thomsen, E., van Weering, T. C. E., and Labeyrie, L. (1996). Rapid changes in surface and deep water conditions at the Faeroe Margin during the last 58,000 years. *Paleoceanography*, 11(6):757–771.

[Steffensen, 2001] Steffensen, J. P. (2001). Unpublished data.

[Taylor et al., 1993] Taylor, K. C., Hammer, C. U., Alley, R. B., Clausen, H. B., Dahl-Jensen, D., Gow, A. J., Gundestrup, N. S., Kipfstuhl, J., Moore, J. C., and Waddington, E. D. (1993). Electrical conductivity measurements from GISP2 and GRIP Greenland ice cores. *Nature*, 366:549–552.

[Thorsteinsson, 1996] Thorsteinsson, T. (1996). Textures and fabrics in the GRIP ice core, in relation to climate history and ice deformation. *Berichte zur Polarforschung*, 205.

[Thorsteinsson et al., 1995] Thorsteinsson, T., Kipfstuhl, J., Eicken, H., Johnsen, S. J., and Fuhrer, K. (1995). Crystal size variations in Eemian-age ice from the GRIP ice core, Central Greenland. *Earth and Planetary Science Letters*, (131):381–394.

[Thorsteinsson et al., 1997] Thorsteinsson, T., Kipfstuhl, J., and Miller, H. (1997). Textures and fabrics in the GRIP ice core. *Journal of Geophysical Research*, 102(C12):26583–26599.

[Underwood, 1970] Underwood, E. E. (1970). *Quantitative Stereology*. Metallurgy and materials. Addison-Wesley Publishing Company.

[Wang and Azuma, 1999] Wang, Y. and Azuma, N. (1999). A new automatic ice-fabric analyzer which uses image-analysis techniques. *Annals of Glaciology*, 29:155–162.

[Zhang et al., 1994] Zhang, Y., Hobbs, B. E., and Jessell, M. W. (1994). The effect of grain-boundary sliding on fabric development in polycrystalline aggregates. *Journal of Structural Geology*, 16(9):1315–1325.